WPI

APRIL 29, 2014

Real-Time Indoor Localization using Visual and Inertial Odometry

A Major Qualifying Project Report

Submitted to the faculty of the

WORCESTER POLYTECHINC INSTITUTE

In partial fulfillment of the requirements for the

Degree of Bachelor of Science in

Electrical & Computer Engineering

By:

Benjamin Anderson

Kai Brevig

Benjamin Collins

Elvis Dapshi

Surabhi Kumar

Advisors:

Dr. R. James Duckworth

Dr. Taskin Padir

Acknowledgements

We would like to acknowledge the

contributions of those who helped make this project a success:

Our project advisors, Professor R. James Duckworth and Professor Taskin Padir for their continuous help and support throughout the course of the project.

Professor David Cyganski for his support and expertise both as an initial advisor, and as a wealth of knowledge with all aspects of odometry.

Graduate student Wisely Benzun, for providing extensive knowledge on visual and inertial odometry, as well as resources for the group to use during the initial stages of the project.

Gradute students Justin Barrett and Elizabeth De Zulueta for providing their insight in the development of the Extended Kalman Filter.

Robert Boisse for his contributions to the hardware assembly for our project.

Abstract

This project encompassed the design and development of a mobile, real-time localization device for use in an indoor environment. The device has potential uses for military and first responders where it is desirable to know the relative location of a moving body, such as a person or robot, within the indoor environment at any given point in time. A system was designed and constructed using visual and inertial odometry methods to meet the project requirements. Stereoscopic image features were detected through a C++ Sobel filter implementation and matched. An inertial measurement unit (IMU) provided raw acceleration and rotation coordinates which were transformed into a global frame of reference. Corresponding global frame coordinates were extracted from the image feature matches and weighed against the inertial coordinates by a non-linear Kalman filter. The Kalman filter produced motion approximations from the input data and transmitted the Kalman position state coordinates via a radio transceiver to a remote base station. This station used a graphical user interface to map the incoming coordinates.

Table of Contents

List of Figures

List of Tables

List of Equations

Executive Summary

Technology for localization and tracking in outdoor environments has improved significantly in recent years, due in great part to the advent of satellite navigation systems such as GPS. Indoor navigation systems on the other hand have been slower to develop due to the lack of a de facto standard method that produces accurate results. Indoor localization has potential uses in various public indoor environments such as shopping malls, hotels, museums, airports, trains, subways, and bus stations. With further advances in technology, indoor positioning may also find use by emergency first responders and military personnel. The technology may also be used in robotics, providing safe navigation for mobile robotic systems.

While satellite navigation is effective for outdoor navigation, the metallic infrastructure of many public buildings attenuates the satellite signal strength enough to mitigate any relevant information it might carry. Other RF based localization technologies, such as WIFI triangulation, suffer from similar signal degradation issues. Compass based systems are ineffective due to the magnetic interference caused by the metallic framework of larger buildings. Various technologies for indoor localization exist, such as inertial measurement, visual odometry, LIDAR, and dead-reckoning. However, these technologies by themselves often prove to be unreliable in effective indoor localization. Visual odometry, or localization by means of camera systems, provides accurate linear movement approximation, but tends to be inaccurate with respect to turns and other rotational movement. Conversely, Inertial odometry, or localization with accelerometers and gyroscopes, provides accurate rotational movement, but fails in long term linear movement approximations due to compounded accelerometer drift associated with gravity.

This project presents a cost effective mobile design which combines both visual and inertial odometry to perform localization within an indoor environment in real-time. The design is intended to be placed on either a human or an otherwise mobile platform which will traverse an indoor environment. A remote user will be able to locate the mobile platform at any given time with respect to its starting position. The device acquires environment and motion data through a stereoscopic camera system and an inertial measurement unit (IMU). This data is stored and manipulated by a central processor running an embedded Linux Operating System, which provides the core functionality to the system. The extracted coordinates are transmitted in real-time via a radio transceiver to a remote user, who can see a plot of the platform's location and trajectory through a custom MATLAB GUI (Graphical User Interface).

Design

A top–level diagram of the intended design is provided below. The crux of the design lies in the fusion of the independent visual and inertial odometry coordinates. This sensor fusion intends to combine the strengths of the two respective odometry systems, while mitigating their weaknesses. Once images are captured, information movement is extracted and transformed to global coordinates. The raw acceleration and rotation data from the inertial measurement unit is transformed to the same frame of reference as the visual odometry data. Once the data is fused, the accurate linear movement from visual odometry can be correlated with accurate rotational movement from the inertial measurement unit so as to more precisely reconstruct the motion of the mobile platform.

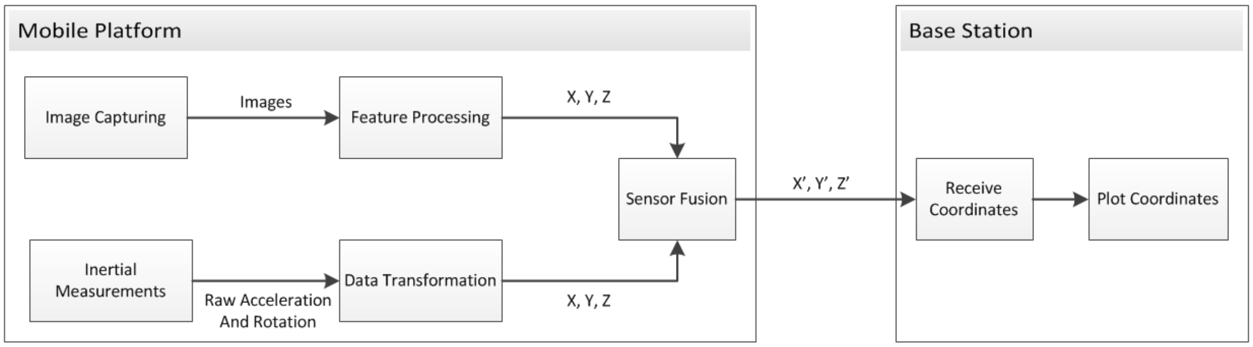

The stereoscopic camera takes a pair of left and right image frames at user-defined frame rate. These images are run through a blob filter in order to find similar sections in the image. A non-maximum suppression algorithm is then used to find areas of interest, or features, in these image sections. The original images are run through a Sobel filter, which is used to create descriptions of each of the detected features. Once features have been detected, they are matched between respective left and right frames, as well as the image frames from the previous time step. Circular matching is performed, in which features from the current time step's left image are matched along a horizontal corridor to the current time step's right frame – and from there to the previous time step's right frame, then to the previous time step's left frame, and finally back to the current time step's left frame. This is done so as to ensure that the same features are being matched across time. Once features have been matched, the platform's motion is reconstructed using RANSAC (RAndom SAmple Consensus). RANSAC takes a small number of randomly selected, successfully matched features, and forms a hypothesis of the system's motion based on these features. This hypothesis is then tested against other successfully matched features, and if enough points fit, it is accepted as the motion of the system. However, if the test fails, a new hypothesis is formed with a different set of points. The accuracy of the motion reconstruction ultimately depends on the number of matched features found.

Simultaneously, the system's acceleration and heading data is measured by the Inertial Measurement Unit (IMU). The gyroscope data from the IMU is converted to the global frame through a rotational matrix describing the orientation of the device relative to its starting orientation, and then integrated to estimate Euler angles. This is combined with the accelerometer data and converted once more to the global frame with another rotational matrix. Finally, this global data is integrated to determine the current position of the system.

These two sets of global coordinates are weighted against each other by an Extended Kalman Filter (EKF). The EKF estimates the current state of the system by forming and validating hypotheses on the system state with each round of new data. The Kalman filter ideally weighs the linear movement data from the camera and the rotational movement from the IMU strongly, while weighing the camera rotation data and the IMU acceleration data weakly. In doing so, the design avoids some of the pitfalls of pure vision or inertial systems, while providing better accuracy at the expense of the complexity of sensor fusion. The Kalman filter output coordinates are continuously transmitted to a base station, which receives the position and heading, and plots it with respect to the initial starting position.

Conclusions

The results from this phase of the project were promising. Successful motion reconstruction from visual odometry was obtained. Similarly, reliable heading estimations were extracted from the inertial odometry implementation. These two sets of data were successfully fused by the Extended Kalman filter to produce a more accurate motion reconstruction.

However, integration challenges were encountered when attempting to combine the two technologies into a real-time, mobile platform. While the visual odometry software performed optimally on x86 processor architectures, a successful ARM port proved to be difficult. This was in large part due to the different set of intrinsic functions between the two architectures, but also due to mishandling of floating point math by the ARM compiler. The intrinsic functions issues were resolved; however the floating point errors were not able to be addressed at this time. It was also noted that the visual odometry algorithms executed more slowly on the ARM processor despite having comparable specifications with the x86 processor; whether this is because of the aforementioned issues or simply due to the inherent architecture differences has yet to be determined. Additionally, documentation and resources for the processor chosen were relatively scarce, in large part due to the processor being new at the time. This further slowed development time when it came to integrating the independent components with the processor.

The gyroscope contained parasitic drifts due to internal changes in temperature, changes in acceleration, as well as inherent bias. Their removal proved to be more challenging than originally anticipated. Regardless, much of the bias on the gyroscope was mitigated, including the drift caused by ambient temperature changes. However, the drifts caused by unpredictable changes in acceleration remain unresolved.

If work is continued on the project, the team recommends investigating a more powerful choice of processor to deal with the intense computational loads required for real-time operation. Additionally, a more robust interface between the camera and the processor would be required. Despite these setbacks, the overall design of the system is still viable. The visual and inertial odometry implementations were successful, as was their fusion with the EKF.

Chapter I. Introduction

Technology for localization and tracking in outdoor environments has improved significantly in recent years, due in great part to the advent of satellite navigation systems such as the Global Positioning System (GPS). GPS has become the de facto technology for outdoor navigation systems, finding uses not only in military environments, but in civil and commercial applications as well. Indoor navigation systems on the other hand have been slower to develop due to no tangible standard method that produces optimal results.

While satellite navigation is effective for outdoor navigation, the metallic infrastructure of many public buildings attenuates the satellite signal strength enough to mitigate any relevant information it might carry. Additionally, the error range of GPS based systems is too large for the resolution at which an indoor positioning system needs to perform. Other RF based technologies, such as WIFI, suffer from the same issues. Compass based systems are ineffective due to the magnetic interference caused by the metallic framework of larger buildings. Various technologies for indoor localization exist, such as inertial measurement, visual odometry, LIDAR, and dead-reckoning. However, these technologies by themselves often prove to be unreliable in effective indoor localization.

Indoor navigation has potential uses in military, civil and commercial applications. Similarly to how GPS is used to provide location directions and current position for users seeking to traverse through an unknown outdoor environment, indoor navigation can provide corresponding results in an enclosed environment. These include large manmade infrastructures such as shopping malls, stadiums, and enclosed plazas, and may be even further extrapolated to define caves and similar settings where satellite navigation would fail. With further development, indoor navigation may be used to reliably track first responders, such as firefighters, during high-risk missions within enclosed environments. By keeping track of first responders' locations at any point in time, as well as any potential victims, numerous tragedies caused by logistics can be avoided. Indoor navigation technology can likewise be beneficial for military personnel when conducting missions in enclosed spaces.

This project explores the design and functionality of an affordable visual odometry system for indoor use. This system will be mounted onto a moving body—such as a robot, vehicle, or person—and will be capable of calculating in real-time the position and orientation of said body with respect to its starting position. The design integrates several techniques so as to create a working visual odometry system. These techniques include feature detection and matching, RANSAC, Inertial Odometry, and an Extended Kalman Filter. This will require accurate sensors and significant processing power in order to be implemented in real-time with little error. In order to achieve this with an affordable system, cost-effective hardware and more efficient algorithms were researched.

Visual odometry, or localization by means of camera systems, provides accurate linear movement approximation, but tends to be inaccurate with respect to turns and other rotational movement. Conversely, inertial odometry, or localization with accelerometers and gyroscopes, provides accurate rotational movement, but fails in long term linear movement approximations due to compounded accelerometer error. Optimal movement approximations canthus be obtained by combining the respective strength of the two technologies, while mitigating their weaknesses.

Visual odometry is performed through feature detection, feature matching, and motion reconstruction. Features are detected by performing non-maximum suppression on blob filtered images. Feature descriptors are extracted from Sobel filtered images. These descriptors are circularly matched between current and past frames in order to efficiently determine camera motion. RANSAC is then performed on the successfully matched feature in order to reconstruct the motion of the system. Inertial odometry is performed by integrating acceleration and rotation data so as to obtain position and heading coordinates. These coordinates, along with those obtained from visual odometry are combined with an Extended Kalman filter which then produces a more reasonable approximation of system motion by fusing the two data sets.

This paper outlines the research, design, and implementation of the system in question. Initially, background information is provided on inertial and visual odometry methodology. Afterwards, the intended system design is discussed in detail. The chosen hardware implementation and the resulting challenges encountered are then explored. The overall results of the independent components of the system, as well as the mobile platform as a whole are provided. The conclusion discusses the overall performance of the system, and provides suggestions for further improvements.

Chapter II. Background

This chapter provides the research performed prior to the implementation of the project. An overview of the fundamental concepts governing the intended design will be provided. Additionally the mathematical properties of feature detection, RANSAC, and Kalman filter approximation will be discussed.

II.I Odometry

Odometry is the estimation of the change in location over time through the utilization of electromechanical sensors or environment tracking. [1] Odometry systems can vary significantly in complexity based upon the desired functionality. An example of a simple system is a typical car odometer that measures the distance travelled by counting the number of wheel rotations and multiplying the result by the tire circumference. The product is the distance traveled in either imperial (miles) or metric (kilometers) units. More advanced odometry systems can provide information including the orientation of a system with respect to an initial position, the trajectory traveled from a starting location, and the current location of a system in relation to its initial position. Advanced odometry systems may be implemented through a variety of methods. One such way of tracking the orientation and movement of a system consists of measuring the forces along the three axes as well as the angular rotation about these axes with a method known as inertial odometry. A second method, known as visual odometry, relies instead on the change in location of a platform with respect to static objects in the surrounding environment. The design proposed in this paper makes use of both visual and inertial odometry to track and locate the system.

II.I.I Inertial Based Navigation

Inertial navigation is a self-contained implementation that uses measurements provided by accelerometers and gyroscopes to track the position and orientation of an object. It is used in various applications including aircraft, missiles, spacecraft, and submarines. Inertial systems fall into two categories, stable platform systems, and strap-down systems. [1]

A stable platform system has the inertial system mounted on a platform which is isolated from external rotational motion. This system uses frames which allow the platform freedom of movement in three axes. Figure II.I and Figure II.II depict a stable platform IMU, and a stable platform inertial measurement unit, respectively.

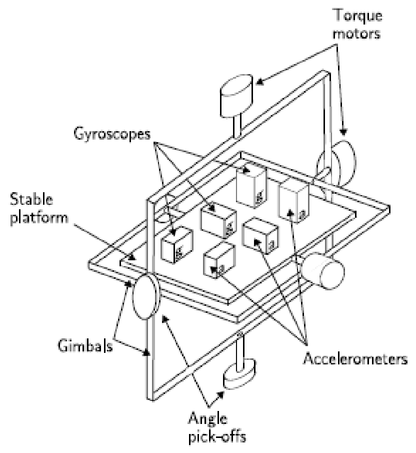

Figure II.I: Stable Platform IMU [1]

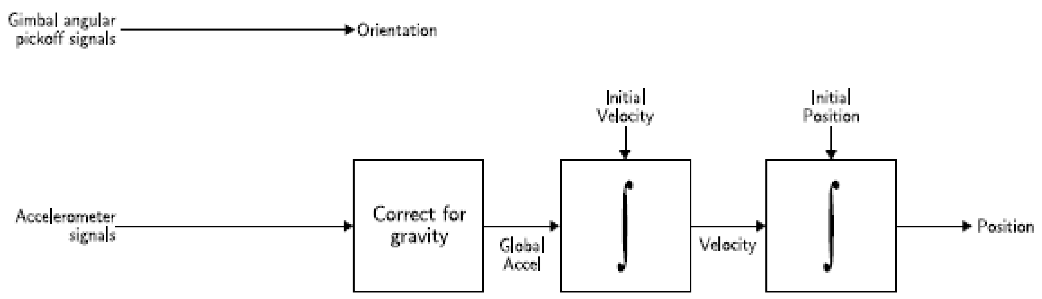

Figure II.II: Stable platform inertial navigation algorithm [1]

A strap-down system is mounted rigidly, directly onto the device, therefore the output quantities are measured in the body frame, rather than the global frame. This requires the gyroscopes to be integrated. [2] Figure II.III depicts a strap-down inertial navigation algorithm.

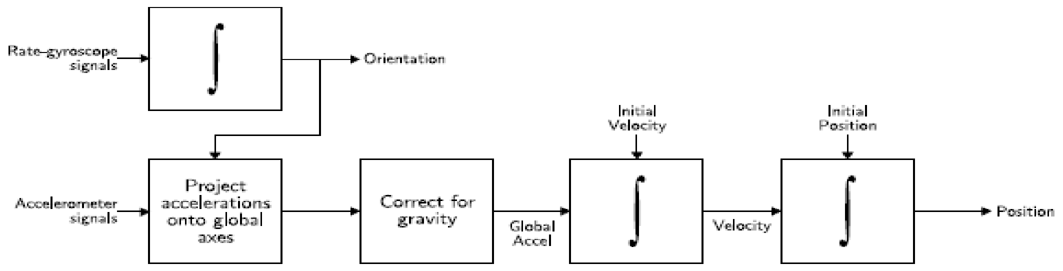

Figure II.III: Strap-down inertial navigation algorithm [1]

II.I.II Accelerometers

An accelerometer is an electromechanical device used to measure acceleration forces. Acceleration can be expressed through Newtonian physics as:

$$a = \frac{F}{m}$$

Equation II.I: Newton's force equation

Accelerometers are generally classified under three categories, Mechanical, Solid State, and MEMS (micro-machined silicon accelerometers). A mechanical accelerometer consists of a mass suspended by springs. The displacement of the mass is measured giving a signal proportional to the force acting on the mass in the input direction. By knowing the mass and the force, the acceleration can be calculated through Newton's equation. [1]

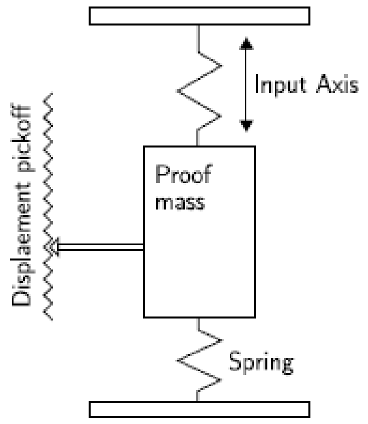

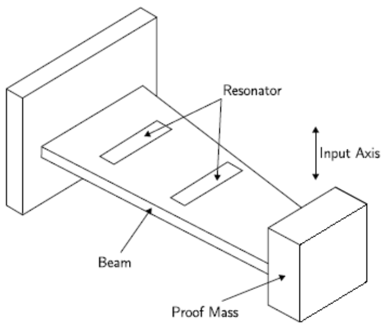

Figure II.IV: a) Mechanical Accelerometer [1] b) SAW accelerometer [1]

A solid-state accelerometer, such as a surface acoustic wave (SAW) accelerometer, consists of a cantilever beam with a mass attached to the end of the beam. The beam is resonated at a particular frequency. When acceleration is applied, the beam bends, which causes the frequency of the acoustic wave to change proportionally. The acceleration can be determined by measuring the change in frequency.

A MEMS (micro-electrical-mechanical system) accelerometer uses the same principles as the other two types, with the key difference being that implemented in a silicon chip, thus being smaller lighter, and less power consuming. On the other hand, MEMS accelerometers tend to be less accurate.

II.I.III Gyroscopes

A gyroscope is a device used for measuring and maintaining orientation using the principles of angular momentum. Gyroscopes can generally be divided into three categories, Mechanical, Optical, and MEMS gyroscopes. [1]

A mechanical gyroscope consists of a spinning wheel mounted upon two gimbals that allows the wheel to rotate in three axes. The wheel will resist changes in orientation due to the conservation of angular momentum. Thus when the gyroscope is subject to rotation, the wheel will remain at a constant orientation whereas the angle between the gimbals will change. The angle between the gimbals can then be read in order to determine the orientation of the device. The main disadvantage of the gyroscopes is that they contain moving parts. Figure II.V depicts a mechanical gyroscope system.

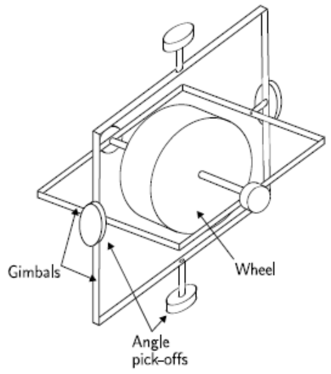

Figure II.V: Mechanical Gyroscope [1]

Optical Gyroscopes used the interference of a light to measure angular velocity. They generally consist of a large coil of an optical fiber. If the sensor is rotating as two light beams are fired on opposite sides, the beam travelling in the direction of rotation will experience a longer path. The angle is then calculated from the phase shift introduced by the Sagnac effect.

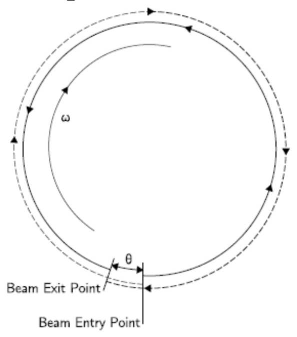

Figure II.VI: Sagnac Effect [1]

As with MEMS accelerometers, MEMS gyroscopes use the same principles as the other two types of gyroscopes, except that MEMS gyroscopes are implemented onto silicon chips. These gyroscopes are more cost efficient and lightweight, but are generally less accurate.

II.I.IV Mono-vision and Stereo-vision Odometry

Visual odometry is the process of using video information from one or more optical cameras to determine the position of the system. This is accomplished by finding points of interest, or features, in each frame or set of frames from the cameras, that are easily distinguishable by the computer and tracking the motion of this information from one frame to the next. Solely using feature location in the frame is not sufficient to track the motion, as this only provides an angular relationship between the camera and the feature. To resolve this problem multiple frames, either from the same camera over time or from two cameras simultaneously, are used to triangulate the position of the feature.

At the highest level, visual odometry can be divided into mono- and stereo-camera odometry. As the name implies, mono-camera systems make use of only a single camera, while stereo-camera systems use two cameras a fixed distance apart.

Mono-vision Odometry

In order to extract depth information from a single camera, two separate frames are used with the assumption that the camera will have moved in the time between the frames. Features that are found in both images are then used as match points, with the camera movement used as the baseline [3] [4].

The benefits of using only a single camera are readily apparent; there is less hardware required reducing system size, cost and hardware complexity. Additionally, there is no need to calibrate several cameras to work together [5] [6].

There are several drawbacks with this type of visual odometry. Camera motion is used as a basis for the distance calculation for features. This motion is not precisely known, as it is the unknown factor in the system.

Stereo-vision Odometry

Stereo camera odometry uses two cameras placed next to each other to determine depth information for each frame by matching features that both cameras can see, and then watching as the points move in space relative to the cameras as the cameras move [7]. The addition of the second camera makes this method superior to mono-camera vision as the depth of each of the points of interest can be found in each frame, as opposed to waiting for the camera to move to provide perspective. Stereo visual odometry can work from just one frame to the next, or a sliding window of frames could be used to potentially improve accuracy [8].

The depths of points can be found by making a ray from each camera at the angle that the point appears to be in and using simple trigonometry to find the perpendicular distance to the point. [9]An example of point patching between two stereo images is shown in Figure II.VII.

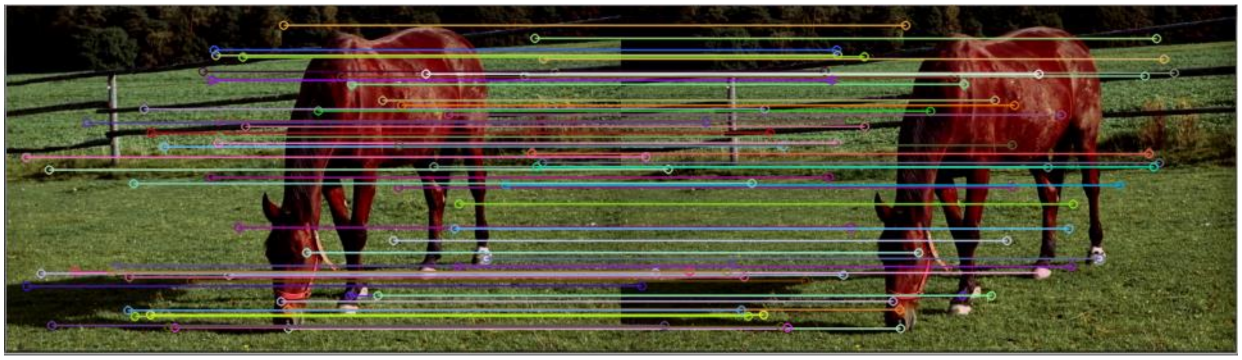

Figure II.VII - Point matching between the images from a stereo camera

Although stereo odometry requires more hardware than monocular visual odometry, it also has increased accuracy and requires less complex computation.

II.II Feature Detection and Matching

Feature matching and detection involves the location, extraction, and matching of unique features between two or more distinct images. Feature Detection is a general term that includes algorithms for detecting a variety of distinct image features. These algorithms can be specialized to detect edges, corner points, blobs, or other unique features. [10]

II.II.I Edge Detection

Edge detection is used to convert a Two-Dimensional image into a set of curves. An edge is a place of rapid change in the image intensity. In order to detect an edge, discrete derivatives of the intensity function need to be derived such that we might get the image gradient. Figure II.VIII depicts an image with respect to its image function. [11]

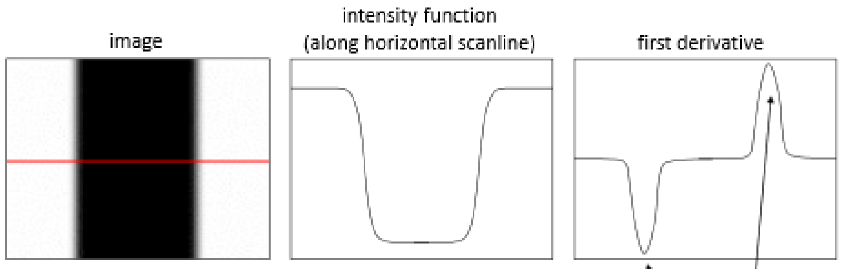

Figure II.VIII: Image edge as function of intensity [11]

Once the discrete derivatives are found, the gradient of the image needs to be calculated. Equation II.II provides the calculation for deriving an image's gradient. In the equation, ∂f is the local change in gradient, whereas x and y are the respective horizontal and vertical pixel changes. Figure II.IX shows an image before and after the gradient has been taken.

$$\nabla f = \left[\frac{\partial f}{\partial x}, \frac{\partial f}{\partial y}\right]$$

Equation II.II: Image gradient from intensity function [11]

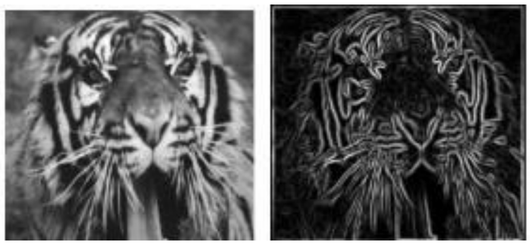
Figure II.IX: Image of Tiger before and after gradient [11]

However, most images will have some noise associated with the edges and must first be smoothed. The general approach to smoothing is a using an image filter such as a Gaussian filter. A Gaussian Filter is applied by taking a small specially crafted matrix or vector, called a kernel, and convolving it with the intensity function of the image. The edges will occur at the peaks of the gradient of the result (if the kernel was a Gaussian function). Figure II.X below provides a graphical of the aforementioned smoothing implementation. [12]

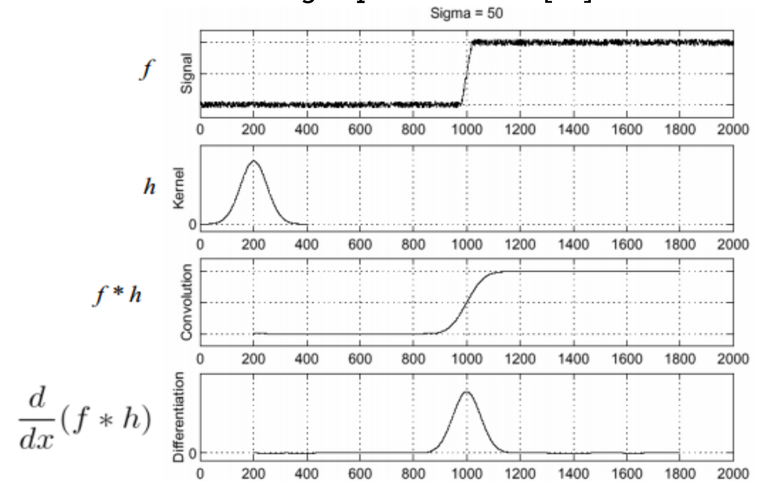

Figure II.X: Smoothing process using Gaussian kernel [12]

It should be noted that due to the associative properties of differentiation. The derivative of the intensity function no longer needs to be calculated if we are smoothing with a Gaussian kernel. The intensity function can simply be multiplied with the intensity of the Gaussian filter.

Some common Edge detection algorithms include the Sobel method, Prewitt method, Roberts method, Laplacian of Gaussian method, zero-cross method, and the Canny method. The Sobel method finds edges using Sobel approximation derivatives. Similarly, the Prewitt and Roberts methods find edges using the Prewitt and Roberts derivatives, respectively. The Laplacian of Gaussians method finds edges by filtering an image with a Laplacian of Gaussian filter, and then looking for the zero crossings. The zero-cross method is similar to the Laplacian of Gaussian method, with the exception that filter on the image can be specified. The Canny method finds edges by looking for local maxima of the gradient of the image. The gradient is calculated using the derivative of a Gaussian filter. [13]

II.II.II Corner Detection

Corner Detection takes advantage of the minimum and maximum eigenvalues from a matrix approximation of a summed up squared differences (SSD) error to find local corners in an image. Three common corner detection algorithms include Harris Corner Detection, Minimum Eigenvalue Corner Detection, and the FAST (Features from Accelerated Test) method. An overview of Minimum Eigenvalue and Harris Corner Detection will be provided below. [13]

Initially, we start with a "window" (a set of pixels) W, in a known location. The window is then shifted by an amount *(u,v)*. Now each pixel (y, x) before and after the change is compared to determine the change.. This can be done by summing up the squared differences (SSD) of each pixel. This SSD defines an error, as given by Equation II.III.

$$E(u,v) = \sum_{(x,y)\in W} [I(x+u, y+v) - I(x,y)]^2$$

Equation II.III: SSD error [12]

The function *I(x+u, y+v)* can then be approximated through Taylor Series Expansion. The order of the Taylor Series is proportional to the magnitude of the window's motion. In general, a larger motion requires a higher order Taylor series. A relatively small motion can be reasonably approximated by a first order series. Equation II.IV shows the first order Taylor Series expansion of the SSD function. The variables I_x and I_y are shorthand for *dI/dx* and *dI/dy* respectively.

$$I(x+u, y+v) \cong I(x,y) + \frac{\partial I}{\partial x}u + \frac{\partial I}{\partial y}v \cong I(x,y) + [I_x \quad I_y] \begin{bmatrix} u \\ v \end{bmatrix}$$

Equation II.IV: First Order Taylor Series Expansion of SSD function [12]

The *I* function expression in Equation II.III can now be replaced with the Taylor expansion derived in Equation II.IV. The result of this operation ultimately yields a much simpler equation, as shown by Equation II.V.

$$E(u,v) = \sum_{(x,y)\in W} [I(x+u, y+v) - I(x,y)]^2 \cong \sum_{(x,y)\in W} \left[I_x u + I_y v\right]^2$$

Equation II.V: Result of Taylor Series substitution to SSD error formula [12]

Equation II.V can be further simplified into Equation II.VI, where *A* is the sum of I_x^2, *B* is the sum of the products of I_x and I_y, and *C* is the sum of I_y^2.

$$A = \sum_{(x,y)\in W} {I_x}^2, \qquad B = \sum_{(x,y)\in W} I_x I_y, \qquad C = \sum_{(x,y)\in W} y^2$$

$$E(u,v) \cong \sum_{(x,y)\in W} \left[I_x u + I_y v\right]^2 \cong Au^2 + 2Buv + Cv^2$$

Equation II.VI: Further simplification of SSD error formula [12]

The surface SSD error *E(u,v)* can be locally approximated by a quadratic form (product of matrices), as presented by Equation II.VI

$$E(u,v) \cong [u \quad v] \underbrace{\begin{bmatrix} A & B \\ B & C \end{bmatrix}}_{H} \begin{bmatrix} u \\ v \end{bmatrix}$$

Equation II.VII: SSD error as quadratic form approximation [12]

In the case of horizontal edge detection, the derivative, I_x will be zero. Thus the expressions, *A* and *B*, found in the matrix *H*, will also be zero. This is shown graphically by Figure II.XI.

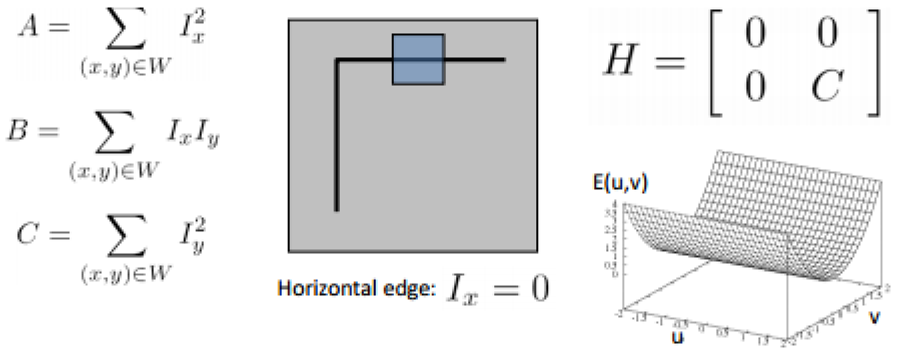
$A = \sum_{(x,y)\in W} I_x^2$
$B = \sum_{(x,y)\in W} I_x I_y$
$C = \sum_{(x,y)\in W} I_y^2$
Horizontal edge: $I_x = 0$
$H = \begin{bmatrix} 0 & 0 \\ 0 & C \end{bmatrix}$
E(u,v)
u
v

Figure II.XI: Result of matrix H in case of Horizontal edge detection [11]

Similarly, in the case of vertical edge detection, the derivative, I_y will be zero, thus making expressions B and C zero. This is shown graphically by Figure II.XII.

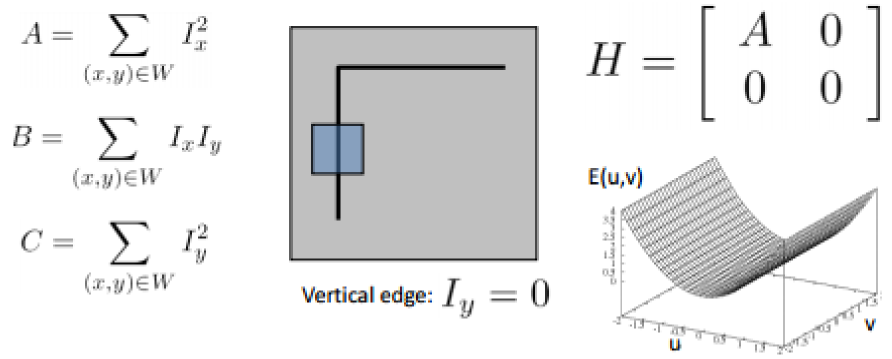
$A = \sum_{(x,y)\in W} I_x^2$
$B = \sum_{(x,y)\in W} I_x I_y$
$C = \sum_{(x,y)\in W} I_y^2$
Vertical edge: $I_y = 0$
$H = \begin{bmatrix} A & 0 \\ 0 & 0 \end{bmatrix}$
E(u,v)
u
v

Figure II.XII: Result of matrix H in case of Vertical edge detection [11]

The matrix H can be visualized as an ellipse with axis lengths defined by the eigenvalues of H, and the ellipse orientation determined by the eigenvectors of H. This can be seen in Figure II.XIII. In general, the shape of H conveys information about the distribution of gradients around the pixel.

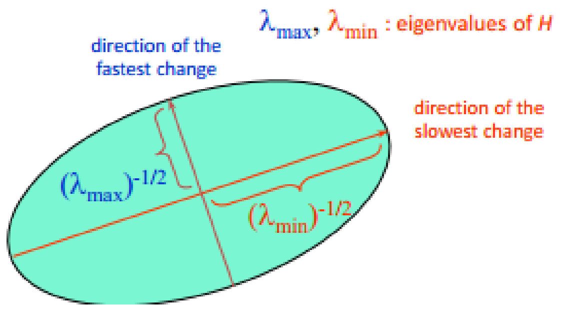
λ_{max}, λ_{min} : eigenvalues of H
direction of the fastest change
direction of the slowest change
$(\lambda_{max})^{-1/2}$
$(\lambda_{min})^{-1/2}$

Figure II.XIII: Elliptical representation of matrix H [11]

Consequently, the maximum and minimum of H needs to be found. For this, the eigenvalues and eigenvectors of *E(u,v)* (the SSD error), need to be calculated. The maximum and minimum ranges of H can be expressed as the product of their respective eigenvectors and eigenvalues Figure II.XIV portrays how the eigenvalues/vectors are used for feature detection. x_{max} is the direction of the largest increase in *E*, x_{min} is the direction of the smallest increase in *E*, λ_{max} is the amount of increase in the x_{max} direction, and λ_{min} is the increase in the x_{min} direction.

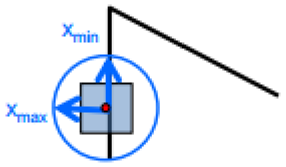

$$Hx_{\max} = \lambda_{\max} x_{\max}$$

$$Hx_{\min} = \lambda_{\min} x_{\min}$$

Figure II.XIV: Using eigenvectors and eigenvalues in corner detection [11]

For corner detection, we want *E(u,v)*to be large for small shifts in all directions. Thus, we want the minimum of the SSD error (λ_{min} of matrix H) to be large. Figure II.XV below shows an image, *I*, with corners, and the images' maximum and minimum eigenvalues after a gradient has been taken.

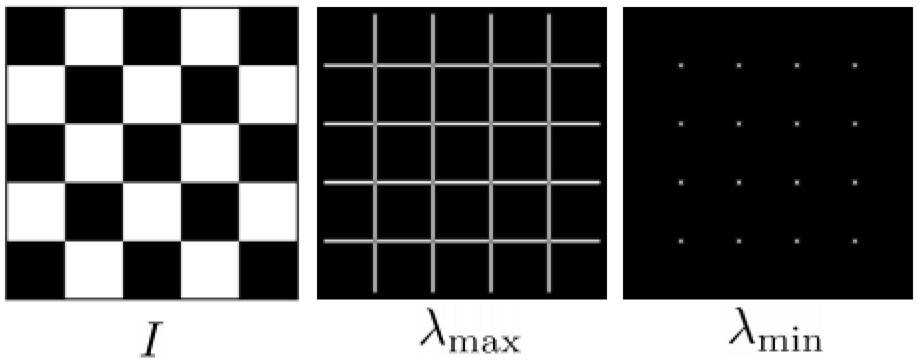

Figure II.XV: An image with its respective maximum and minimum eigenvalues [11]

Figure II.XVI visualizes the interpretation of eigenvalues for our desired functionality. Essentially, when the maximum eigenvalue is much greater than the minimum, or vice-versa, then an edge has been detected. However, when both the maximum and minimum eigenvalues are large and fairly comparable in magnitude, then a corner has been detected. When both the maximum and minimum eigenvalues are small, then a flat region has been detected (e.g. no corner or edge).

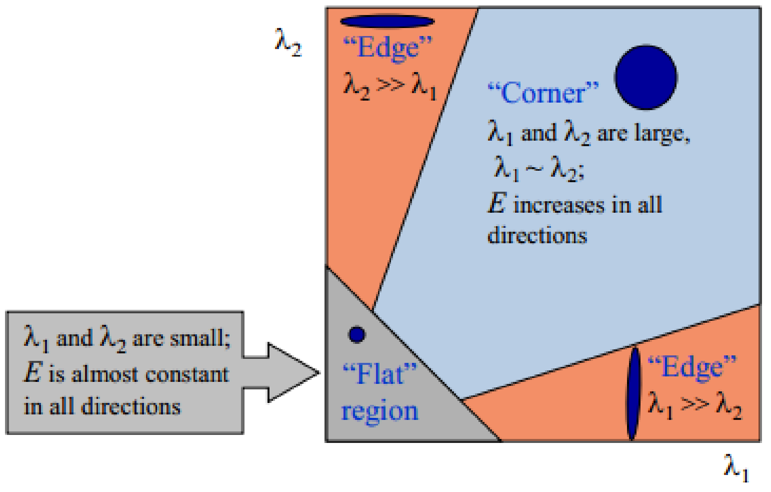

λ_2
"Edge"
$\lambda_2 >> \lambda_1$
"Corner"
λ_1 and λ_2 are large,
$\lambda_1 \sim \lambda_2$;
E increases in all directions
λ_1 and λ_2 are small;
E is almost constant in all directions
"Flat" region
"Edge"
$\lambda_1 >> \lambda_2$
λ_1

Figure II.XVI: Interpreting eigenvalues [11]

In summary, in order to calculate corner detection, we must:

- Compute the gradient at each point in the image
- Create the H matrix from the gradient entries
- Calculate the eigenvalues
- Find the points with large responses
- Choose the point where the minimum eigenvalue is a local maximum as a feature

Figure II.XVII shows a point of the image *I* from Figure II.XV where the minimum eigenvalue is a local maximum.

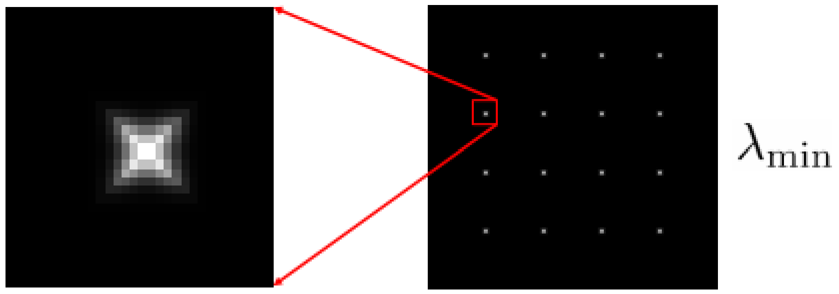

Figure II.XVII: Minimum eigenvalue as a local maximum in image gradient [11]

The minimum eigenvalue, $\lambda_{\min}$, is a variant of the "Harris Operator" used in feature detection. The Harris Operator is given by Equation II.VIII, where the *trace* is the sum of the diagonals. The Harris Corner detector is similar to $\lambda_{\min}$, however, it is less computationally expensive because there is no square root involved.

$$f = \frac{\lambda_1 \lambda_2}{\lambda_1 + \lambda_2} = \frac{determinant(H)}{trace(H)}$$

Equation II.VIII: Harris Corner Detection equation [12]

Figure II.XVIII below shows the results of the Harris operator on the gradient of image *I*. As can be seen, it is comparable to the results of the minimum eigenvalue.

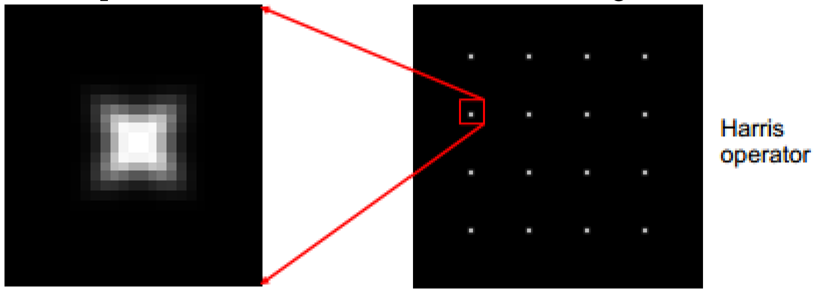

Figure II.XVIII: Harris Operator as local maximum in image gradient [11]

In practice, a small window, *W*, is inefficient and generally does not obtain optimal results. Instead, each derivative value is weighted based on its distance from the center pixel. Equation II.IX provides the matrix H represented by weighted derivatives

$$H = w_{x,y} \begin{bmatrix} I_x^2 & I_x I_y \\ I_x I_y & I_y^2 \end{bmatrix}$$

Equation II.IX: Matrix H represented by weighted derivatives [12]

The Harris method does not require a square root to be taken in the algorithm, and as such is much less computationally expensive. Although the results are not as accurate as with a fully implemented minimum eigenvalue algorithm, they are comparable enough to warrant implementing the Harris method over the minimum eigenvalue method. [12]

II.II.III SURF and SIFT

This section will briefly discuss the Speeded-Up Robust Features (SURF), and the Scale-invariant feature transform (SIFT) algorithms, which are used for detecting, extracting, and matching unique features from images.

SIFT

The Scale-invariant feature transform, or SIFT, is a method for extracting distinctive invariant features from images. These features can be used to perform matching between different views of an object or scene. The advantage of SIFT is that the features are invariant (constant) with respect to the image scale and rotation. SIFT detects key points in the image using a cascade filtering approach that takes advantage of efficient algorithms to identify candidate locations for further examination. The cascade filter approach has four primary steps:

1. **Scale-space extrema detection:** Searches over all scales and image locations. Implemented by using a difference-of-Gaussian function to identify potential interest points.
2. **Keypoint localization:** For each candidate location, a model is fit to determine location and scale. Keypoints are then selected based upon the candidates' measure of stability.
3. **Orientation assignment:** Orientations are assigned to the keypoint locations based on local image gradient directions. Future Operations are performed on the newly transformed image data, thus providing invariance to the transforms.
4. **Keypoint descriptor:** The local image gradients are measured at the selected scale in the region around each keypoint. They are then transformed into a representation which allows for higher levels of shape distortion and illumination modification.

SIFT generates large numbers of features that covers the image over the full range of scales and locations. For example, an image with a size of 500x500 pixels will generate approximately 2000 stable features. For image matching and recognition, Sift features are extracted from a set of reference images stored in a database (in the case of our design, the reference image(s) will be the preceding image pair).The new image is matched by comparing each feature from the new image to that of the preceding image and finding potential matching features based upon the Euclidean distance of their feature vectors. The matching computations can be processed rapidly through nearest-neighbor algorithms. [14]

SURF

The Speeded-Up Robust Features, or SURF, algorithm is a novel scale and rotation invariant feature detector and descriptor. SURF claims to approximate, and at times outperform previously proposed schemes (such as SIFT), while at the same time being able to be computed faster. The speed and robustness of SURF is achieved by taking advantage of integral images for image convolutions. SURF uses a Hessian matrix-based measure for detection, and a distribution based algorithm for description. [15]

SURF initiates by selecting interest points from distinctive locations in an image, such as corners, blobs, and T-junctions. Interest points are detected by using a basic Hessian-matrix approximation upon an integral image. An integral image represents the sum of all pixels bits in the input image within a rectangular region formed by the origin point and x position. Equation II.X shows the general form of an integral image.

$$I_{\Sigma}(x) = \sum_{i=0}^{i \leq x} \sum_{j=0}^{i \leq x} I(i,j)$$

Equation II.X: General form of integral image function [15]

In the next step, SURF represents the neighborhood of every interest points through feature vectors. The descriptor describes the distribution of intensities within the interest point neighborhood in a similar process as SIFT, with the exception that SURF builds upon the distribution of first order Haar wavelet responses rather than the gradient. The weighted Haar responses are represented as points in a space, and the dominant orientation is estimated by calculation the sum of the responses. This ultimately yields an orientation vector for the interest point. Figure II.XIX provides a graphic representation of the orientation vector calculation through Haar wavelet responses.

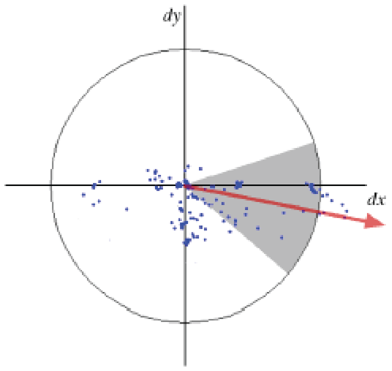

Figure II.XIX: Orientation assignment of interest point via Haar wavelet responses [15]

The descriptor vectors are then matched between different images, based on the distance between vectors. This process is similar to SIFT, with the exception that SURF takes advantage of the sign of the Laplacian generated by the Hessian matrix (the sign of the Laplacian is equivalent to the trace of the Hessian matrix) to exclude points that do not share the same contrast. This results in a faster overall matching speed.

II.II.IV Obtaining World Coordinates from Matched Features

The Feature Detecting algorithms examined find and extract interesting feature points from the stereoscopic images. These feature points can then be matched between the two images preceding them. The algorithms provide local x, and y coordinates from the 2D images, however for this information to actually be relevant, it needs to be interpolated as real world 3-dimensional coordinates. By obtaining the 3-dimensional, or world, coordinates, we can measure the magnitude and direction by which the features changed from the current image to the one preceding it, and consequently determine the change in coordination of the mobile platform. [16]

The first step is to find and extract features using one of the various detection algorithms detailed in the prior sections. The local locations (the location of the feature with respect to the image) are then given in an N-by-2 matrix, corresponding to the local x and y coordinates in the image.

The world coordinates can then be determined through processes of triangulation. If we have a matched feature, *p*¸ that is seen by both cameras, the depth can be determines as shown in Figure II.XX. The difference between x_R, and x_T is equivalent to the disparity of the feature point. The variable, *f*, is the focal length of the cameras in question. [17]

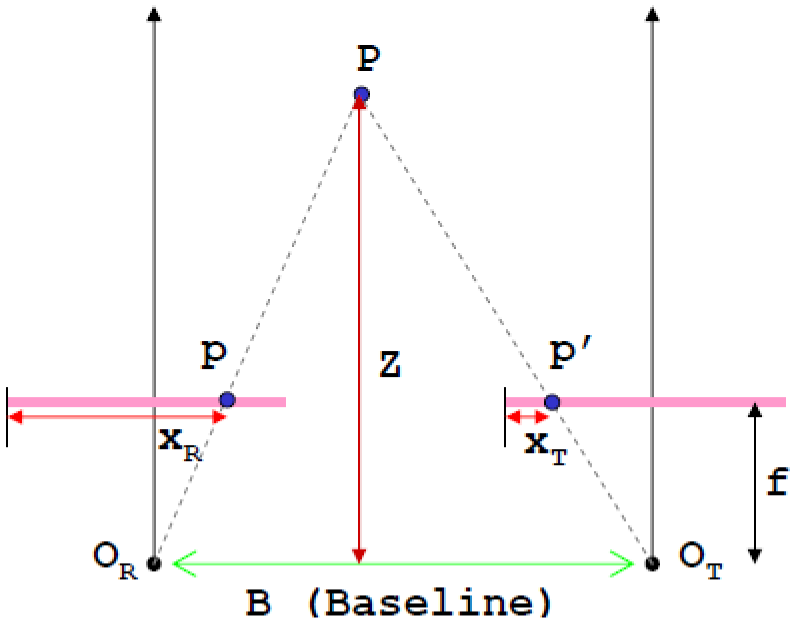

Figure II.XX: Triangulating Feature Point [17]

Thus, the next step would be to find the disparity map between the left and right images. The disparity map will provide the depth of each pixel with respect to the cameras. The world coordinates can then be determined if the baseline and focal length of the camera system is known, along with the calculated disparity map. The respective equations for calculating each world coordinate are given by Equation II.XI, where *d* is the disparity of the image, b is the Vaseline, and x_r, y_r is the local position. Figure II.XXI provides a graphical view of the transformation from local x,y coordinates to world XYZ coordinates by means of a disparity map.

$$Z = \frac{b * f}{d}\,, \qquad X = Z\frac{x_R}{f}, \qquad Y = Z\frac{y_R}{f}$$

Equation II.XI: World coordinates from local coordinates [17]

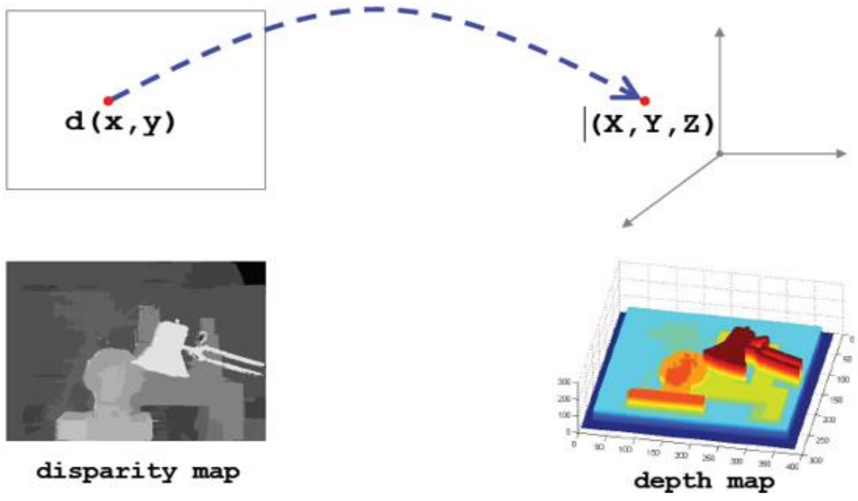

Figure II.XXI: Transformation from local x,y coordinates to world XYZ coordinates [17]

Once world coordinates have been found, they can be sent to the filtering algorithms that will remove any outliers and predict the motion of the subject based upon the coordinates.

II.III RANSAC

Once features have been located in a frame, they must be matched to features in preceding frames in order to find a hypothesis for the motion of the camera. RANSAC (Random Sample Consensus) is an iterative method to estimate parameters of a mathematical model from a set of observed data which contains outliers. It is used in visual odometry to remove false feature matches [4]. Firstly, RANSAC randomly select sample of data points, *s,* from *S* and instantiates the model from this subset [5]. Secondly, it finds set of data points S_i which are within a distance threshold *t* of model. S_i is inlier of dataset *S*. Thirdly, if size of S_i is greater than threshold *T*, model is re-estimated using all points in S_i. After *N* trails largest consensus set *Si* is selected and model is re-estimated using all points in S_i.

RANSAC computes a fundamental matrix (Equation II.XII) to identify incorrect feature matches in stereo images, where *F* is the fundamental matrix and μ_0^T and μ_0^T are image coordinates in pair of stereo images. [5].

$$\boldsymbol{\mu_0^T F \mu_0^T = 0}$$

Equation II.XII: RANSAC fundemental matrix

To determine the number of iterations *N*, the probability of a point being an outlier needs to be known. Equation II.XIII computes number of iterations [5].

$$N = \frac{\log(1-p)}{\log(1-(1-\epsilon)^s)}$$

Equation II.XIII: Number of RANSAC iteration

In the above equation, ∈ is the probability that a point is an outlier, *s* is the number of inliers and *N* is number of trials. Table II.I gives the number of trials for a given sample size and proportion of outliers. The algorithm was tested using the Computer Vision Toolbox in MATLAB and the plots are show in Figure II.XXII, Figure II.XXIII and Figure II.XXIV. The minimum threshold *t* was set to 10^{-2} for first plot and decreased in next two plots. Decreasing *t* increases the proportion of outliers in the data set and gives more accurate point matches.

Table II.I:Number of trails N for a given sample and proportion of outliers

Sample size	Proportion of outliers ∈						
s	5%	10%	20%	25%	30%	40%	50%
2	2	3	5	6	7	11	17
3	3	4	7	9	11	19	35
4	3	5	9	13	17	34	72
5	4	6	12	17	26	57	146
6	4	7	16	24	37	97	293
7	4	8	20	33	54	163	588
8	5	9	26	44	78	272	1177

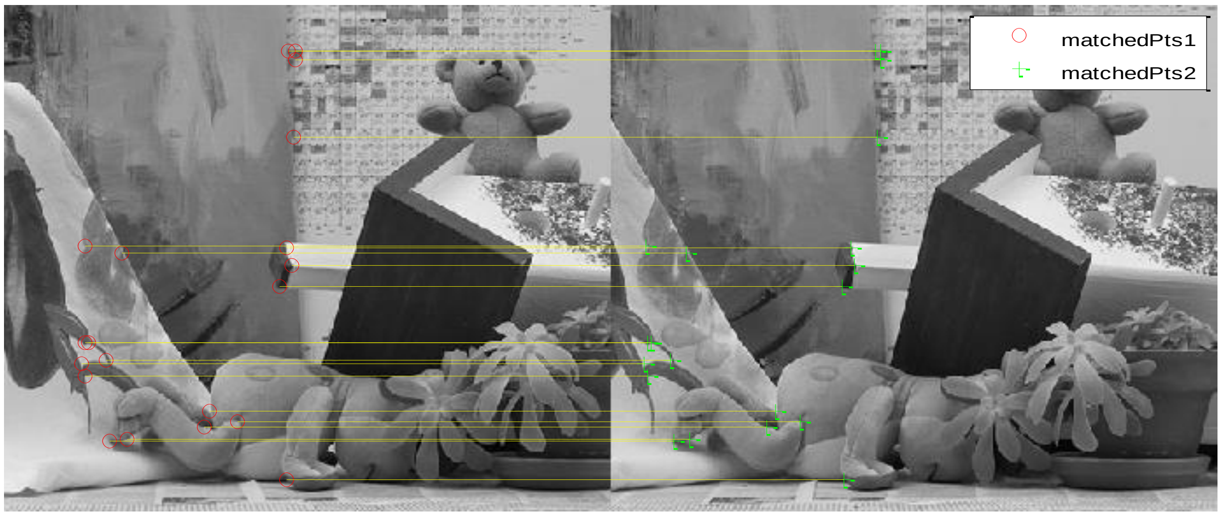

Figure II.XXII: Feature matching

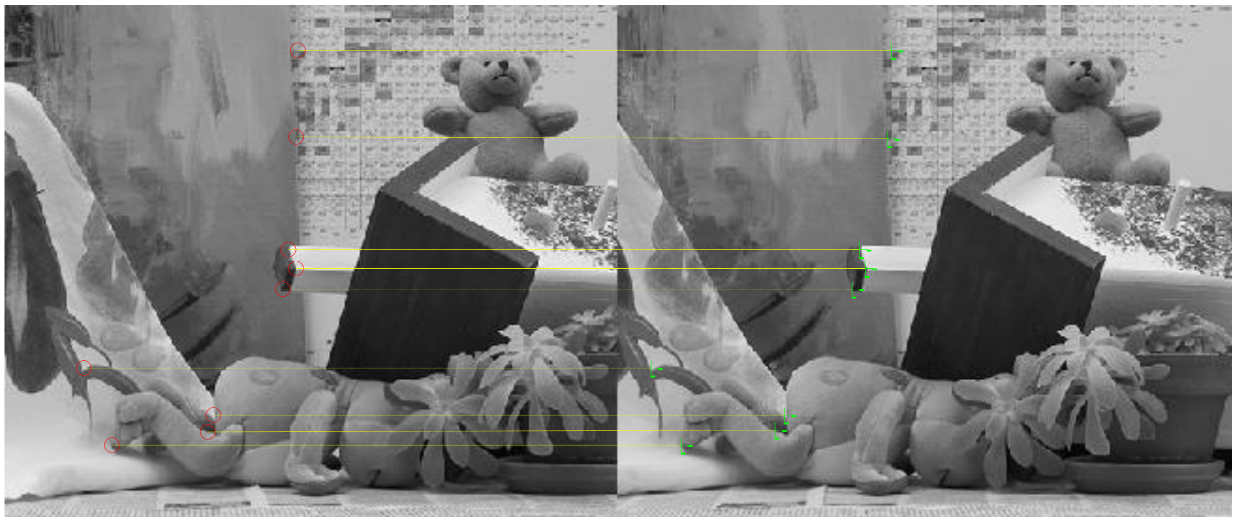

Figure II.XXIII: RANSAC with threshold t=1E-4

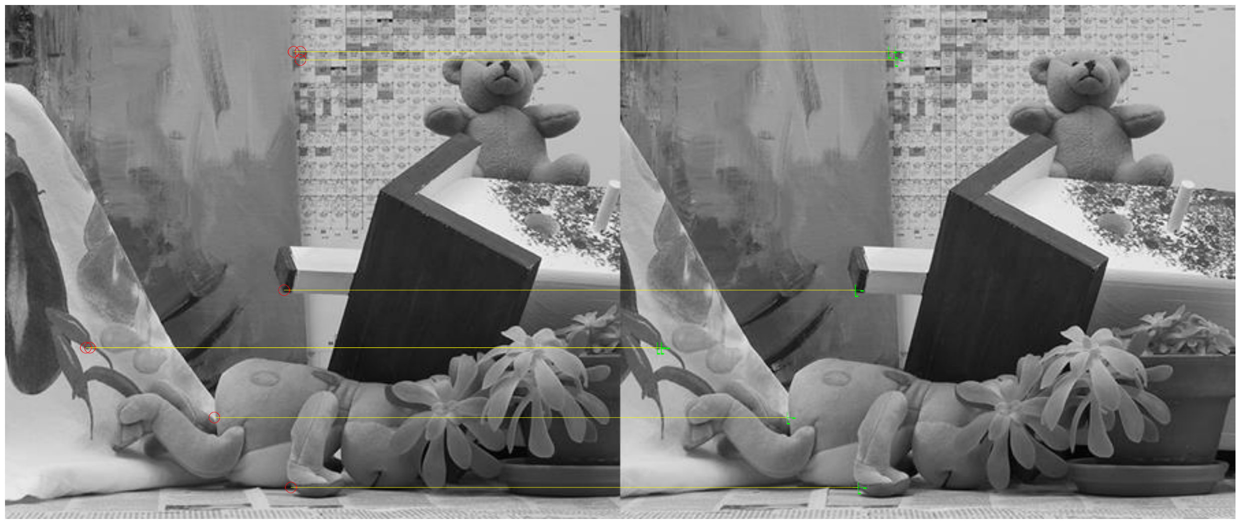

Figure II.XXIV: RANSAC threshold t= 1E-6

II.IV Kalman Filter

The Kalman Filter is a widely used algorithm that uses noisy data and a dynamic model to produce estimations of the unknown variables that describe a system's current state. The Kalman filter is designed to produce a recursive estimation that minimizes the mean of the square error. This becomes very helpful in real time navigation and control of a vehicle given discrete sensor readings. It works by approximating the state of a system in the next time step given the prior state, the observed error, and the estimation covariance. Although the Kalman filter is designed for linear systems, several variants of the Kalman filter have been created to describe nonlinear systems. The linear Kalman filter relies on the dynamic equations to describe the system functionality [18].

II.IV.I Linear Kalman Filter

The linear Kalman filter is reliable due to the fact that it provides estimated state values that have the same average value of the true state in addition to providing the smallest possible error variance. It achieves this by solving for the constants in Equations II.XIV that define the linear system in which A, B, and C are matrices, k is the time index, u is a known input, y is the measured output, x is the state of the system, and w and z are the noise [19].

$$\text{State equation: } x_{k+1} = Ax_k + Bu_k + w_k$$

$$\text{Output Equation } y_k = Cx_k + z_k$$

Equations II.XIV: Linear System Definition [19]

In order to apply the Kalman filter, an assumption must be made that the process noise (w) and the measurement noise (z) must not only be naught, but also have no correlation between each other. This results in Equation II.XV where S_w represents the process noise covariance and S_z represents the measurement noise covariance. In the following equations, a -1 superscript indicates matrix inversion and a T superscript indicates matrix transposition.

$$S_w = E(w_k w_k^T)$$

$$S_z = E(z_k z_k^T)$$

Equation II.XV: Noise Covariance [19]

With this it becomes possible to solve for K, the Kalman gain, $\hat{x}$, the state estimate, and P, the estimation covariance, using Equation II.XVI.

$$K_k = (AP_kC^T + S_z)^{-1}$$

$$\hat{x}_{k+1} = (A\hat{x}_k + Bu_k) + K_k(y_{k+1} - C\hat{x}_k)$$

$$P_{k+1} = AP_kA^T + S_w - AP_kC^TS_z^{-1}CP_kA^T$$

Equation II.XVI: Kalman Filter [19]

II.IV.II Nonlinear Kalman Filter

Nonlinear systems are systems that cannot be described by linear equations but instead by sets of dynamic equations. Our project requires the application of a nonlinear Kalman filter for estimating the position of the system by analyzing the change in position of matched points from multiple frames of our camera. There are multiple types of nonlinear Kalman Filters that each try to reduce the error of each measurement. One such nonlinear filter is the extended Kalman filter which uses a first-order linear approximation of the non-linear system to get an estimation of the state variables [20]. Due to this linear approximation, the Extended Kalman filter often provides error prone results and can even diverge from the true state. The unscented Kalman filter (UKF) is a derivative-free alternative to the Extended Kalman Filter (EKF).

II.V Existing Systems

This section discusses different visual odometry systems currently available or being researched. The first system studied was the Atlas sensor head. Atlas is a bipedal humanoid robot developed by Boston Dynamics with funding and oversight from Defense Advanced Research Projects Agency (DARPA). The robot is 6 feet tall and is designed for a variety of search and rescue tasks. Atlas includes a sensory 'head' built by Carnegie Robotics which features a sophisticated range of sensors, including a pair of stereo cameras, to give robot the 3D awareness of its surroundings. The sensor head has an on-board processor that implements stereo algorithms that transforms left and right images into 3D depth maps at 15 FPS. Figure II.XXV shows depth maps generated by the sensor head. The stereovision system has a depth resolution of ±0.31 mm at 1 m and ±30 mm at 10 meters [21].

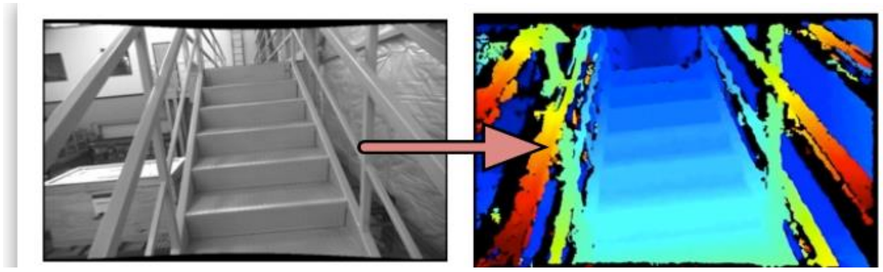

Figure II.XXV: 3D depth maps generated by Atlas sensor head[23]

Other than Atlas sensor head, the group looked into visual odometry papers presented at IEEE conferences and proceedings of the IXth Robotic Science and Systems. Visual odometry has widespread applications in different areas of engineering including tracking first respondents, autonomous quadcopters and autonomous underwater vehicles. Odometry has complex problems such as human bounce, low baseline to depth ratios and noisy data. A research group from Sarnoff Corp. Princeton, New Jersey has developed a human wearable system with two pairs of forward and backward looking stereo cameras together with an IMU [2]. The group has developed an algorithm that can run in real time with 15 Hz update rate on a dual core 2 GHz laptop PC and accurately estimate local pose and act as a front end input to the SLAM algorithm. Data from SLAM and the IMU are integrated using an Extended Kalman filter to predict the most accurate location coordinates. Figure II.XXVI shows block diagram of the odometry system. This method provides more accurate results in situations when cameras fail to provide sufficient features because of poor illumination or non-textured scenes. Figure II.XXVII shows angular velocity results from Visual odometry (red), an IMU (blue) and a Kalman filter(green). As seen in the figure, Kalman filter follows visual odometry measurements for all frames except for frame 2100 when the stereo odometry result is inaccurate. Similar to the visual odometry system developed at Princeton, a research group from the Electrical Engineering department at the University of Texas, Dallas, created an odometry system that fuses data from an IMU, wheel encoders and stereo vision system to improve accuracy of location coordinates [4]. Figure II.XXVIII shows translation and rotational motion of camera frame. In the figure, Fb is the moving frame of reference, Fb* is the static frame of reference i.e. pose at time t=0, T is the translational motion vector, R is the rotational motion vector, m1 is the coordinates of the feature point in the moving frame of reference and m1* is the coordinates of the feature point in the static frame of reference. Discrete and continuous

Homography Matrices are used to recover position, orientation, and velocity from image sequences of tracked feature points. The relationship between image points is given by Equation II.XVII and the Homography matrix is given by Equation II.XVIII.

$$m_j = \left(R + \frac{1}{d^*} T n^{*T}\right) m^*{}_j$$

Equation II.XVII: Relationship between image points

$$H_d = \left(R + \frac{1}{d^*} T n^{*T}\right)$$

Equation II.XVIII: Homography matrix

The Kalman filter fuses measurements from visual odometry and inertial measurement systems. Time varying matrices in the Kalman filter allows each sensor to receive high or low priority depending on which sensor is providing more accurate data at the given time. After studying the above systems it can be concluded that fusing odometry data from multiple sensors using a Kalman filter gives more accurate results.

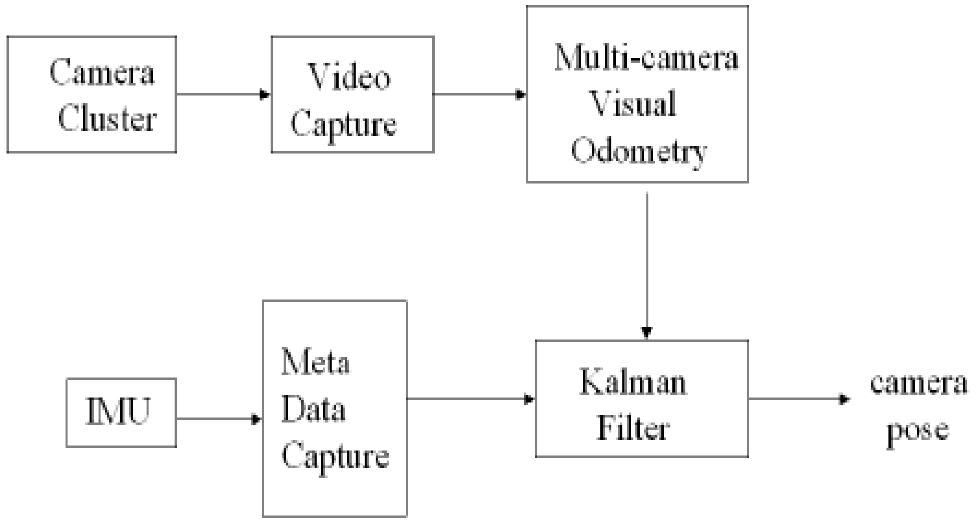

Figure II.XXVI: Flow diagram for multi camera odometry and IMU integration [22]

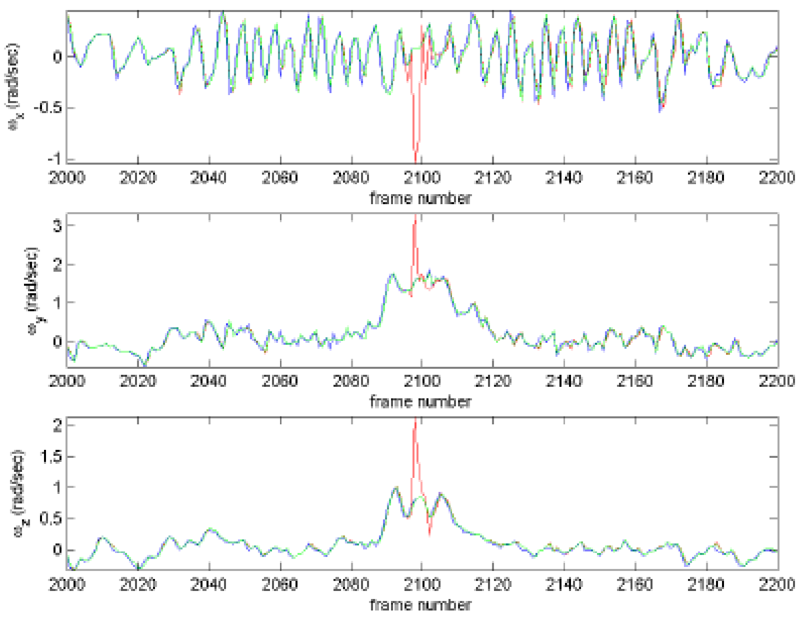

Figure II.XXVII: Results from SLAM, IMU and Kalman filter [22]

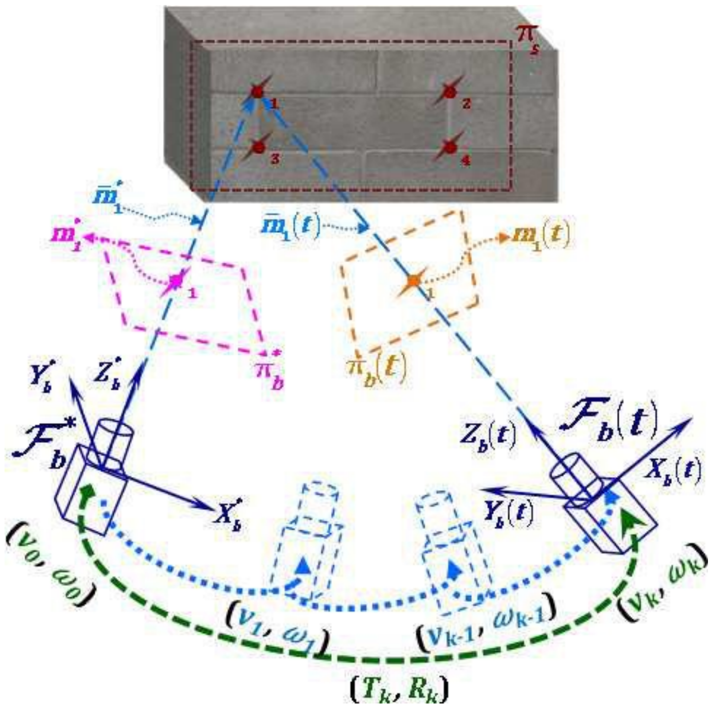

Figure II.XXVIII: Translation and rotational motion of camera frame [23]

Chapter III. System Design

This chapter will discuss the overall design of the mobile system. The design consists of five major parts, Data Acquisition, Feature Detection and Matching, Kalman Filter approximation, Power management and the top level User Interface. Figure III.I provides a top level diagram of the system design.

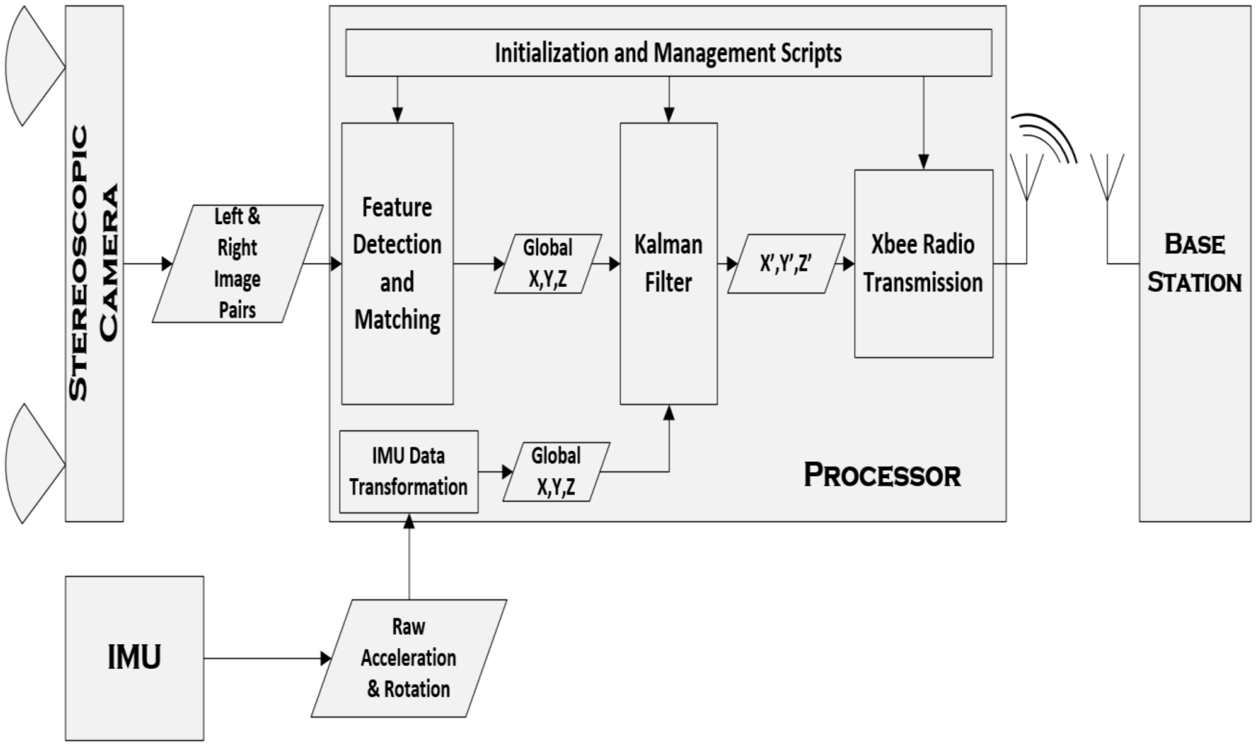

Figure III.I: Top Level System Design

III.I Data Acquisition

The system has two primary means of acquiring data for localization. A stereoscopic camera is used to bring in sets of image frames for feature detection and matching. An IMU is used to support the output of the camera data by providing a different set of acceleration and rotation approximations.

III.I.I Stereo Vision Camera System

A Stereo Vision Camera System consists of two image sensors configured onto a base board in left and right positions. The two image sensors work simultaneously and independently of one another. As such, for each discrete time constant the system produces two images, one from each respective sensor. The images are a rectangular matrix of pixels, with the number of pixels corresponding to the overall resolution of the image. The pixel bits control the color of the specific pixel. For example, a 3 bit pixel will have 8 (2^3) distinct colors available. The number of bits per pixel is dependent on the image sensor. These left and right images will ideally be identical with the exception of a central offset corresponding to the baseline. In other words, the pixels of the left image starting from the left edge and traversing the length of the baseline, as well as the pixels of the right image starting from the right edge and traversing the length of the baseline, will be unique to their corresponding images. The pixels not within the aforementioned range will have equivalent correspondence between the two images. These corresponding pixels will be locally shifted by the length of the baseline. Figure III.III provides a graphical representation of this property.

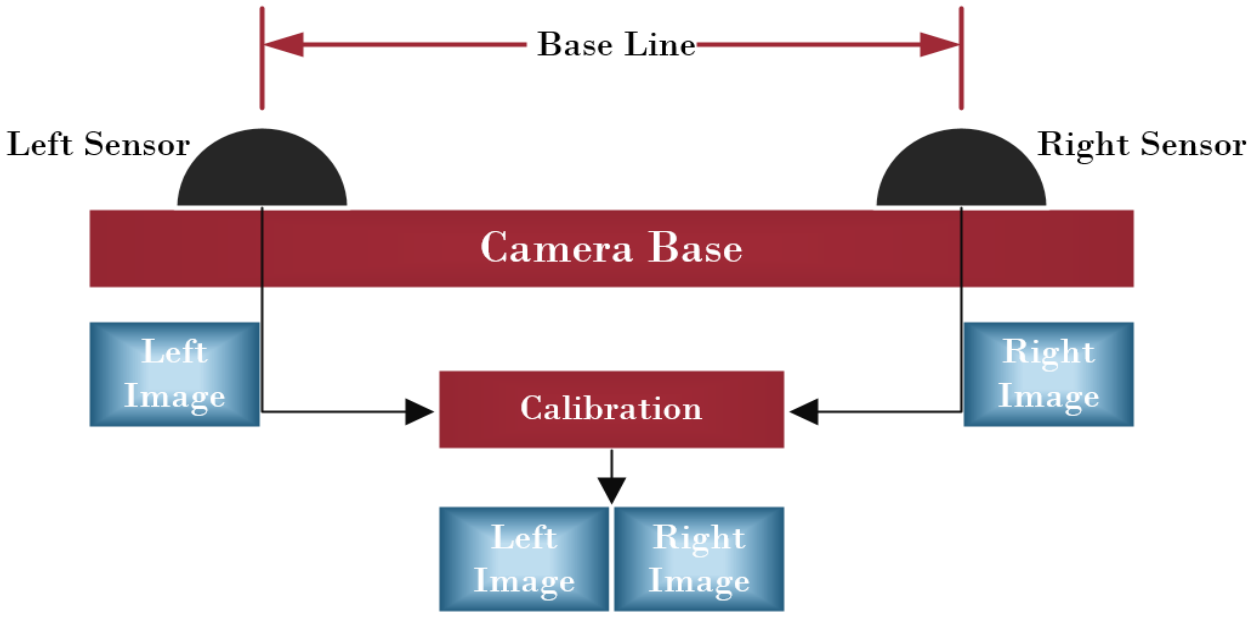

Figure III.II: General Stereoscopic Camera Implementation

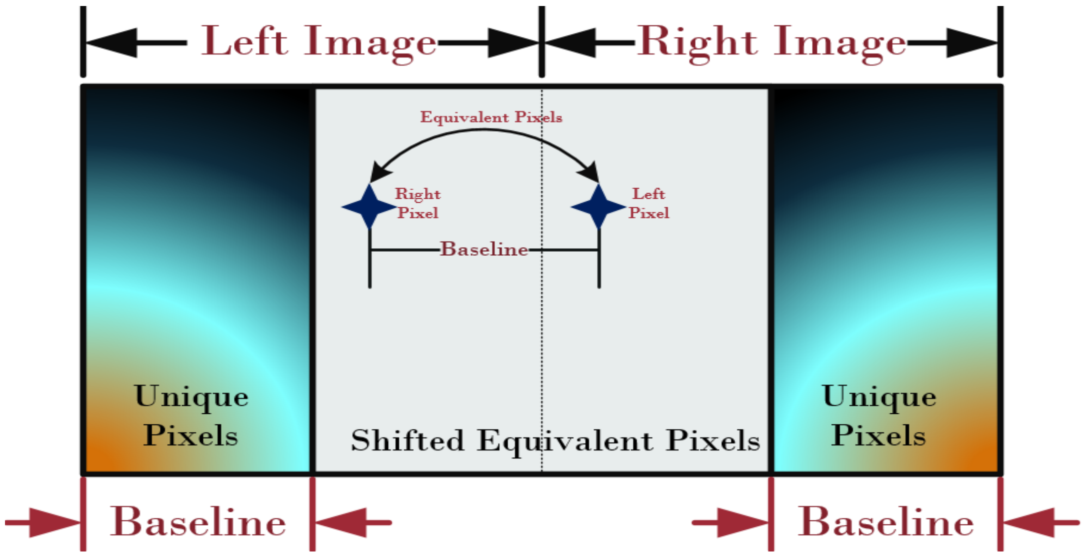

Figure III.III: Correspondence between Left and Right Images

This local shift of equivalent pixels between the left and right image frames is the fundamental property that allows for depth, or Z-vector, calculations to be later produced. By comparing the equivalent pixel movements from the frames of the next discrete time constant, the overall movement of the camera system can be approximated within its local frame. A stereoscopic camera system will usually have to calibrate the two frames before any processing can be done. The calibration aligns the frames such that they fall within the same horizontal axis. The calibration also serves to remove image distortion due to warping, and find the parameters of the camera pairs.

The raw output of the Stereoscopic camera system is then encoded and compressed as either a pair of bitmap (BMP) or JPEG images. The bitmap compression is lossless (the integrity of the data remains the same), but the data set size is much larger. On the other hand, the JPEG compression loses some information, but has a much smaller data set size. In either case, the image pairs can be opened up in software as an array. The pixels can then be processed and manipulated on the bitwise level.

III.I.II Inertial Measurement Unit

The IMU used in the system has two sensors – an accelerometer and a gyroscope to collect acceleration and angular velocity measurements. Accelerometers measure inertial forces, or the forces (and hence acceleration) that is directed in the opposite direction from the acceleration vector. For example, if the accelerometer is sitting idle on the table, with positive Z axis pointing downwards, then Z axis acceleration will be -1g. The accelerometer data consists of x, y, and z measurements that can be used to calculate velocity and position through integration. The gyroscope data consists of the change in roll (φ), pitch (θ), and yaw (ψ) which is the angle of rotation about the X,Y and Z axes respectively as shown in Figure III.IV. The angular velocity, similarly, can be used to track the angular heading of the system. The IMU sensors output an analog voltage proportional to the sensed acceleration and angular velocity that is converted to a digital value using an Analog to Digital Converter. IMU datasheets have conversion factors to convert digital values from the ADC to acceleration values in meters per second squared or degrees per second.

Gyroscopes have static bias which is the signal output from gyro when it is not experiencing any rotation. Gyroscopes also have bias that varies with temperature and time. The variation of bias over time is called bias drift. Gyroscopes provide reasonable estimations of turns over a short period of time. However the position computed using accelerometer data drifts very quickly due the cubing of measurement error. MEMS IMUs have separate registers to store accelerometer and gyroscope data. The processor is used to communicate with the IMU to read in measurements from the registers through digital interfaces like SPI or I2C. This data from the IMU is fused with velocity estimations from the visual odometry subsystem in the Kalman filter. Sensor fusion with IMU data makes the visual odometry results more robust.

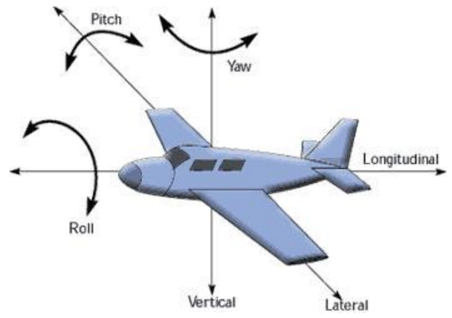

Figure III.IV: Euler angles with respect to the axes of an airplane

III.II Feature Detection and Matching Algorithm

The core of the visual odometry process is the feature detector and matcher. This section of code processes raw images into a set of points of interest that are matched between left and right frame pairs and between subsequent frames. These points, known as features, can then be used to reconstruct the motion of the camera. Figure III.V provides a top level view of the feature detector and matcher.

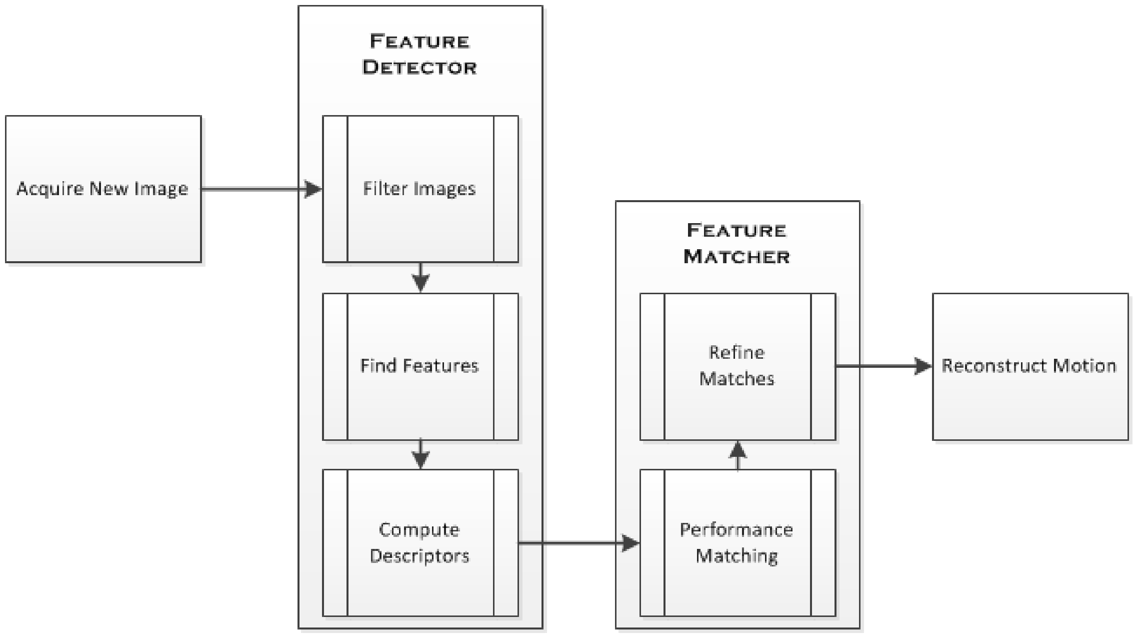

Figure III.V: Top level flow chart of feature detector and matcher

Although the team experimented with writing detector, matcher and motion reconstruction code, it was determined that it would be more efficient to use freely available published code. The library used, Libviso2, was written by Dr. Andreas Geiger from the Max Planck Institute for Intelligent Systems in Germany [10]. This library provided the team with a fully implemented platform for each step of the visual odometry process. The algorithm used had several similarities to what had already been researched by the team, with some differences. The components of the library that are primarily responsible for the core functionality are discussed below.

The library takes many steps to speed up what is a very computationally expensive process. One of these steps is finding features and calculating descriptors at half resolution. This is significantly more efficient, while incurring only a minor accuracy penalty.

III.II.I Sobel Filter

The Sobel filter is an edge finding algorithm that is frequently used in computer vision as it can efficiently find edges in an image. In order to calculate the Sobel filter for a given image, a matrix of constants, called a kernel, is convolved across each row horizontally to create the horizontal gradient, and down each column vertically to get the vertical gradient.

In Libviso2, the Sobel-filtered versions of the image are not used for feature detection, as was done in some of the team's early visual odometry implementations. Instead, it is used solely to construct descriptors for detected features. An example of the actual output of the Sobel filter used in Libviso2 is shown below.

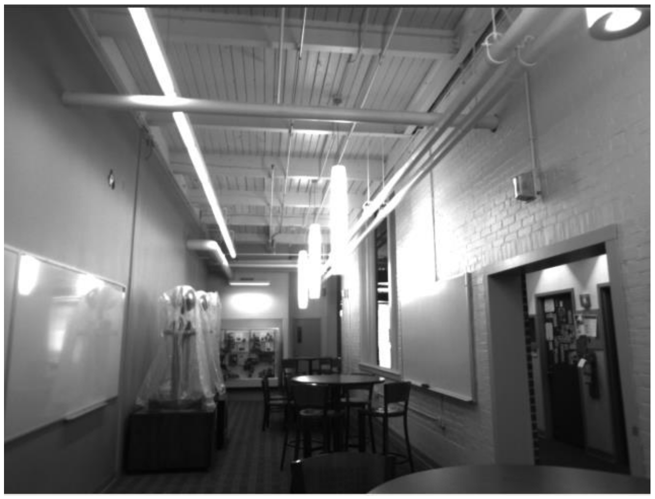
Figure III.VI: Sample image from camera before filtering

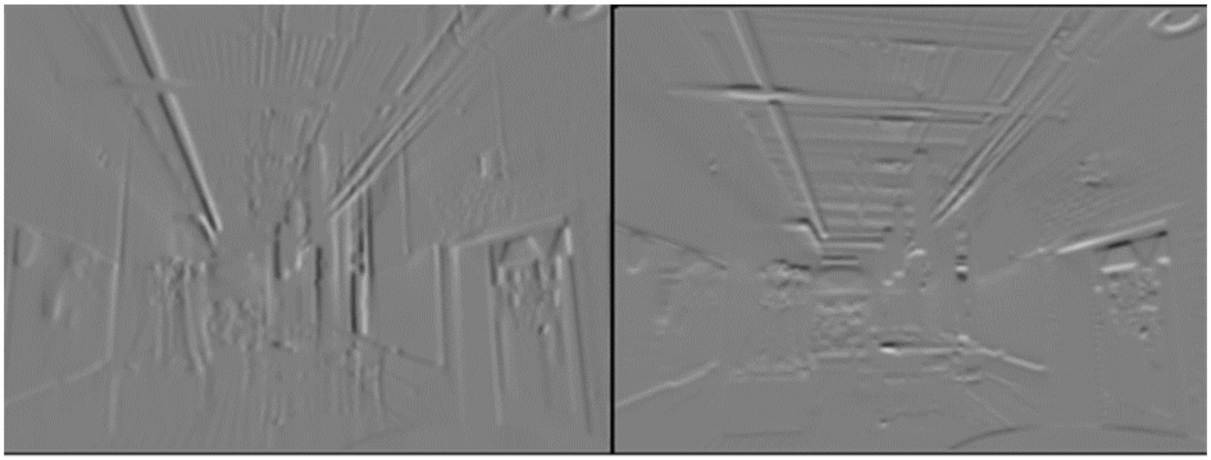
Figure III.VII: The horizontal and vertical results of the Sobel Operator

The output consists of two different images: one representing the horizontal gradient and one representing the vertical gradient. For applications that are intended to be directly used by people, such as edge filters in photo manipulation software, these two images can be combined into one that includes both horizontal and vertical edges. For the creation of descriptors however, the two are kept separate. The descriptors are a representation of the pixels surrounding a feature that are compared to the descriptors of other features determine if the two features are the same object.

III.II.II Feature Detection Using Non-Maximum Suppression

Non-maximum suppression is an algorithm that thins edges in a processed image by setting pixels in a given range to zero if they are not the highest valued pixel. This algorithm was used to find the local maximums, which were then used as features. The images sent to the non-maximum suppression algorithm were first run through a blob filter, which has the effect of forcing similar areas in an image to the same color, creating sharp gradients where different areas touch. The output of the blob filter on the image used above for the Sobel filter is demonstrated below in Figure III.VIII.

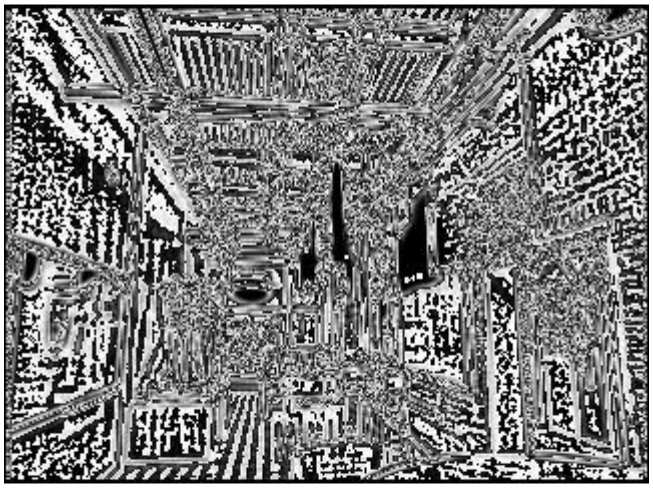

Figure III.VIII: Output from blob filter

This processed image allows non-maximum suppression to easily bring out edges and corners, which are then used as feature points. Descriptors of these features are then created using the Sobel filtered images.

III.II.III Matching

Matching is done by comparing the descriptor of each feature with that of every other feature. Features that are the same will have similar descriptors.

Libviso2 uses circular matching, where instead of matching features between corresponding left and right frames and then matching then to one of the previous frames, each feature from a given frame is tracked across each of the other four frames in a set. This is shown in the diagram below. First, in Step 1, a feature is matched from the previous left frame to the previous right frame. This search can be constrained to a narrow horizontal corridor, as matches between stereo frames on a calibrated camera will be perfectly horizontal to each other. Next, the match is then matched to the current right frame. In order to minimize the time it takes to find the matching feature, information about the motion of the camera is used to find where the feature is most likely, and that area is searched first. The feature from the current right frame is then matched to the current left frame, again along a narrow horizontal corridor. Finally this feature is matched to the previous left frame, completing a circle through all of the current set of four frames. If the feature is matched back to the same feature that was used initially, the match is good, as the feature can be seen in each frame so it can be used to reconstruct motion. This process is shown in Figure III.IX.

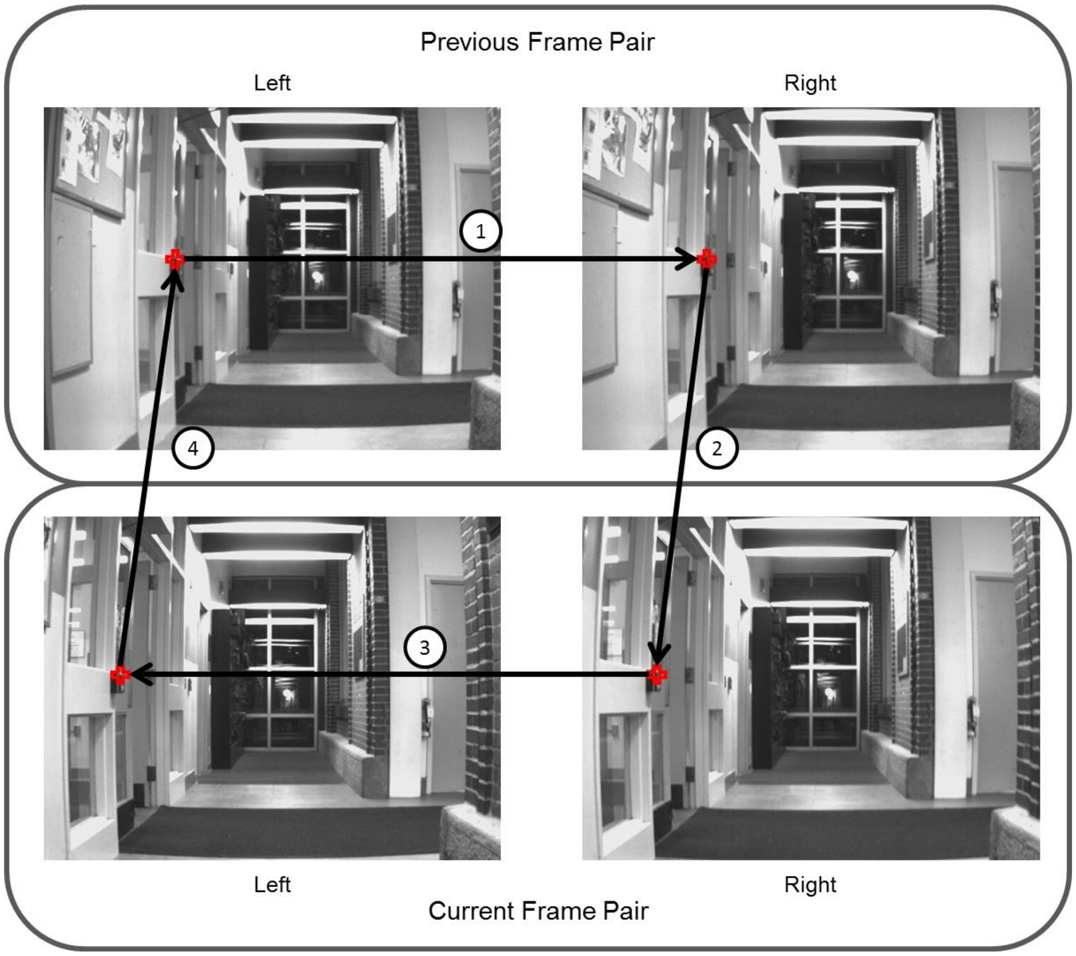

Figure III.IX: Circular Matching

III.II.IV RANSAC

RANSAC is used to remove bad feature matches so that a successful motion reconstruction can be made from only good matches. After the matcher has returned a list of matches and has thinned them out based on some basic density parameters, the list of matches is sent to RANSAC which builds random groups of these matches, and attempts to create motion data from these groups. This implementation of RANSAC uses only three matches to make the initial motion estimate, and then attempts to add more matches to this estimate. If enough other matches fit this motion estimate, it is considered good and the algorithm stops. Otherwise RANSAC will run up the maximum allowed number of iterations, in this case 200, and at the end take the motion estimate that had the most corresponding matches.

III.III Non-Linear Kalman Filter Approximation

The Extended Kalman Filter (EKF) or Non-Linear Kalman Filter was used to generate a state estimate by fusing and filtering data from both the visual odometry subsystem and the IMU. The EKF started by making a prediction of where the system will be in the current time step based off the state vector of the previous time step and the state transition matrix. This prediction was then compared to the measurements of the current time step and calculated using the Kalman gain and covariance matrix of the system. The visual odometry subsystem provided the EKF with the linear velocity in the three axes of the body-frame. The visual odometry was also capable of providing angular velocity but this measurement is less accurate when compared to that of the IMU. The IMU provides the EKF with linear acceleration and angular velocity, both in the body frame of reference. With these several sensor measurements, predictions become much more accurate, despite the low sampling rate of the visual odometry subsystem. More accurate predictions result in more effective noise removal and therefor closer estimations of the systems true movement.

Listed below are the different equations, matrices, and vectors needed for the EKF. The subset for each variable corresponds to the x, y, or z component of that variable. P_x is the position in the x direction. v_x is the velocity in the x direction. a_x is the acceleration in the x direction. θ_x is the angle about the x-axis. $\dot{\theta}_x$ is the change in the angle about the x-axis. Figure III.XVIII shows the state and measurement vectors. The state vector shows all of the variables that are estimated and the measurement vector shows all of the measurements that are received from the cameras and IMU. Figure III.XI shows the observation versus estimation matrix. This matrix compares what information is received from the cameras and IMU to the variables that are estimated. Figure III.XII displays the state transition matrix of the system using the dynamic equations shown in Figure III.XIII. The time step *dt* in these equations and matrices is determined by the update rate of the IMU due to its much faster sampling rate than that of the visual odometry subsystem. The dynamic equations listed below are in terms of the x-axis but can be extended to the y and z axes.

$$x_k = \begin{bmatrix} P_x \\ P_y \\ P_z \\ v_x \\ v_y \\ v_z \\ a_x \\ a_y \\ a_z \\ \theta_x \\ \theta_y \\ \theta_z \\ \dot{\theta}_x \\ \dot{\theta}_y \\ \dot{\theta}_z \end{bmatrix} \qquad y_{k=} \begin{bmatrix} v_x \\ v_y \\ v_z \\ a_x \\ a_y \\ a_z \\ \dot{\theta}_x \\ \dot{\theta}_y \\ \dot{\theta}_z \end{bmatrix}$$

Figure III.X: State and Measurement Vectors

$$H = \begin{bmatrix} 0&0&0&1&0&0&0&0&0&0&0&0&0&0&0 \\ 0&0&0&0&1&0&0&0&0&0&0&0&0&0&0 \\ 0&0&0&0&0&1&0&0&0&0&0&0&0&0&0 \\ 0&0&0&0&0&0&1&0&0&0&0&0&0&0&0 \\ 0&0&0&0&0&0&0&1&0&0&0&0&0&0&0 \\ 0&0&0&0&0&0&0&0&1&0&0&0&0&0&0 \\ 0&0&0&0&0&0&0&0&0&0&0&0&1&0&0 \\ 0&0&0&0&0&0&0&0&0&0&0&0&0&1&0 \\ 0&0&0&0&0&0&0&0&0&0&0&0&0&0&1 \end{bmatrix}$$

Figure III.XI: Observation vs. Estimation Matrix

$$F = \begin{bmatrix} 1 & 0 & 0 & dt & 0 & 0 & .5dt^2 & 0 & 0 & 0 & 0 & 0 & 0 & 0 & 0 \\ 0 & 1 & 0 & 0 & dt & 0 & 0 & .5dt^2 & 0 & 0 & 0 & 0 & 0 & 0 & 0 \\ 0 & 0 & 1 & 0 & 0 & dt & 0 & 0 & .5dt^2 & 0 & 0 & 0 & 0 & 0 & 0 \\ 0 & 0 & 0 & 1 & 0 & 0 & dt & 0 & 0 & 0 & 0 & 0 & 0 & 0 & 0 \\ 0 & 0 & 0 & 0 & 1 & 0 & 0 & dt & 0 & 0 & 0 & 0 & 0 & 0 & 0 \\ 0 & 0 & 0 & 0 & 0 & 1 & 0 & 0 & dt & 0 & 0 & 0 & 0 & 0 & 0 \\ 0 & 0 & 0 & 0 & 0 & 0 & 1 & 0 & 0 & 0 & 0 & 0 & 0 & 0 & 0 \\ 0 & 0 & 0 & 0 & 0 & 0 & 0 & 1 & 0 & 0 & 0 & 0 & 0 & 0 & 0 \\ 0 & 0 & 0 & 0 & 0 & 0 & 0 & 0 & 1 & 0 & 0 & 0 & 0 & 0 & 0 \\ 0 & 0 & 0 & 0 & 0 & 0 & 0 & 0 & 0 & 1 & 0 & 0 & dt & 0 & 0 \\ 0 & 0 & 0 & 0 & 0 & 0 & 0 & 0 & 0 & 0 & 1 & 0 & 0 & dt & 0 \\ 0 & 0 & 0 & 0 & 0 & 0 & 0 & 0 & 0 & 0 & 0 & 1 & 0 & 0 & dt \\ 0 & 0 & 0 & 0 & 0 & 0 & 0 & 0 & 0 & 0 & 0 & 0 & 1 & 0 & 0 \\ 0 & 0 & 0 & 0 & 0 & 0 & 0 & 0 & 0 & 0 & 0 & 0 & 0 & 1 & 0 \\ 0 & 0 & 0 & 0 & 0 & 0 & 0 & 0 & 0 & 0 & 0 & 0 & 0 & 0 & 1 \end{bmatrix}$$

Figure III.XII: State Transition Matrix

$$\hat{P}_x = P_x + v_x * dt + 0.5 * a_x * dt^2$$

$$\hat{v}_x = v_x + a_x * dt$$

$$\hat{a}_x = a_x$$

$$\hat{\theta}_x = \theta_x + \dot{\theta}_x$$

$$\hat{\dot{\theta}}_x = \dot{\theta}_x$$

Figure III.XIII: Dynamic Equations

The EKF was first written in MATLAB due to the ease of plotting data and running tests. The MATLAB starts by loading in the data from the cameras and the IMU. The cameras provide position in meters and heading in degrees for the x, y, and z directions. The IMU provides acceleration in meters per second squared and change in heading in degrees in the x, y, and z directions. The z direction is forward and backward. The y direction is up and down. The x direction is left and right. The buffer size and change in time are set next. The buffer size is the size of the IMU data set. The variable *dt* is set to the IMU time difference because the IMU and camera data needs to be synced and the IMU has a faster sampling rate than the camera.

Next, state variables are initialized using the first data points from the camera and IMU data sets. The position variables are initialized to zero. The initial state vector is initialized to these initial state variables and the initial covariance matrix is set up to a 15x15 identity matrix. Next, matrix x_k and vector x_p are initialized. x_k is a matrix that stores the iterations of the state vector. x_p is the state vector after the predict state also called a priori. One iteration of x_k (state vector) is depicted in Figure III.X. Matrix P_k and P_p are initialized next. P_k is a matrix that stores the iterations of the covariance matrix. P_p is the covariance matrix after the a priori state. The variables Q and R are set next. Q is the matrix for the process noise. This matrix only has values along the diagonal and zeroes everywhere else. These values can range from 0.1 to 0.2 and are adjusted to help correct the output. R is the matrix for measurement noise. This matrix also only has values along the diagonal and zeroes everywhere else. The values are based off of the noise properties for the camera and IMU based on their data sheets. The y_k matrix is set up next, which holds the iterations of the measurement vector and one iteration (measurement vector) is shown in Figure III.X. The H matrix is then set up which tells the system what are the observed states and which are the estimated states as shown in Figure III.XI. This matrix is used in the a posteriori state to choose only the values that are measured.

The MATLAB code then enters a *for* loop, which runs through all of the data points in the data sets. The loop starts by updating the state transition matrix. This matrix holds the dynamic equations used to predict the next state. These equations are nonlinear because the modeled system itself is nonlinear. These dynamic equations are shown in Figure III.XIII and the state transition matrix is shown in Figure III.XII.

```
%Predict / a priori
    %state equation
    xp = F*xk(:,i-1);

    %covariance of the estimation error
    Pp = (F*Pk(:,:,i-1)*F') + Q;
```

Figure III.XIV: ***a priori*** **state**

The next state is the predict state, also called *a priori*. This state predicts where the system will be in the next iteration. The MATLAB code is shown in Figure III.XIV. The first equation is the state equation, which makes the prediction. The second equation is used to update the covariance matrix. The covariance matrix is used to tell the Kalman Filter how much confidence there is in the specific value. These numbers range from zero to one with zero being very confident and one being not confident.

Next is the update state also called *a posteriori*. This state corrects the values predicted in the *a priori* using the measurement data taken in from the cameras and IMU. Figure III.XV shows the *a posterior* state. The measurement data is collected before these steps. The Kalman gain is calculated first. Then the state vector is corrected using the new measurement data. The covariance matrix is also corrected using the new measurement data. The MATLAB code ends by plotting the position data of the state vector.

```
    %Update / a posteriori

    K = (Pp*H')*(pinv(((H*Pp)*H')+R)); %Kalman Gain
    xk(:,i) = xp + K*(yk(:,i)-H*xp); %Updated state vector
    Pk(:,:,i) = Pp-K*H*Pp; %Updated covariance of the estimation error
```

Figure III.XV: ***a posteriori*** **state**

III.III.I Data Transformation

The accelerometer and gyroscope within the IMU are integral parts of this project. Like the camera, they assist in the tracking of position and orientation. They are able to do this in much less time with much less complicated processing than the camera system. Both of them serve as inputs to the Kalman Filter by providing the angular rate of change and linear acceleration. Before they can be processed by the Kalman Filter, they must be translated from the local, or body frame, to the global frame. This is accomplished by keeping track of the angular orientation of the system in relation to the global axes. The angular orientation can be described by the three Euler angles of roll, pitch, and yaw as shown in Figure III.XVI. By converting the accelerometer measurements to the global frame, gravity can be removed by subtracting 9.8 m/s2 from the y-axis acceleration.

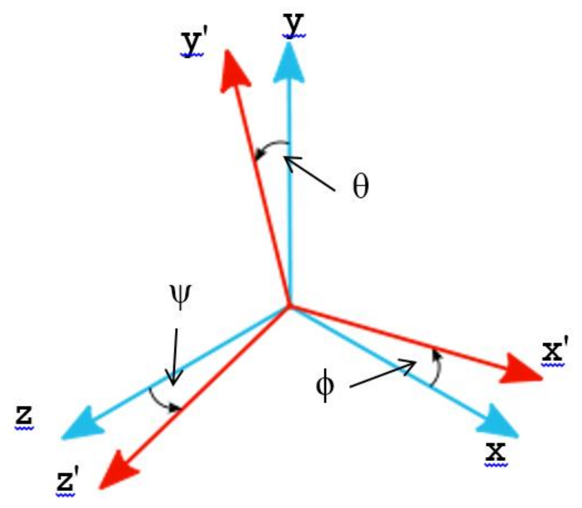

Figure III.XVI: Axis Definition

Gyroscope and Accelerometer Rotation Matrix

The rotation of a body in 3D space is represented using Euler angles convention, in which φ is the rotation of the system about the global z-axis, θ is the rotation about the x-axis and φ is the rotation about the y-axis. The gyro rates are transformed to global frame using the following rotational matrix for Euler angle rates.

$$\begin{bmatrix}\dot{\psi}\\ \dot{\theta}\\ \dot{\varphi}\end{bmatrix} = \begin{bmatrix}0 & cos\varphi & -sin\varphi\\ 0 & sin\varphi/cos\theta & cos\varphi/cos\theta\\ 1 & sin\varphi * tan\theta & cos\varphi * \tan\theta\end{bmatrix} * \begin{bmatrix}\dot{\psi}'\\ \dot{\theta}'\\ \dot{\varphi}'\end{bmatrix}$$

Equation III.I: Gyroscope Rotation Matrix from Figure III.XVI

Because the above equation requires the global orientation in order to calculate the global change in orientation, a previous calculation or estimation of heading is required. In our design, the predicted heading produced within the Kalman filter was used.

Likewise, the acceleration component in each global dimension is computed from a rotation matrix described in Equation III.IV and Equation III.II. The headings used to compute the Body Rotation Matrix can either be calculated by integrating the change in each heading calculated in Equation III.I or by using the predicted heading of the Kalman filter. In order to stay consistent with the calculation of the global angular velocities, the predicted heading from the Kalman filter is used.

$$C_b^n = \begin{bmatrix}\cos(\theta)\cos(\psi) & -\cos(\phi)\sin(\psi)+\sin(\phi)\sin(\theta)\cos(\psi) & \sin(\phi)\sin(\psi)+\cos(\phi)\sin(\theta)\cos(\psi)\\ \cos(\theta)\sin(\psi) & \cos(\phi)\cos(\psi)+\sin(\phi)\sin(\theta)\cos(\psi) & -\sin(\phi)\cos(\psi)+\cos(\phi)\sin(\theta)\sin(\psi)\\ -\sin(\theta) & \sin(\phi)\cos(\theta) & \cos(\phi)\cos(\theta)\end{bmatrix}$$

Equation III.II: Body Rotation Matrix from Figure III.XVI

$$\begin{bmatrix}v_z\\ v_x\\ v_y\end{bmatrix}_{global} = C_b^n * \begin{bmatrix}v_z\\ v_x\\ v_y\end{bmatrix}_{body}$$

Equation III.III: Body-to-Global Velocity Transformation

$$\begin{bmatrix} a_z \\ a_x \\ a_y \end{bmatrix}_{global} = C_b^n * \begin{bmatrix} a_z \\ a_x \\ a_y \end{bmatrix}_{body}$$

Equation III.IV: Body-to-Global Acceleration Transformation

III.III.II Noise and Data Weighting

The weighting of the data allows the system to decide which input data it should rely on more over others. Weighting of the data occurs in the covariance matrix. These values range from zero to one. The closer the values are to zero the more confident the EKF is in that value. The EKF then uses equations to appropriately change the covariance matrix to fit the desired need of the system. Covariance matrices are usually initialized to be an identity matrix.

There will always be white Gaussian noise associated with data coming from the sensors. The Q and R noise matrices are used to best understand this noise. The Q matrix, called process noise, is used to represent the noise that is introduced when predicting the next state. The R matrix, called measurement noise, is used to represent the noise produced by the sensors of the system. To find the appropriate values for these matrices, our system was left sitting still for a fixed period of time. This data set consisted of measurements for all of the different inputs of the system. The measurements of velocity, acceleration, and angular velocity had a mean value of zero. The standard deviation was taken on each of these inputs. These standard deviations were then squared and used as the values for the R matrix to best model the noise coming from the sensors of the system. The Q matrix uses these values for the measured variables and deriving the values for the unmeasured variables.

III.IV Power Management

There are several different voltage levels required in the system. The OMAP EVM has internal voltage regulators that accept any voltage from five to fifteen volts at one amp or less. The Capella Camera requires five volts at one amp. As discovered in testing, the IMU needs a very clean power supply that can support the 1.5 A transient as it turns on. To meet these requirements, two switching regulators were chosen to supply the 3.3 V and 5 V regulated voltages for the IMU and Capella. As the EVM would be regulating its input voltages, it was connected directly to the unregulated input voltage. Both the XBee wireless transceiver and the Arduino would be powered off the EVM's 5 V USB bus power. A top level block diagram of the power management system is shown in Figure III.XVII.

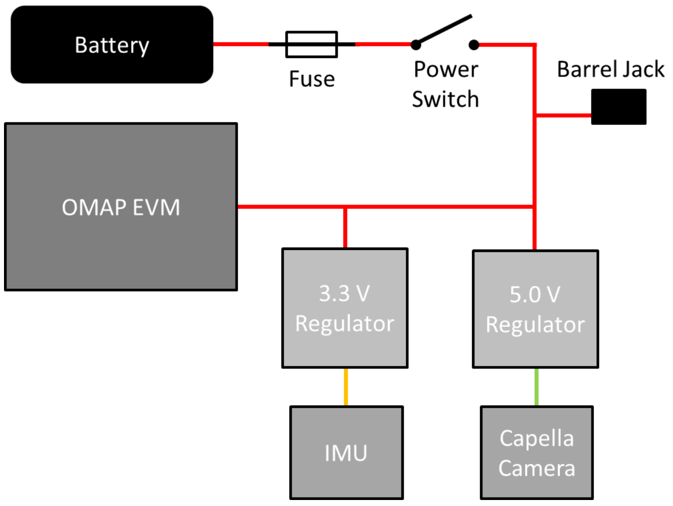

Figure III.XVII: Power Management block diagram

III.IV.I Switching Regulators

To speed the development process, off the shelf switching regulators were chosen. As each regulator only had to power one device, determining max current draw was relatively straight forward. The peak current requirements for each of the regulators are shown below.

Table III.I: Peak current draw for voltage regulators

3.3 V Regulator		5.0 V Regulator	
IMU	1.5 A	Capella Camera	1 A

It was decided to use D15V35F5S3 switching regulator modules from Pololu, a manufacturer of parts for hobby robotics. The regulator has a small form factor, can be plugged into a protoboard, and has a selectable output voltage to either 3.3 V or 5 V. Because of this, the same type of regulator could be used for both supplies. The regulators have a high efficiency, approximately 90% for both with an input voltage of 7.2 V and under the given load conditions. The efficiency curves for each of the regulators are shown below in Figure III.XVIII. The regulators were mounted on a custom protoboard which provided them with terminals to connect to the various subsystems that required regulated voltages.

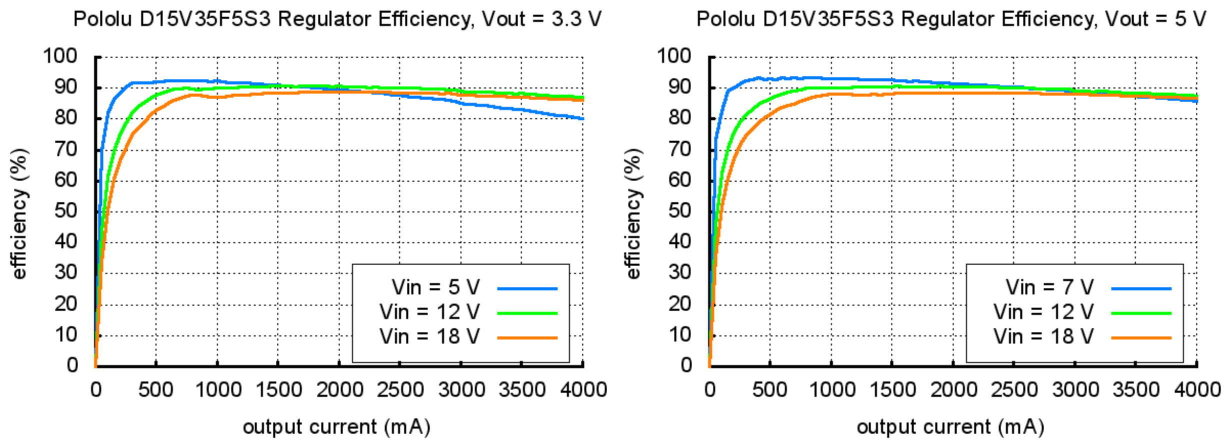

Figure III.XVIII: Efficiency of 3.3 V regulator (left) and 5.0 V regulator (right)

III.IV.II Battery

To allow for mobility, the system needed to be powered by a battery. The highest input voltage allowable was 15 V, limited by the voltage regulator on the EVM. The minimum voltage allowable was 6.5 V, limited by the dropout voltage of the 5 V regulator. Given these voltage requirements, a 7.2 V nickel-metal hydrate, or NI-MH battery was a chosen. The necessary capacity for the battery was then determined by estimating the current draw of the system for a typical case. Although all of the other current draw analysis was done for the worst case, that does not give a reasonable estimation for battery life, as most of the components do not run at their worst case current draw for the entire time. This is especially true for the IMU, which has a startup transient of 1.5 A, but only draws 200 mA during regular operation. To determine current draw from the regulators, the following equation was used.

$$I_{in} = \frac{I_{out} \cdot V_{out}}{E \cdot V_{in}}$$

Equation III.V: Input Current Calculation

In the above equation, *E* is the efficiency of the regulator, in this case estimated at 85%. The current estimate for the typical case is then shown below.

Table III.II: System current draw estimate

Device	Current Draw (A)
OMAP EVM	0.8
3.3 V Regulator	0.1
5 V Regulator	0.6
Total	1.5

III.IV.III Safety Measurements

In order to prevent the battery from being damaged in the event of a short circuit, a fuse was placed in the positive power supply line. The fuse is rated for 5 A, to allow for regular operation, which can reach two amps, and also allow for enough overhead for startup transients or other short spikes in power usage. Additionally, each of the Pololu voltage regulators had a built in over-current shutdown feature, which would cause them to turn off in the event of a current draw beyond their capacity.

III.V User Interface

The system must be capable of displaying or communicating the tracked position and orientation of the system. An initial design implemented an LCD on the system that displayed a numerical representation of the position and heading. The group decided this setup would be too costly and add more work and possible problems to the project. Instead our design implements a wireless transceiver that can be used to transmit the information to a second system that can display or process the information in any way the user wishes.

III.V.I Wireless Radio Communication

The design implements a transceiver that transmits the data from the mobile system as a frame as well as a transceiver that reads in the frames to a computer. The frames include the x, y, and z positions as well as the pitch, yaw and roll. The frames have the following comma delimited structure:

[x-position], [y-position], [z-position], [pitch], [yaw], [roll] Wireless transceivers enable data to be transmitted in both directions, allowing commands to be sent to the system. These commands may include asking the system to report its position, zero its position and heading, and anything else deemed important. The system could also be implemented in a spoke-hub structure, in which multiple odometry systems report their locations and orientations to a central receiver. This would be very useful for search and rescue and military operations.

Chapter IV. System Implementation

This chapter will discuss the realized implementation of the system design presented in Chapter III. The top level system implementation diagram is provided by Figure IV.I. The stereoscopic capabilities are provided by E-con System's Capella Stereo Vision Camera Reference Design. The system uses Analog Device's ADIS16375 IMU for collecting acceleration and rotation data to support the camera. The Arduino Uno parses the raw IMU data and feeds the output through a Virtual Com Port (VCP). The OMAP5432 Evaluation Module provides the core functionality to the system and acts as the communications manager between the other peripherals. Feature detection and matching, local to global coordinate transformation, and Kalman filter approximations are all performed on the OMAP5432. The power management unit splits the 7.2V battery supply to 3.3V and 5V respectively. It also contains a power on/off switch and a safety fuse. The XBee Wireless Transceiver and Receiver pair provides the principal means of communications between the system and the target computer. The primary means of communication between the peripherals and the central processor is through the serial port drivers provided by the OMAP5432 EVM.

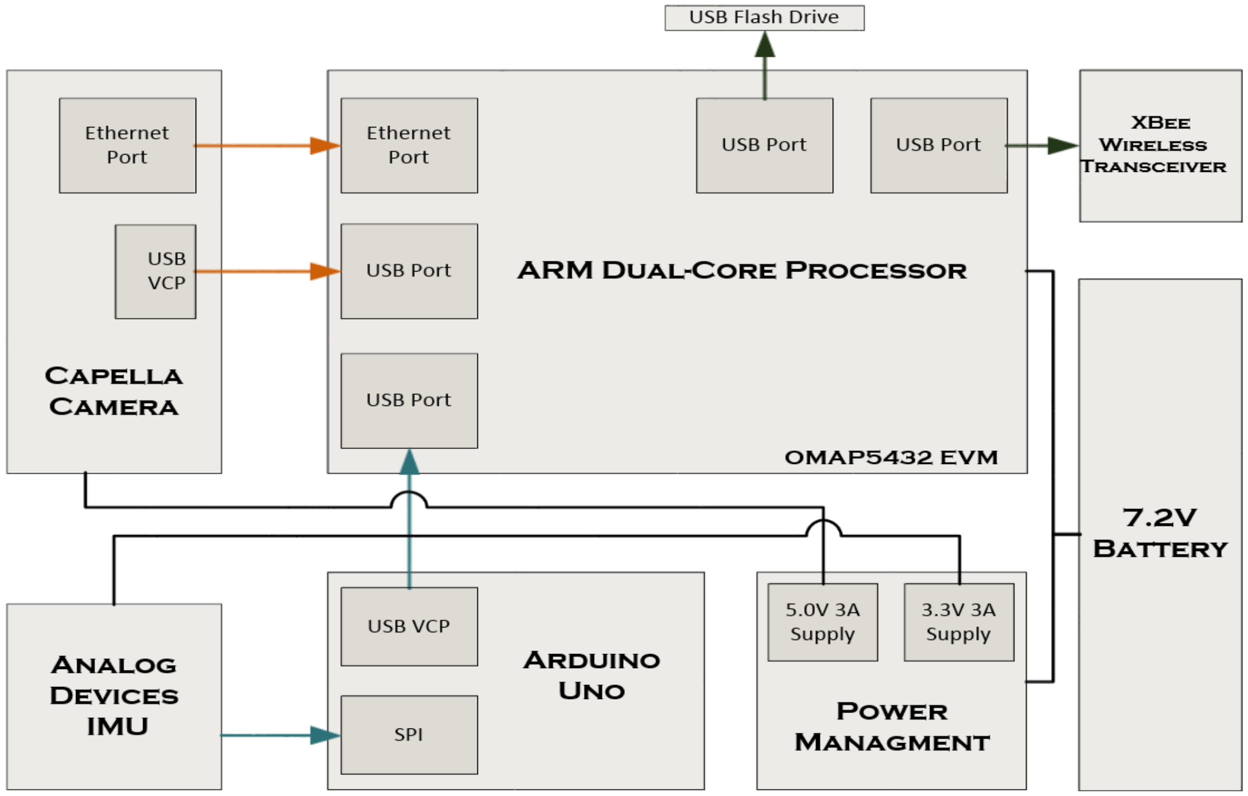

Figure IV.I: Top level system implementation

IV.I Capella Camera Stereo Vision System

The Capella camera is an embedded Stereovision reference design for the TI OMAP35x and DM37x line of processors. The Capella is targeted towards customers seeking to integrate Stereovision capabilities in a product design, and rapid prototyping of stereovision camera algorithms. At $1,299 the Capella camera is one of the more affordable global shutter systems for obtaining stereovision capabilities. The Capella communicates with the OMAP5432 processor via a USB serial port and an Ethernet connection. The Ethernet connection is used for transmission of the video stream from the camera to the processor. The serial port is used to run the initialization scripts on the camera processor. The Capella comes with a preinstalled Linux kernel containing the camera drivers and various camera applications. The Linux kernel also provides the potential for extending the cameras functionality to meet our requirements. Refer to Appendix A.III for documentation on setting up and using the camera.

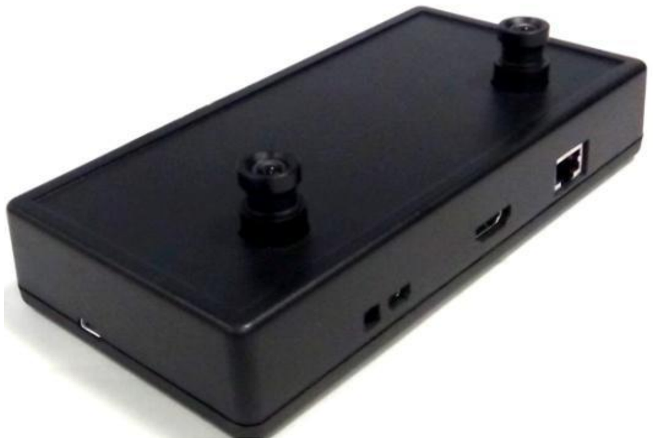

Figure IV.II: Capella Stereo Vision Camera Reference Design

IV.I.I Specifications

Table IV.I provides the specifications for the Capella Camera. The primary benefits of the Capella is the fairly low voltage power requirement as well as the Linux 2.6.35 kernel which allows for streamlined communication between the Overo processor (OMAP35x architecture) on the camera and the OMAP5432 EVM.

Table IV.I: Capella Camera Specifications and Features

SPECIFICATIONS AND FEATURES	
FRAME RATE	30 fps
RESOLUTION	736x480 (per camera) ,1472x480 (combined camera resolution)
IMAGE FORMATS	8-bit greyscale format
LENS TYPE	Factory calibrated S-mount lens pair with lock-nut and S-mount lens holder
BASELINE	100mm (adjustable on request)
CAMERA BOARD	E-CAM 9v024 Stereo
CAMERA	1/3" Global shutter MT9V024 image sensor
OUTPUT FORMAT	WVGA 752(H) x 480(V) (360690 pixels) sensors output 736(H)x480(V) images in 8-bit greyscale format
INTERFACE	27 pin FPC connector to Gumstix Overo WaterSTORM COM, HDMI-DVI cable, USB type A to Mini B cable, Ethernet port
DRIVERS	Standard V4L2 compliant drives with associated API'S
SOFTWARE	Linux 2.6.35 kernel, OpenCV for depth measurement
POWER SUPPLY	5V, 1A
PRICE	$1,299.00

IV.I.II File Transfer Protocol (FTP) Network

The Capella operating system came with a pre-installed FTP server with the intention of transferring files to and from the camera. As the user does not have direct access to the SD card containing the Capella OS file system, the FTP network is the primary means by which the user can modify the Operating system. The user must first specify the IP (internet protocol) address of the camera, at which point the receiving computer may access the camera file system with an FTP client.

IV.I.III GStreamer Multimedia Framework

The only means of outputting the video stream externally provided natively by the Capella Camera is through the HDMI out port. The OMAP5432 EVM processor does not contain an HDMI in port, and as such additional functionality has to be provided to the Capella Camera. The GStreamer Multimedia Framework is an open-source library that allows for the manipulation, processing, and streaming of video and audio sources. Building and installing GStreamer on the Capella camera provided the capability to stream the camera feeds to a different computer through a local Ethernet connection. In order to do this, corresponding GStreamer pipelines are initiated on both the host (Capella) and the receiving (OMAP5432) computers. For further detail on building GStreamer and constructing pipelines refer to Appendix A.III.

GStreamer Streaming Host Pipeline

The GStreamer host pipeline is run on the Capella Camera. The pipeline opens the video streams from the left and right cameras and formats the raw video as 640x480 grayscale streams transmitting at 5 frames per second. The pipeline then gives the streams a color space and payloads the stream for Real-time Transport Protocol (RTP) format. Finally the pipeline defines a UDP (User Datagram Protocol) port for each stream and transmits them at the user specified IP address. Figure IV.III provides a flow diagram of the host pipeline.

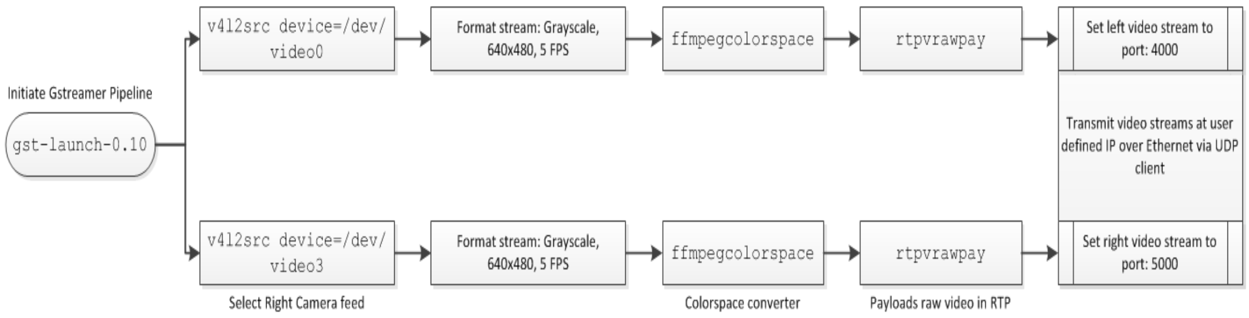
Initiate Gstreamer Pipeline
gst-launch-0.10
v4l2src device=/dev/video0
Format stream: Grayscale, 640x480, 5 FPS
ffmpegcolorspace
rtpvrawpay
Set left video stream to port: 4000
Transmit video streams at user defined IP over Ethernet via UDP client
v4l2src device=/dev/video3
Format stream: Grayscale, 640x480, 5 FPS
ffmpegcolorspace
rtpvrawpay
Set right video stream to port: 5000
Select Right Camera feed
Colorspace converter
Payloads raw video in RTP

Figure IV.III: GStreamer host pipeline flow diagram

GStreamer Receiver Pipeline

The GStreamer receiver pipeline is run on the OMAP5432 EVM. This pipeline connects to the UDP network set up by the host pipeline and opens the respective video ports. The pipeline capabilities are based upon the verbose outputs of the host pipeline. Afterwards the video streams are de-payloaded and converted back into the same color space. Each incoming frame is then encoded as a JPEG image and saved into a folder to be accessed by the feature detection algorithm. Figure IV.IV provides a flow diagram of the receiver pipeline.

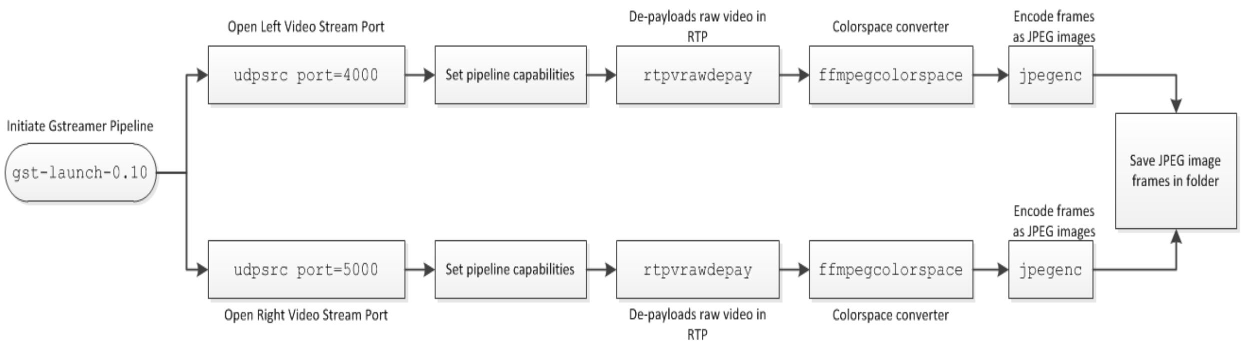
Initiate Gstreamer Pipeline
gst-launch-0.10
Open Left Video Stream Port
udpsrc port=4000
Set pipeline capabilities
De-payloads raw video in RTP
rtpvrawdepay
Colorspace converter
ffmpegcolorspace
Encode frames as JPEG images
jpegenc
Save JPEG image frames in folder
Open Right Video Stream Port
udpsrc port=5000
Set pipeline capabilities
De-payloads raw video in RTP
rtpvrawdepay
Colorspace converter
ffmpegcolorspace
Encode frames as JPEG images
jpegenc

Figure IV.IV: GStreamer receiver pipeline flow diagram

IV.II ADIS16375 IMU Interface

The ADIS16375 is a high-end IMU that has a tri-axis gyroscope with range of ±3000 degrees per second and a tri-axis accelerometer with range of ±18 g. It was donated for the research project by Analog Devices so the group could make use of a high quality IMU for the project despite the high price. The IMU has a MEMS angular rate sensor, a MEMS acceleration sensor and an embedded temperature sensor. The outputs from the sensors are written to a thirty two bit output registers after calibration for bias which gives high precision measurement values. The IMU module is compact and has dimensions of 44 by 47 by 14 mm. Analog Devices provided a prototype interface board that comes with larger connectors than the connector on the IMU to facilitate prototyping. Figure IV.V below shows the IMU and the prototype board. The following sections describe IMU axis, SPI bus for interfacing IMU with processor and power requirements of the IMU.

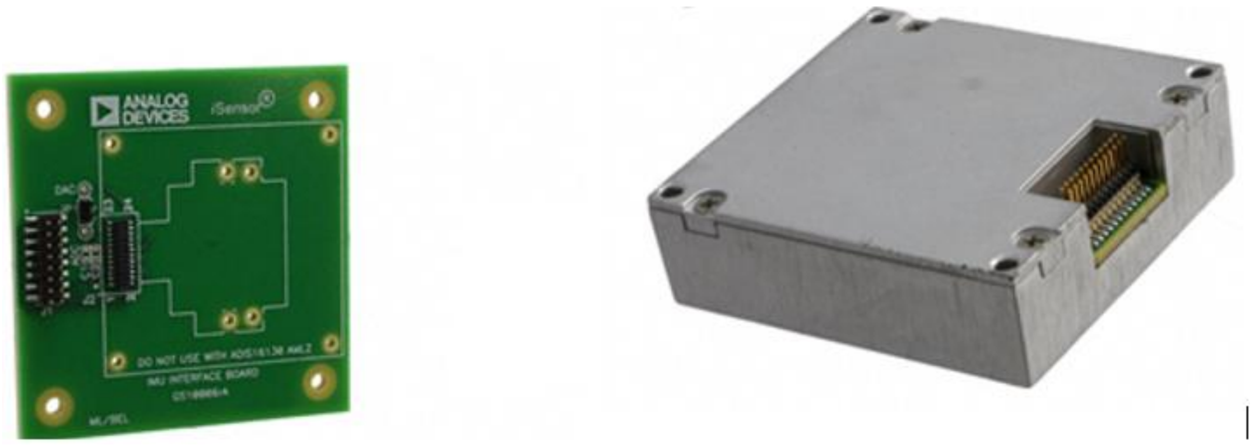

Figure IV.V: ADIS16375 IMU and prototype interface board

IV.II.I IMU Frame of Reference

The IMU coordinate axis is shown in Figure IV.VI below. The data collected using the IMU is converted from the IMU frame of reference to the system's frame of reference using the rotational matrix in Equation IV.I.

$$\begin{bmatrix} x_{imu} \\ y_{imu} \\ z_{imu} \end{bmatrix} = \begin{bmatrix} 0 & 1 & 0 \\ 0 & 0 & 1 \\ 1 & 0 & 0 \end{bmatrix} \times \begin{bmatrix} x_{system} \\ y_{system} \\ z_{system} \end{bmatrix}$$

Equation IV.I: IMU transformation matrix

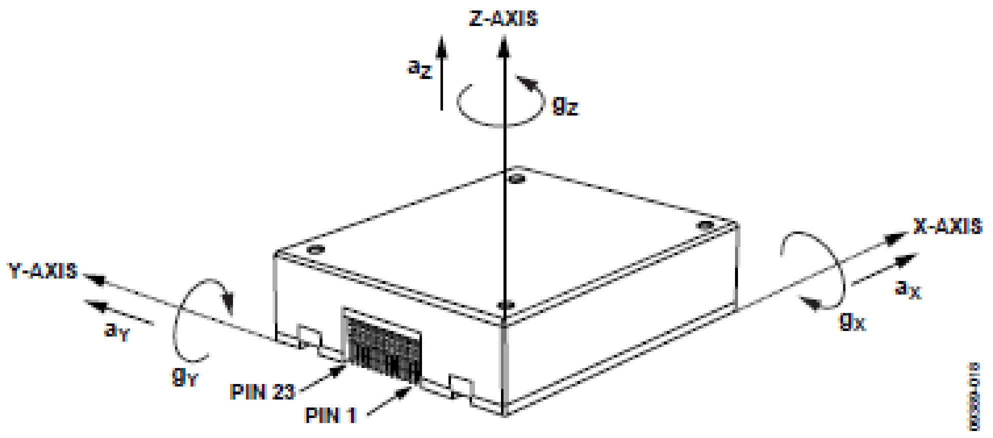

Figure IV.VI: ADIS IMU frame of reference

IV.II.II Power Requirements

Table IV.II below shows the power requirements of the IMU and Arduino as per their datasheet. The IMU is powered by a 7.6 V Lithium-ion-polymer battery by stepping down the battery output to 3.3 V using a D15V35F5S3 adjustable regulator. Arduino is powered through the OMAP EVM through a USB port. IMU- Arduino integration in the final system is shown in a block diagram in section.

Table IV.II : Power requirements of IMU

Parameter	ADIS16375	Arduino
Operating voltage	3.3 V	5 V
Power supply current	173 mA	200 mA
Transient currents	1.5 A	

IV.II.III SPI (Serial Peripheral Interface)

The IMU has a SPI compatible serial interface to connect it to an embedded system SPI is a synchronous serial data link that operates in full duplex communication. SPI has four main lines- slave select, serial clock, master out slave in (MOSI) and master in slave out (MISO). In the system, the embedded processor is the master and the IMU is the slave device. The master generates the serial clock which sets the speed of the link, initiates the data frame and selects the slave device by setting the slave select (SS in the figure below) low.

The OMAP has four SPI modules and the OMAP EVM breakout header has pins that provide access to SPI module 2 in the OMAP. To register the SPI slave device with the OS, the Linux kernel requires a device tree file. The device tree is a structure of nodes and properties. Each device connected to the CPU is represented as a node and has a compatibility property which enables the operating system to decide which device driver to bind to a device. It was not feasible to interface the IMU directly with the OMAP processor because the device tree file for the OMAP was not found in the Ubuntu Linux distribution installed on the OMAP EVM. Given the time constraints and lack of documentation on how to implement a device tree for SPI, this option was abandoned. As a workaround we used an Arduino Uno board as a medium between the IMU and the OMAP. The Arduino Uno is a development board based on the ATmega328. The IMU connects to the Arduino via SPI and the IMU data is parsed in the Arduino, and printed to a serial port at baud rate of 115200 baud. The Arduino has built in SPI drivers which made it convenient to interface the IMU with the Arduino. The IMU and the Arduino SPI settings are shown in the table below.

Table IV.III: SPI specifications for ADIS16375 and Arduino Uno

Setting	ADIS 16375	Arduino
	Slave	Master
SCLK	≤15 MHz	8 MHz
SPI Mode	SPI Mode 3 CPOL=1 and CPHA=1	SPI Mode 3
Bit Sequence	MSB first	MSB first

The Arduino is the master device that generates system clock at a rate of 8 MHz and controls the data coming in and out of the IMU which is the slave device. Data is shifted with the most significant bit (MSB) shifting out first. The IMU and the Arduino communicate in SPI mode three. In mode three, data is captured on the clock's rising edge and data is propagated on a falling edge.

IV.II.IV IMU Interface

A level shifter circuit was developed to interface the Arduino Uno with the ADIS IMU. The shifter connects SPI signals between the devices. The minimum digital high voltage that can be read by the Arduino is 3 V and the minimum digital high voltage guaranteed by the IMU is 2.4 V. For this reason a level shifter circuit was designed to shift the IMU output to 5V so that Arduino could read in IMU data. The schematic for the level shifter is shown in the figure below. The level shifter consists of two NPN BJT transistors and four current limiting resistors. The first NPN shifts the input voltage to 5 V but the signal is inverted. The second NPN reverses the output of first NPN transistor and the output of the level shifter is the original signal shifted to 5 V.

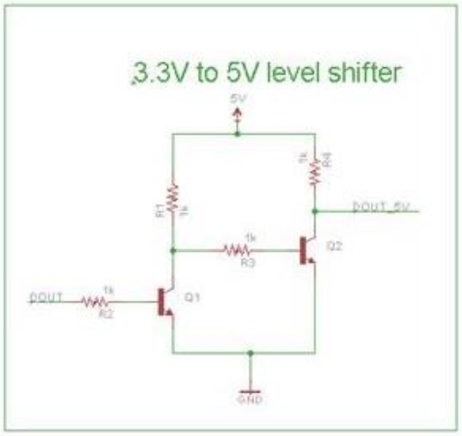

Figure IV.VII: Level shifter schematic

The Arduino shield also has an FTDI chip that converts the serial data coming from Arduino to USB signals so that the FTDI drivers installed on the processors could read the data sent from Arduino. Furthermore, Python module pySerial was installed on the OMAP. pySerial provides a back end for Python running on Windows and Linux to provide access to serial port. A python script was developed to read serial data coming from serial port on the OMAP and save the data in a text file.

IV.II.V IMU Data Transmission

In the final system implementation, the Arduino reads in data from IMU at a frequency of 100 Hz using a hardware timer with a period of 10ms. The Arduino script initializes a 16 bit internal hardware timer called 'Timer 1'. The Interrupt Service Routine flags the interrupt from Timer 1. A loop constantly checks for the flag and when the interrupt is flagged, a new measurement is read from the accelerometer, gyroscope and temperature sensor in the IMU. The data is transmitted by serial communication to the processor in the following comma delimited data format in which the second, third, and fourth measurements are angular velocities and the last three measurements are accelerations.

$$[\text{temperature}, \dot{\varphi}, \dot{\theta}, \dot{\psi}, , a_z, a_x, a_y]$$

The plot of the integrated gyroscope measurements from the experiment is shown in the figure below. Ninety degree turns were estimated accurately as shown in Figure IV.VIII. The plots show that the system can read in sensor values accurately at precise time intervals to get accurate estimation of headings from the measurements.

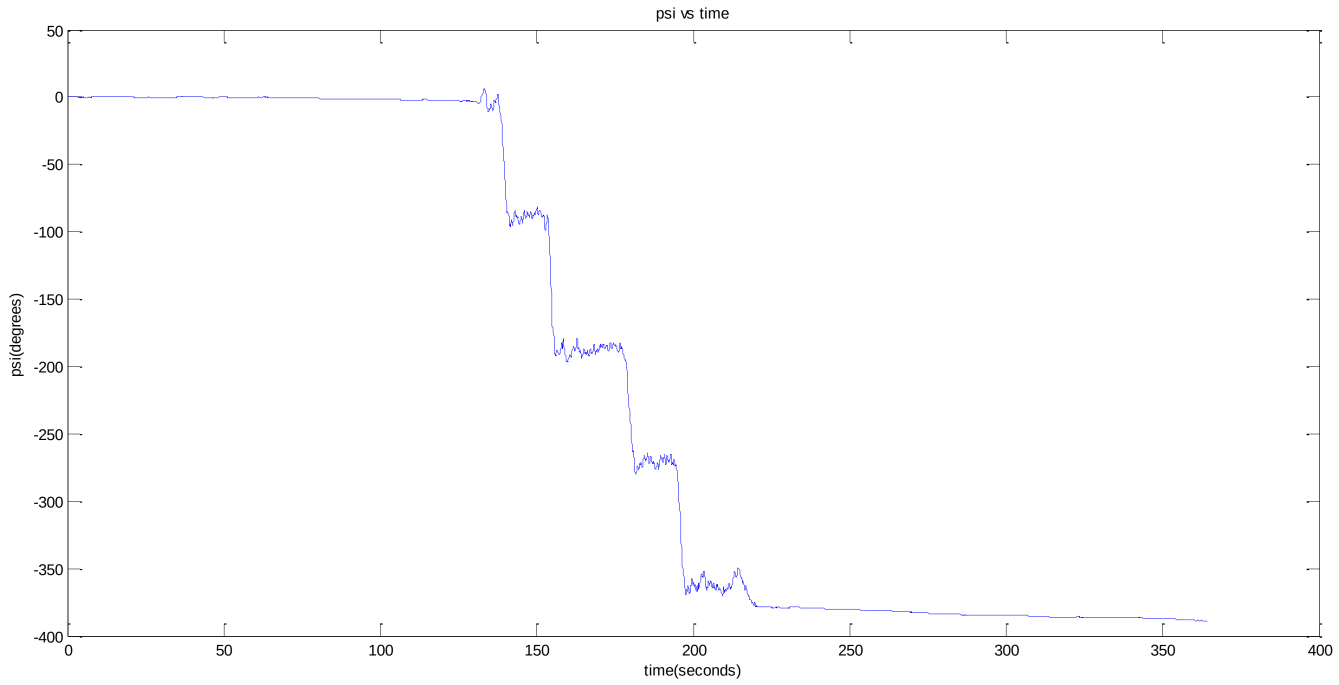

Figure IV.VIII: Ninety degree rotations about Z axis

IV.III Kalman Filter on the ARM Platform

A C++ implementation of the EKF has been designed to run on the ARM platform using an OpenCV matrix library. The EKF is written as a function that reads in the next measurements from the camera and the IMU as inputs. It then goes through the a priori and a posteriori states of the EKF using the new measurements. The EKF sets the state vector and covariance matrix as global variables allowing them to be used for the next iteration of the EKF. The EKF function will then output the state vector of the system. The position data from the state vector will then be sent over to the XBee, which transmits the position of the system to the base station.

To get the design running on the ARM platform the correct library is needed and the cross compiler needs to be set up. The EKF function uses matrices to store data and does matrix manipulations to calculate better approximations of the system. To do these calculations a matrix library is needed. Finding the correct library did pose a challenge. The first library used was called Meschach. The documentation for the library created the illusion that it would be of use. However, when doing initial testing some of the functions did not work properly. The functions that were being used to set the values of the elements were not correctly inputting the data. The functions that would manipulate the data also were not performing the calculations correctly. The outputted data would not be correct. After looking through the library and seeing how the functions were written, it was apparent that the functions were not written properly. Instead of rewriting these functions and a different library was used. OpenCV had a matrix library where the functions were written properly. After doing some basic manipulations of matrices using the functions from OpenCV it was apparent that the functions were performing correctly. Once a working matrix library was found the EKF was then written in C++ and tested on an x86 platform.

Once the EKF was proven to work on an x86 platform, the next challenge was to get it to cross compile onto the ARM platform. The compiler that was used is called arm-linux-gnueabihf-g++. The challenge was getting the matrix library to compile and link correctly. When building the matrix library only a portion of the library would build and link. However, the part of the library that is being used by the EKF was built and linked. The problem was that the compiler couldn't find the library. Changing where the compiler was looking for the library was tried first but it did not work. Next, the library was rebuilt and relinked to try to connect the library to the directory where the compiler was looking. The compiler still couldn't find it. Finally, the library was built and linked in its own directory and then copied over to the directory where the compiler was looking. This finally worked and the EKF does compile for the ARM platform.

IV.III.I Design Changes

The first step of the Kalman filter is the transformation of the measurements of the visual odometry subsystem and IMU sensor from the systems body frame of reference to the global frame. This transformation relies heavily on the accuracy of the heading estimations and measurements. Because we were not able to completely remove the bias introduced by changes in acceleration within the IMU, we were not able to fully implement local-to-global transformation. To adjust for this, we found that if the system was kept relatively flat during testing, the angles of roll and pitch could be set to zero. This effectively equates to the local yaw of the system being the same as the global yaw.

Because of the complications in removing the gyroscopes drift, we were unable to implement the entire Kalman filter that was described before. Without accurate calculations of the roll and pitch of the system, acceleration measurement became useless due to the components of gravity present in each axis. Because the roll and pitch had to be set to zero, the systems capabilities were very limited. Any slight change in pitch or roll resulted in inaccurate data being recorded.

IV.III.II Extended Kalman Filter Process

Figure IV.IX below shows the overall flow chart of the different steps that the EKF takes to produce the filtered output state. The EKF first takes in the data from the camera and the IMU. The constants and all of the variables that the EKF will need, such as the state and measurement vectors, are initialized next. The EKF then enters the *a priori* state were the EKF will predict the next state of the system as well as predict the next covariance matrix. It then checks to see if there is any new camera data. If there is not, then the EKF will only transform the IMU measurements into the global frame. If there is camera data, then both the camera and IMU data is transformed into the global frame. After the data is transform, the measurement vector is updated. Next the EKF enters the *a posteriori* state. This state will calculate the Kalman Gain and adjust the state vector based on the new measurements. The covariance matrix will also be adjusted. The position and heading state of the system will then be outputted to the XBee to be transmitted. The EKF only runs when it receives new data from the IMU and/or the camera.

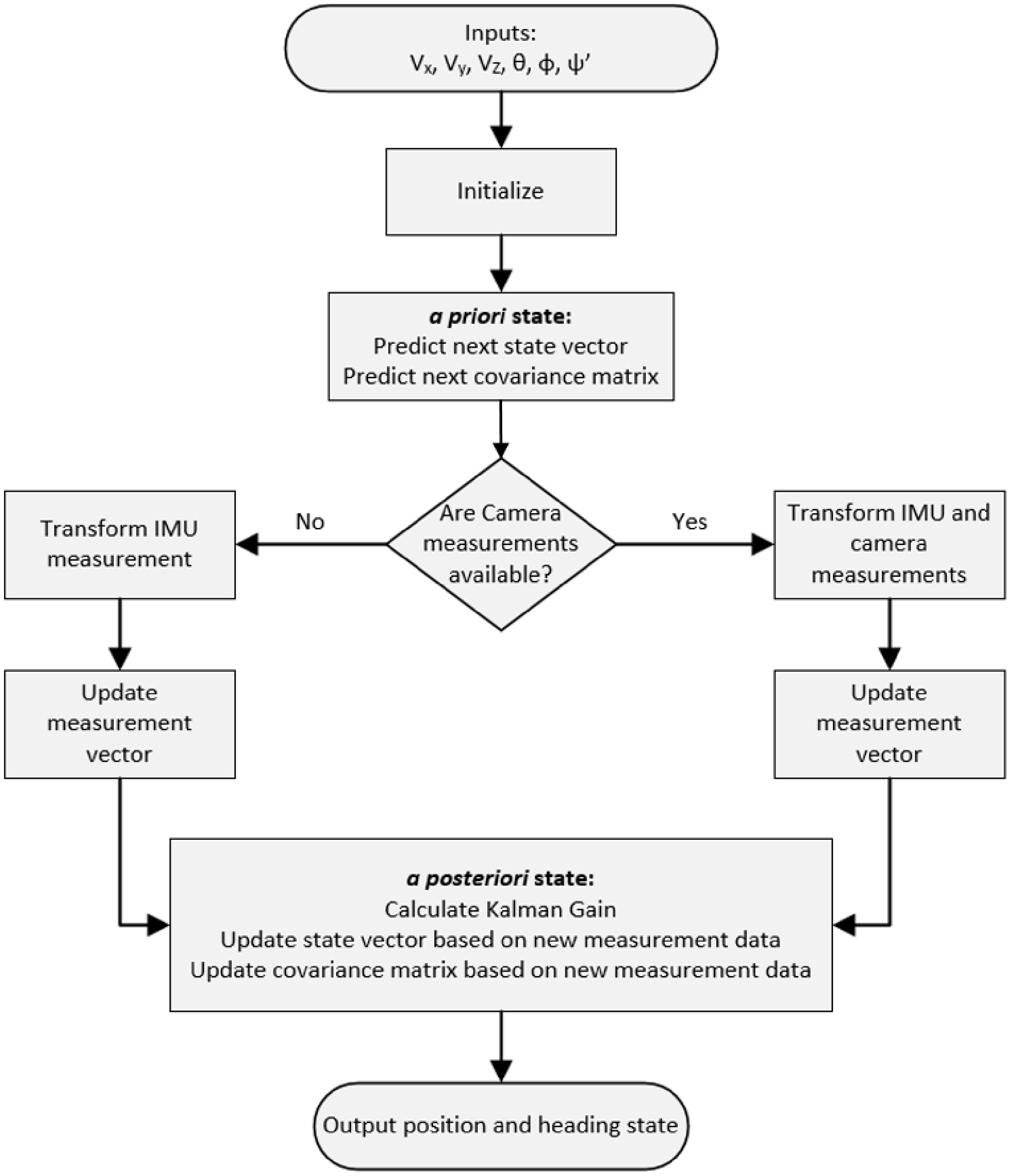
Inputs:
V_x, V_y, V_Z, θ, ϕ, ψ'
Initialize
a priori state:
Predict next state vector
Predict next covariance matrix
Are Camera measurements available?
No
Yes
Transform IMU measurement
Transform IMU and camera measurements
Update measurement vector
Update measurement vector
a posteriori state:
Calculate Kalman Gain
Update state vector based on new measurement data
Update covariance matrix based on new measurement data
Output position and heading state

Figure IV.IX: Extended Kalman Filter flow chart

IV.IV XBee Radio Communication

XBee Pro radios were chosen due to their simplicity and the extensive documentation on their usage. In order to set up the XBees for peer-to-peer communication, the two were accessed through *minicom*, a serial communication program. The serial communication baud rate was set to 57600 baud with 8 data bits, no parity, and a stop bit of 1. The maximum baud rate of 115200 baud was incompatible with MATLAB's serial communication library. Next the Xbees were controlled to enter configuration mode by typing "+++" and waiting for the response "OK". Within the command mode, AT commands can be sent to the XBees to either read or set the configuration parameters. The most important parameters are the Channel, PAN ID, and Interface Data Rate. These three values were set to C, 3332, and 57600 respectfully by utilizing the Command Reference Table in the XBee Product Manual.

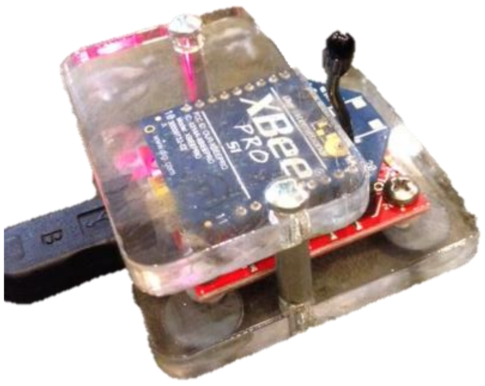

Figure IV.X: XBee Radio and USB Interface

In transparent mode, the XBees buffer the incoming serial data and sends the packet after either 100 characters are received, the command mode sequences is received, or after no characters are received for a time period equal to the packetization timeout. For our project we only have one XBee transmitting and one receiving which allows us to send data whenever we want without the danger of interference caused by both transceivers transmitting at the same time. We chose a packetization timeout of 3 character such that data was transmitted after an entire frame was communicated to the transmitter on the mobile system. Because of the comma delimited data format, the combined number of digits and decimal points of the six measurements must be less than or equal to 89. These configurations are then saved to non-volatile memory with the AT command "WR".

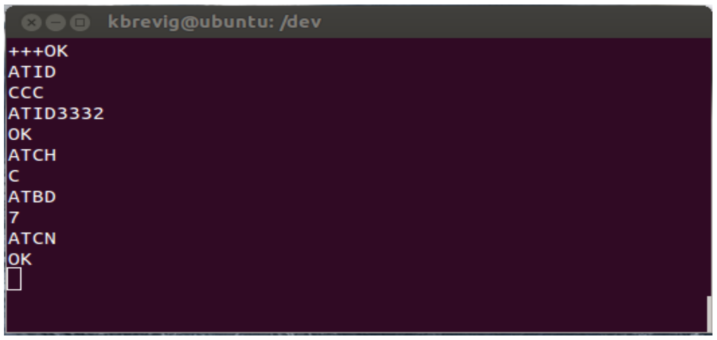

```
kbrevig@ubuntu: /dev
+++OK
ATID
CCC
ATID3332
OK
ATCH
C
ATBD
7
ATCN
OK
```

Figure IV.XI: Configuring the XBee Channel and PAN ID

IV.IV.I MATLAB GUI

A MATLAB script was created to connect to an XBee radio over serial communication, read in incoming data, and plot the system position and orientation over time. Three plots are displayed including a top down view of the systems past and current x and z-coordinates, the systems height over time, and the three axes of revolution over time. The following plot is the result of sending hand typed packets to one XBee radio through *minicom* connection, receiving the packets on the other XBee, and processing the packets in MATLAB. In this experiment, two packets were alternated to prove the concept.

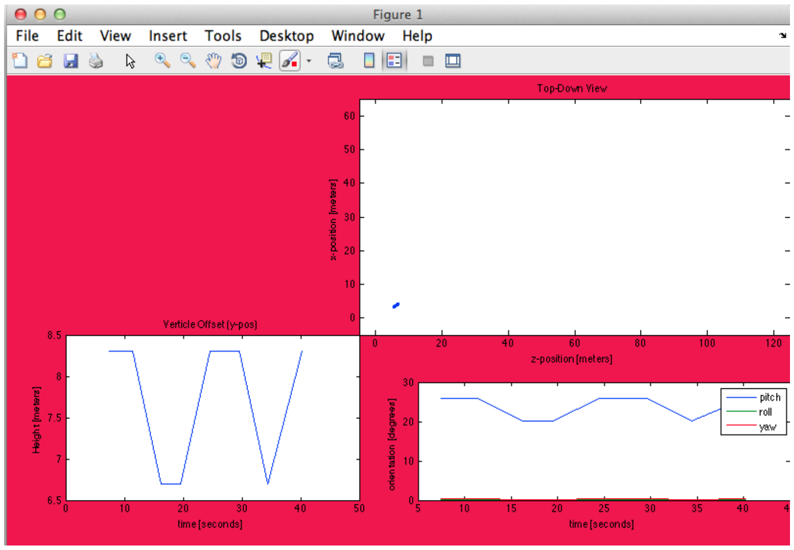

Figure IV.XII: MATLAB Receive and Plot

IV.V OMAP5432 EVM Processor

The main processor was used for visual odometry processing, interpretation of the data received from the IMU and data fusion using an EKF. As the team was not planning on developing an entire circuit board for the processor, the chosen device had Selection of the processor and supporting board was made by weighing several factors, with price and ease-of-use as the leading influences. One of the first major decisions about the processor that needed to be made was the architecture that would be used.

Early tests were run on x86 processors. The x86 architecture is a 32-bit microprocessor architecture named for the line of microprocessors from Intel, is an architecture that is ubiquitous in personal computers produced solely by Intel and its spin-off AMD. The x86 architecture has evolved over the years to become a very powerful general purpose architecture, with deep pipelining and effective instructions. However as most personal computers have easy access to a wall outlet or other power supply, these processors have very large power requirements. Even x86 processors built for mobile applications such as laptops still have very large power requirements when compared to other architectures, such as PowerPC or ARM processors. As a result of requiring so much power to run, they also dissipate a large amount of power as heat. This requires heat sinks and fans to prevent the processor from overheating. For these two reasons, x86 processors are not frequently used in embedded or small mobile systems and the team determined that this would not have been an optimal choice.

The ARM architecture has become very popular in mobile devices such as tablets and cellular phones due to its low power requirements and good performance. However because ARM processors are designed to use very little power, their instructions are not as powerful as those on an x86 processor. The group chose to use an ARM processor due to the low power and cooling requirements, low cost, and ease of acquisition. Additionally, the team had some experience with ARM processors and there was a large amount of information available online for the architecture. The Texas Instruments OMAP5432 evaluation module was chosen as for the processor system. This board was released just before the beginning of the project, making it one of the newest ARM processors available for purchase. Additionally, the low price point of the board fit into the team's budget.

The OMAP5432 was supported by the OMAP5432 Evaluation Module, or EVM. This PCB included the OMAP processor, supporting voltage regulators, power control ICs, clock sources and distribution, network interfaces, RAM, connectors for the various interfaces, and other associated hardware.

A block diagram of the EVM from the board datasheet is shown in Figure IV.XIII

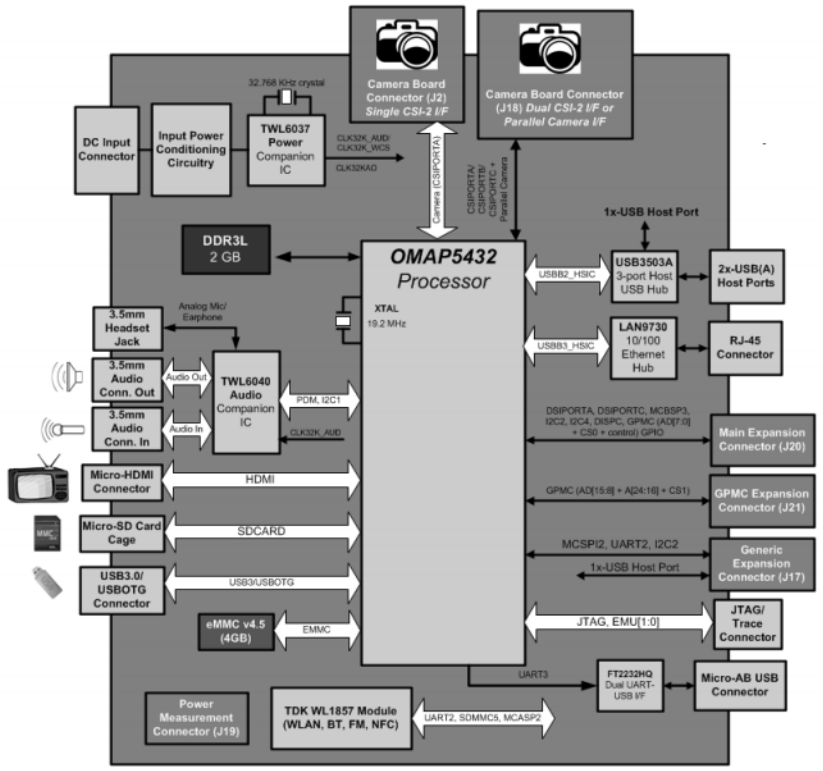
Camera Board Connector (J2) Single CSI-2 I/F
Camera Board Connector (J18) Dual CSI-2 I/F or Parallel Camera I/F
32.768 KHz crystal
DC Input Connector
Input Power Conditioning Circuitry
TWL6037 Power Companion IC
CLK32K_AUD/ CLK32K_WCS
CLK32KAO
Camera (CSIPORTA)
CSIPORTA/ CSIPORTB/ CSIPORTC + Parallel Camera
1x-USB Host Port
DDR3L 2 GB
OMAP5432 Processor
XTAL 19.2 MHz
USBB2_HSIC
USB3503A 3-port Host USB Hub
2x-USB(A) Host Ports
USBB3_HSIC
LAN9730 10/100 Ethernet Hub
RJ-45 Connector
Analog Mic/ Earphone
3.5mm Headset Jack
3.5mm Audio Conn. Out
Audio Out
3.5mm Audio Conn. In
Audio In
TWL6040 Audio Companion IC
PDM, I2C1
CLK32K_AUD
DSIPORTA, DSIPORTC, MCBSP3, I2C2, I2C4, DISPC, GPMC (AD[7:0] + CS0 + control) GPIO
Main Expansion Connector (J20)
Micro-HDMI Connector
HDMI
GPMC (AD[15:8] + A[24:16] + CS1)
GPMC Expansion Connector (J21)
Micro-SD Card Cage
SDCARD
MCSPI2, UART2, I2C2
1x-USB Host Port
Generic Expansion Connector (J17)
USB3.0/ USBOTG Connector
USB3/USBOTG
eMMC v4.5 (4GB)
EMMC
JTAG, EMU[1:0]
JTAG/ Trace Connector
UART3
FT2232HQ Dual UART-USB I/F
Micro-AB USB Connector
Power Measurement Connector (J19)
TDK WL1857 Module (WLAN, BT, FM, NFC)
UART2, SDMMC5, MCASP2

Figure IV.XIII: OMAP5432 EVM block diagram

IV.V.I Specifications

The OMAP5432 on the EVM is a dual core ARM processor, featuring two ARM Cortex-A15 processors, clocked at up to 1.5 GHz. The board includes two gigabytes of DDR3L memory clocked at 800 MHz. For non-volatile memory, the board has a 4 GB EMMC device; however the team was not able to install drivers for this device. The board has jumpers to select the boot source, and for simplicity the team made use of the micro-SD card port as the location of the operating system as well as the file system. The EVM has on-board voltage regulation and management, and accepts a wide range of input voltages, making for simple system integration.

IV.V.II Ubuntu 6.x Operating System

Texas Instruments provided two operating system choices: Yocto, a platform that provides Linux builds for specific embedded devices, and the more well know Ubuntu. As the Yocto system had limited support and documentation, Ubuntu 12.04 LTS was chosen. Additionally, several team members had previous experience with Ubuntu.

USB Flash Drive Storage

Due to the limited amount of storage on the micro-SD card, the team searched for another method to store the recorded image data from the cameras. A USB flash drive was proposed as a simple and cost effective system. This allowed easy transfers of data off the device for testing and validation, and allowed an easily expandable amount of exterior memory. For this purpose, a 64 GB flash drive with a small physical footprint was acquired. It was connected directly to one of the USB 2.0 ports on the EVM, to avoid any latency in the USB hub that was used to connect the FTDI devices.

FTDI Drivers and Serial Com Port Communication

Several devices required serial connectivity with the OMAP processor. These were the Arduino, which relayed information from the IMU, the Capella camera, which needed instructions over a serial port to start recording and transferring data, and the XBee, which received data over a serial port to transmit to the base computer. The standard Ubuntu kernel includes drivers for FTDI devices; however the kernel provided by TI for the OMAP5432 was not built with this driver included. The team rebuilt the Linux kernel to include the FTDI driver.

IV.V.III Feature Matching and Detection on ARM Platform

The library used for visual odometry, Libviso2, was written to run on x86 processors, and took advantage of several features specific to the x86 architecture. Running the visual odometry code on the ARM platform required a successful port of Libviso2 to ARM. In order to run these sections of code on an ARM platform, the sections of code containing these x86 sections had to be converted to the ARM equivalents. This process was complex and time consuming, however it was successfully completed and the section of the library that contained these features functioned exactly the same on the two platforms.

Although the code was all ported successfully, there were additional compiler issues that prevented floating point functions from running on the platform. These issues are discussed further in the Results Chapter.

Despite the failure of floating point functions, the team was able to get reliable estimations of the execution speed of the algorithm on the OMAP processor. Using these, an estimation of the performance of the OMAP platform could be made using a handicapped x86 machine. Frames were processed in approximately 400 milliseconds, a five-fold increase in execution time over the same code executed at full speed on the x86 laptop used for testing. This would result in a frame rate of approximately 2.5 frames per second on the OMAP platform. The original testing operated at 10 FPS. The frame is directly tied to accuracy. A comparison of the first floor dataset processed on an x86 processor using 5 frames per second and 2.5 frames per second is shown below.

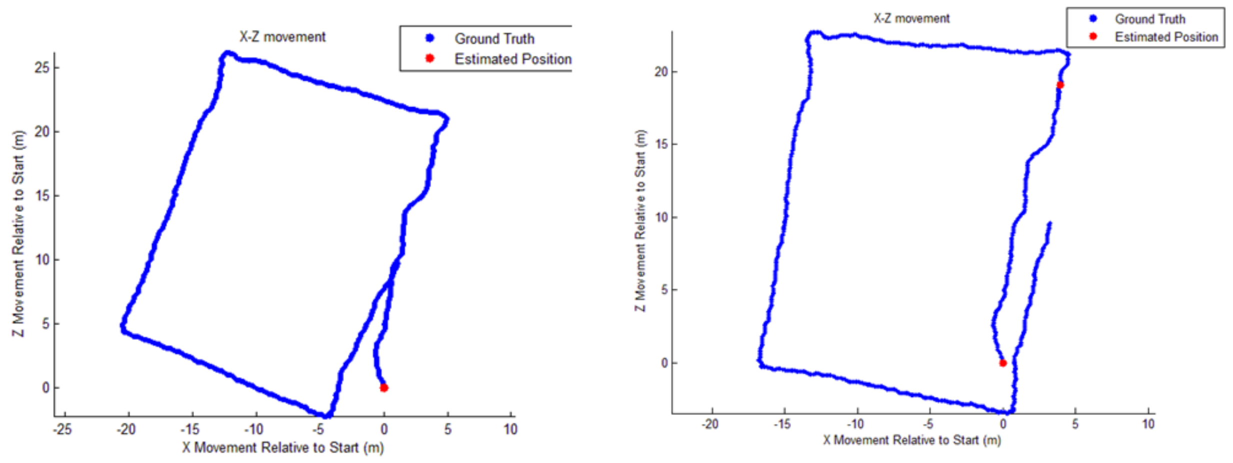

Figure IV.XIV - Comparison of visual odometry running at 5 FPS (left) and 2.5 FPS (right)

The 2.5 FPS data is less accurate; however it would still be acceptable for a proof of concept design.

IV.VI Power Management System

Successful power management is essential for effective operation of all of the system components. There were two power sources used during the debugging and testing of the system; the battery was used for mobile operation and a 12 V wall power supply was used for bench testing.

The original power usage estimations were relatively accurate. With an input voltage of 12 V the systems draws approximately 1.6 A under full processing load. The current draw varies under processing load, as both the camera processer and the main processer change their clock rates based on the load they are under. Additionally, because several of the voltage regulators used are switching regulators, the current required changes based on the input voltage as well.

Chapter V. Experimental Results

This chapter provides an overview of the testing and experimental results of the system. The performances of the various algorithms were first tested independently as they were implemented. The performance of the system was tested as a whole upon finishing the integration of the various components.

V.I Initial Feature Detection and Matching Results

The following are the initial results from the Feature Detection and Matching Algorithms implemented on an x86 processor. The Bumblee3 camera was used for obtaining the image frames (the Capella camera had not yet been purchased at this time). A data set was obtained from the first floor of the Atwater Kent building. This data set was then processed. Figure V.I presents the visual odometry approximation of the path traversed by the system on the first floor. The results are fairly accurate for this application, however the errors become more pronounced as the system keeps moving.

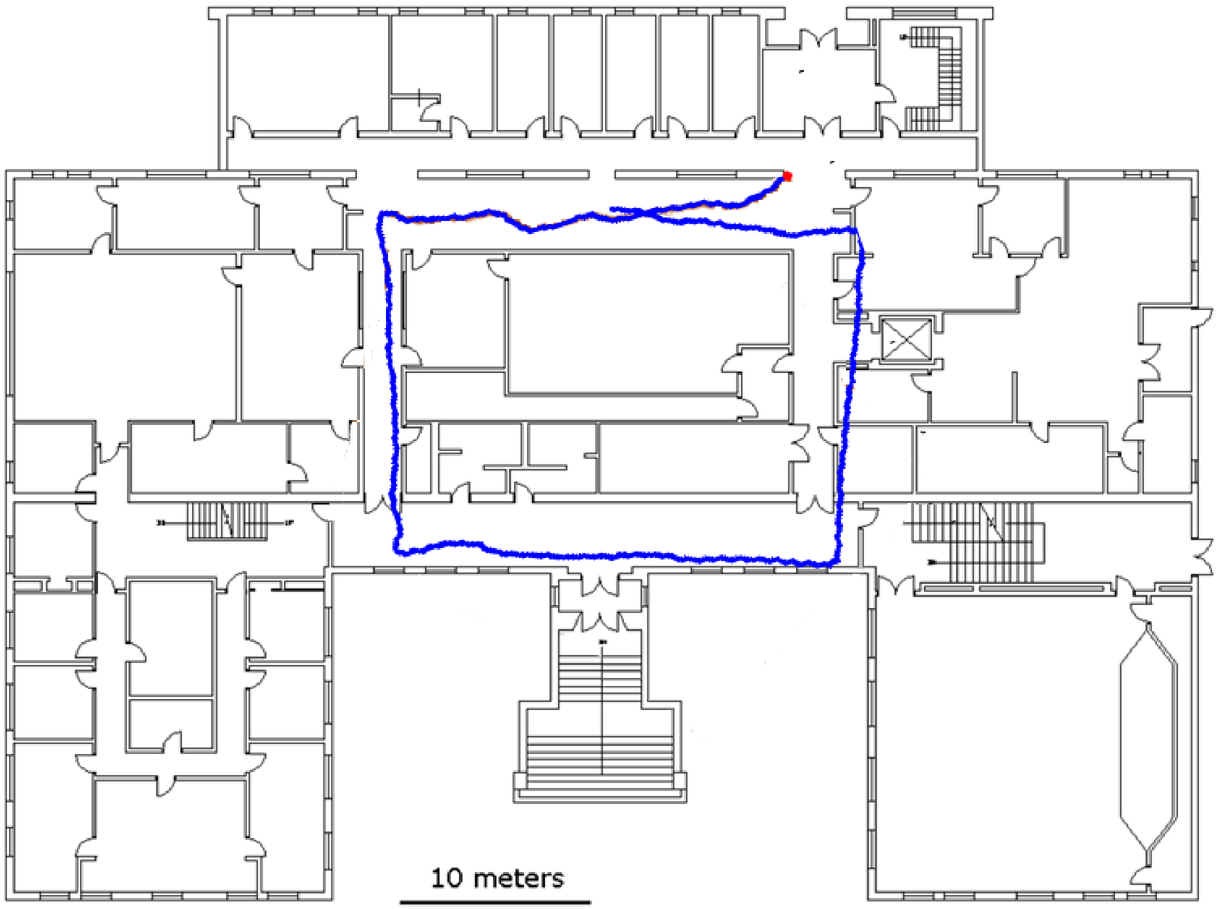

Figure V.I: Visual Odometry results on first floor of Atwater Kent, running on an x86 processor

A second dataset was taken on the third floor of Atwater Kent. This data demonstrated one of the major flaws of a vision-based odometry system. The third floor is on average more featureless and dimly light than the first floor. As such, the detector was finding less than 25% of the number of features compared to the first floor. As such, major miscalculations started to propagate upon major corner turns of the system, until the resulting path became completely erroneous. Figure V.II provides the results of the third floor dataset. Red dot mark frames where no motion reconstruction was possible due to a lack of successfully matched features.

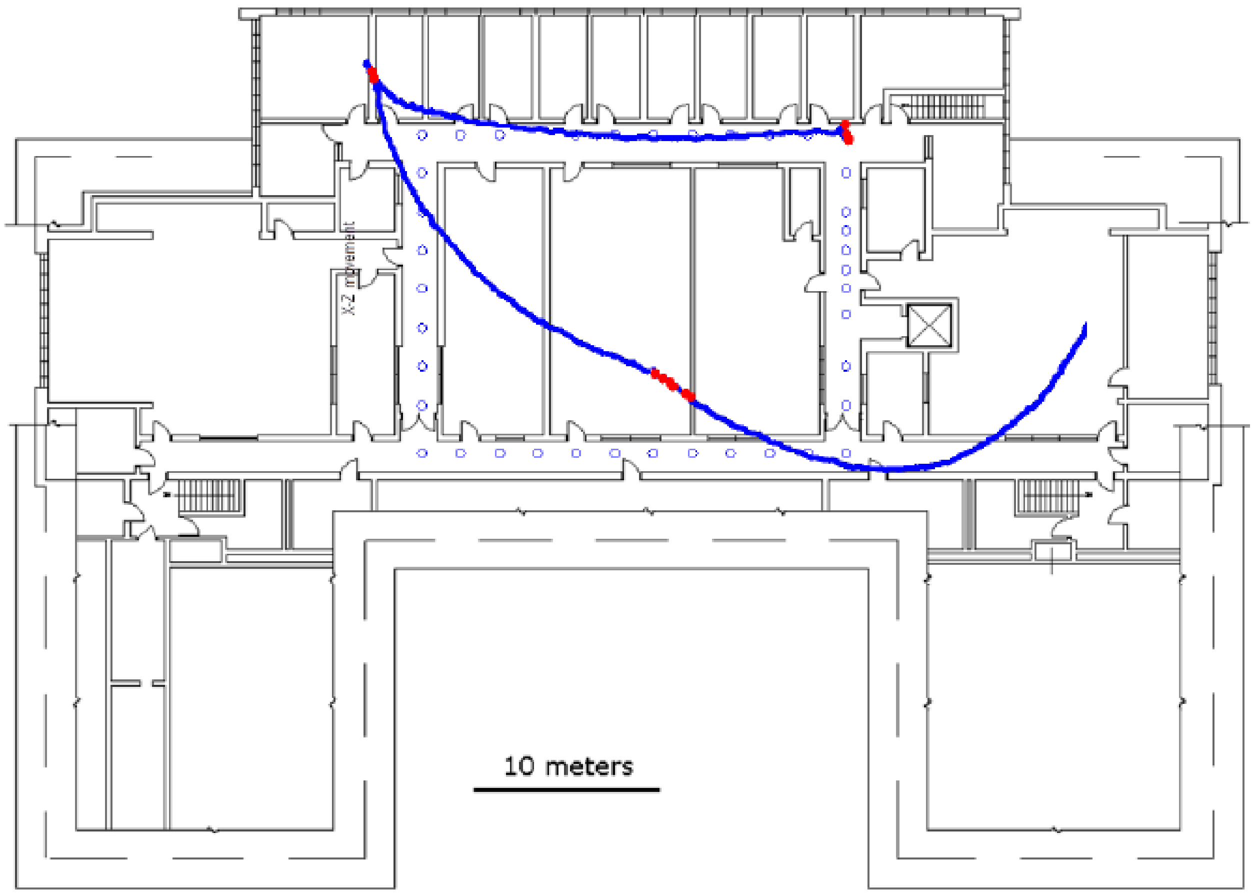

Figure V.II: Third floor results of visual odometry running on x86 processor

V.II Investigating Inertial Odometry

Because of problems with the visual odometry portion of the system, a purely inertial odometry system was extensively researched to assess its effectiveness with the hardware we had available to us. IMU readings were taken at a sample rate of 100 Hz using the Arduino Uno and a computer running a python script for serial data recording. The measured data was processed using the Kalman filter described above. Of the 12 inputs described in the measurement vector of **Figure III.X**, only linear acceleration and angular velocity are supplied as inputs to the filter from the IMU. With data from only two sensors, the gyroscope and accelerometer, it becomes much more difficult to track position and orientation.

V.II.I Gyroscope Drift

The gyroscope measurements include a bias in each angular velocity measurement, as depicted in Figure IV.VI. This leads to large drifts of the orientation when performing integration of the angular velocity. To remove bias, we first initialize the system by calculating the average angular velocity for each gyro output while the system is still on a flat surface. These values are often small, between 0.07 and 0.13 degrees/sec but add a significant drift over long period of time. In our experiments where the system remains still on a table for just over a minute, the orientation drifts as much as 8°. By subtracting the calculated average value of each output of the gyroscope, the bias can be significantly reduced resulting in a drift no more than 0.4°. The experiment results plotted in Figure V.III experienced drifts between 92% and 98% smaller then unprocessed direct gyroscopic data.

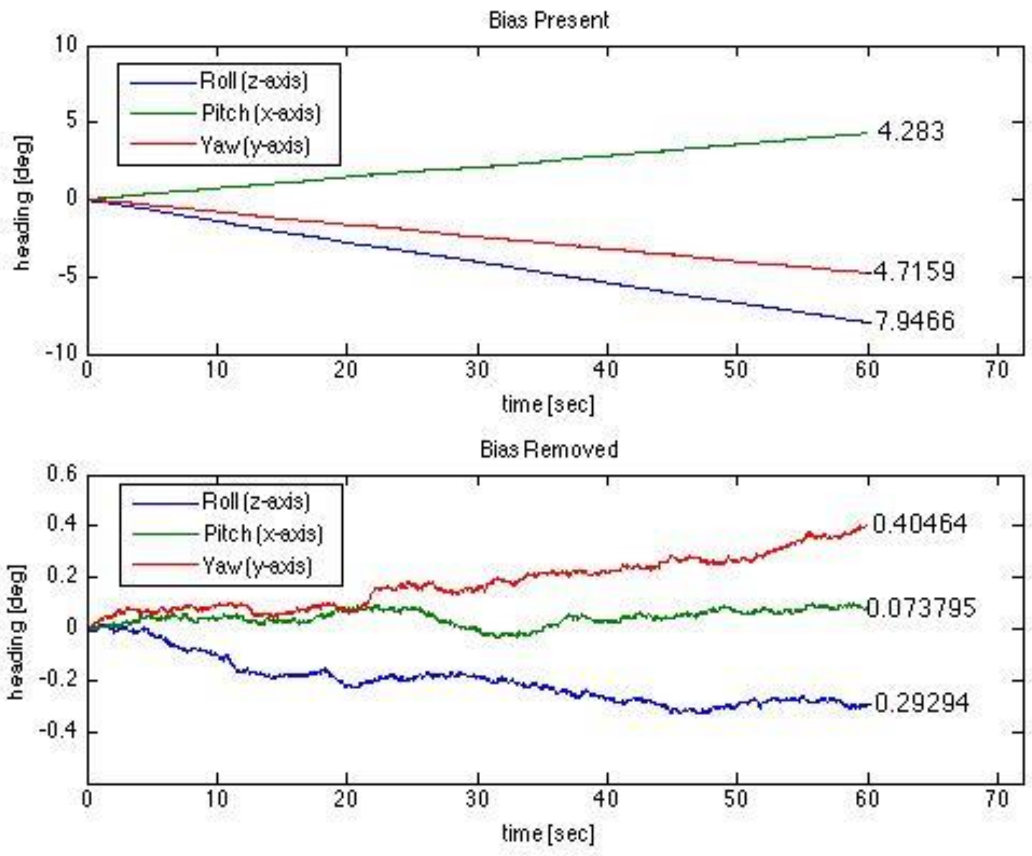

Figure V.III: Bias Removal-Sitting Still

This method of calculating the bias during an initialization script is effective for data captures over a few minutes in temperature-stable environments. If the internal temperature of the IMU changes due to extended use or varying environment temperatures, we can expect the drift to change. Over a 3.5 minute experiment in which the system was walked around the first floor of the Atwater Kent Building, the roll and pitch was tracked. As before we first initialized the system and calculated the bias. The three following plots of Figure V.IV show the 90° turns of the system in the building, the pitch and yaw after removing the bias, and the pitch and yaw as a result of running the Kalman Filter. During the first 60 seconds there is almost no drift, looking at the second plot; however drift is introduced as soon as the system is moved at approximately 80 seconds after the beginning of the measurement. Because of the translation from the local frame to the global frame in the Kalman filter, the bias of roll is a positive value when yaw is between 0° and 180° and a negative value when it is between 180° and 360°. The resulting roll at the end of testing will be close to 0° if the system spends relatively equal amounts of time facing in the positive-z and negative-z directions. These drifts were a direct result of random accelerations introduced by picking up the system and walking forward.

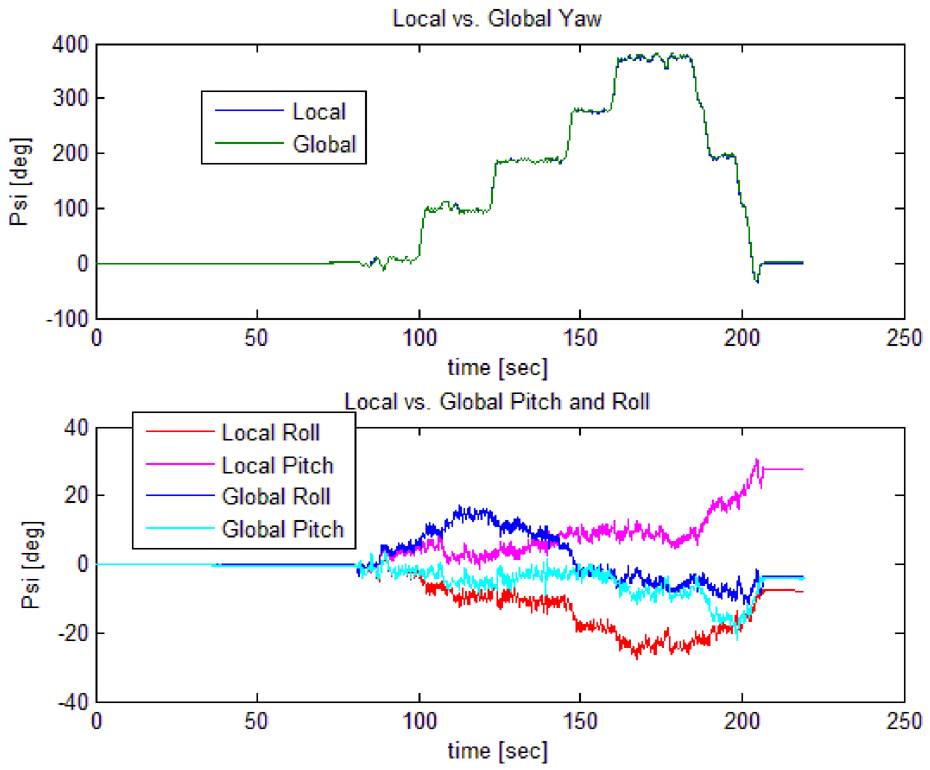

Figure V.IV: Bias Removal-90° Turns

V.III Data Fusion with EKF Results

The EKF was chosen to filter the data because it would allow the fusing of the data from the camera and the IMU. In our implementation, the EKF receives velocity measurements from the camera and it receives change in heading measurements from the IMU. The EKF fuses these measurements and calculate position. It also removes noise from the system. The EKF combines the data from the camera and the IMU through the transformation of the camera data from local to global coordinates. The transformation and fusing of the data was difficult to do. Due to the complexity, the system does not correctly fuse and transform the data.

V.III.I Understanding Noise in EKF

The EKF takes noise into account in its state estimations. As described in the subsection Noise and Data Weighting of the Non-Linear Kalman Filter Approximation section, the noise is represented in the Q and R matrices and the values are found using the process described in that section. A MATLAB script was written to find the values for the Q and R matrices using that process. The data that was used in this experiment was from the first floor of Atwater Kent. The IMU and camera were first set on a table to keep the values at a mean of zero. The standard deviations were taken of the velocity and change in angular velocity inputs from the IMU and camera. These standard deviations were then squared and placed into the diagonal of the R matrix as shown in Figure V.V. These values are also used for the velocity and change in angular velocity noise elements of the Q matrix, which are along the diagonal. The position noise element in the Q matrix is set to be the velocity noise element multiplied by the change in time. The angular velocity noise element in the Q matrix is set to be the change in angular velocity multiplied by the same change in time. The Q matrix is shown in Figure V.VI. These values are used in our EKF to best represent the noise of the system.

$$\begin{bmatrix} 7.0633e-4 & 0 & 0 & 0 & 0 & 0 \\ 0 & 8.7067e-4 & 0 & 0 & 0 & 0 \\ 0 & 0 & 8.9663e-4 & 0 & 0 & 0 \\ 0 & 0 & 0 & 2.8716e-6 & 0 & 0 \\ 0 & 0 & 0 & 0 & 5.7418e-6 & 0 \\ 0 & 0 & 0 & 0 & 0 & 4.5105e-6 \end{bmatrix}$$

Figure V.V: Values of R Matrix

$$\begin{bmatrix} 3.5317e-6 & 0 & 0 & 0 & 0 & 0 & 0 & 0 & 0 & 0 & 0 & 0 \\ 0 & 4.3533e-6 & 0 & 0 & 0 & 0 & 0 & 0 & 0 & 0 & 0 & 0 \\ 0 & 0 & 4.4832e-6 & 0 & 0 & 0 & 0 & 0 & 0 & 0 & 0 & 0 \\ 0 & 0 & 0 & 7.0633e-4 & 0 & 0 & 0 & 0 & 0 & 0 & 0 & 0 \\ 0 & 0 & 0 & 0 & 8.7067e-4 & 0 & 0 & 0 & 0 & 0 & 0 & 0 \\ 0 & 0 & 0 & 0 & 0 & 8.9663e-4 & 0 & 0 & 0 & 0 & 0 & 0 \\ 0 & 0 & 0 & 0 & 0 & 0 & 1.4358e-8 & 0 & 0 & 0 & 0 & 0 \\ 0 & 0 & 0 & 0 & 0 & 0 & 0 & 2.8709e-8 & 0 & 0 & 0 & 0 \\ 0 & 0 & 0 & 0 & 0 & 0 & 0 & 0 & 2.2553e-8 & 0 & 0 & 0 \\ 0 & 0 & 0 & 0 & 0 & 0 & 0 & 0 & 0 & 2.8716e-6 & 0 & 0 \\ 0 & 0 & 0 & 0 & 0 & 0 & 0 & 0 & 0 & 0 & 5.7418e-6 & 0 \\ 0 & 0 & 0 & 0 & 0 & 0 & 0 & 0 & 0 & 0 & 0 & 4.5105e-6 \end{bmatrix}$$

Figure V.VI: Values of Q Matrix

V.III.II Sensor Fusion

Experiments with sensor fusion within the EKF provided mixed results. In some cases, adding the IMU's tracking of heading to the data from the visual odometry subsystem created worse results as evident in the first floor capture displayed in Figure V.VII. Here we see that the visual odometry better tracked heading, completing more precise turns. When the visual odometry heading was replaced by the heading calculated from the IMU, turns became much noisier and less precise.

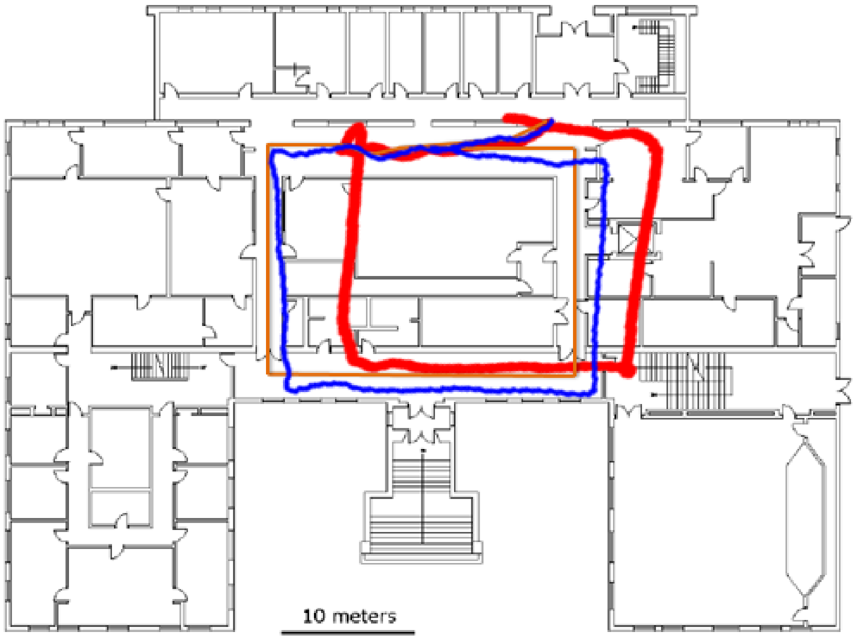

Figure V.VII: Results of sensor fusion on first floor of Atwater Kent (Blue – raw data, Red – Sensor Fusion, Orange – Ground truth)

A data capture on the third floor of Atwater Kent that failed when implementing visual odometry was improved by fusing the heading from the IMU. This data set had failed due to the lack of edges for tracking and sufficient lighting. The linear movement was inaccurate, which is evident when the system passes the hallway before the first turn. Although this data set doesn't show a reliable localization of the system, we are still able to show that sensor fusion can provide improvements in some cases.

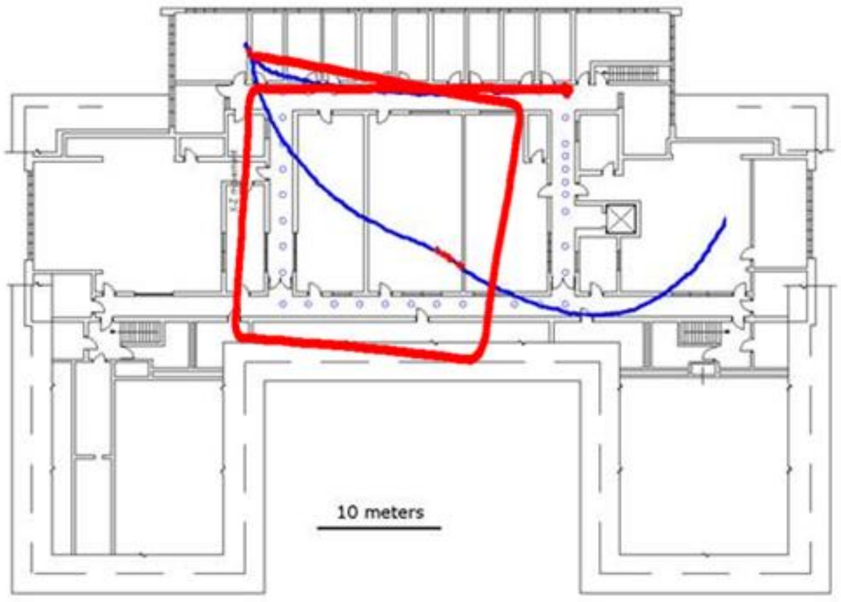

Figure V.VIII: Results of sensor fusion on third floor of Atwater Kent (Blue – raw data, Red – Sensor Fusion, Circles – Ground truth)

V.IV XBee Transmission and Data Representation

Despite not achieving full integration of the visual and inertial odometry in real time, we were still able to experiment with data transmission and visualization with an external GUI. Position data from the visual odometry experiments and heading data from the inertial odometry were sent by wireless transmission to a computer. A MATLAB program on this computer displays this information in real-time in a GUI to show height, heading, and a top-down view of the z and x positions. Because the data must be re-plotted each time, the execution time of the GUI was expected to increase as more and more data was received. Instead, we found that this was untrue and that the execution time stayed under 0.1 seconds as shown in Figure V.X. If this maximum execution time happens to be slower than the update rate of the system, data frames may be missed. This is not a huge concern considering all the position and heading values aren't necessary to the general user.

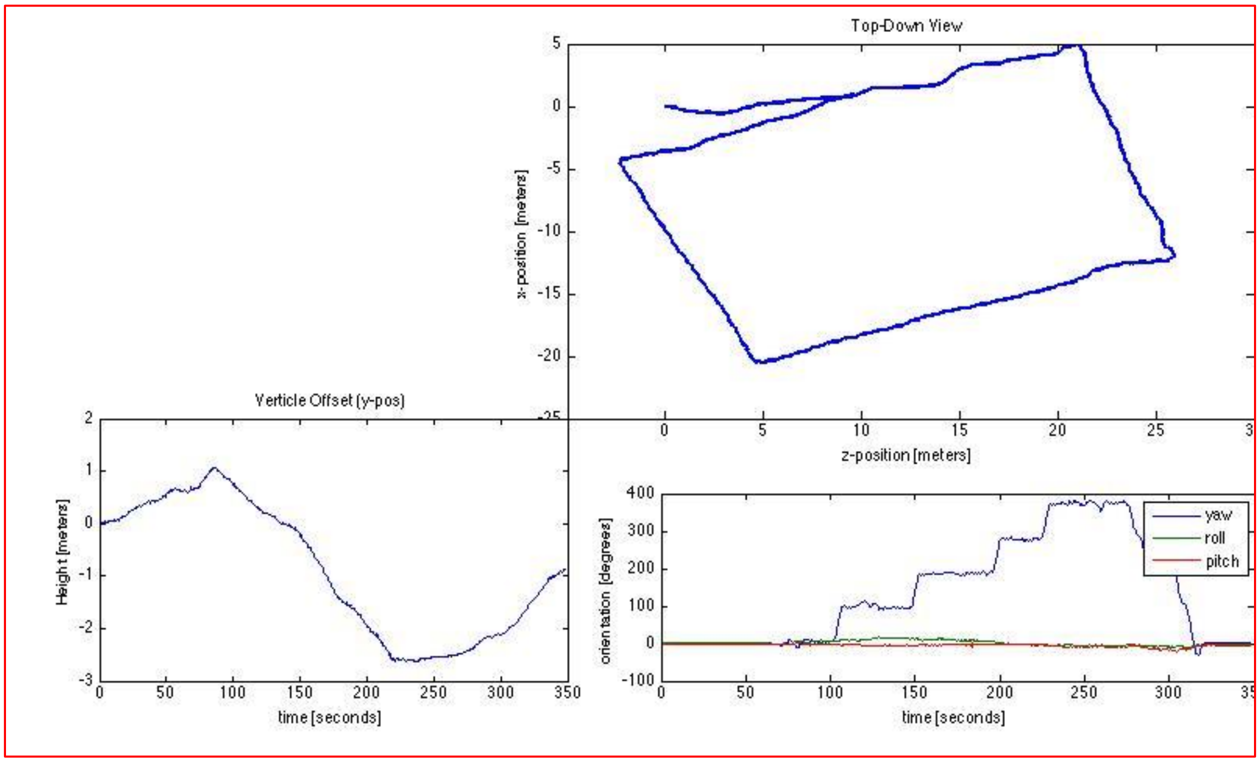

Figure V.IX: Real-time position and heading GUI

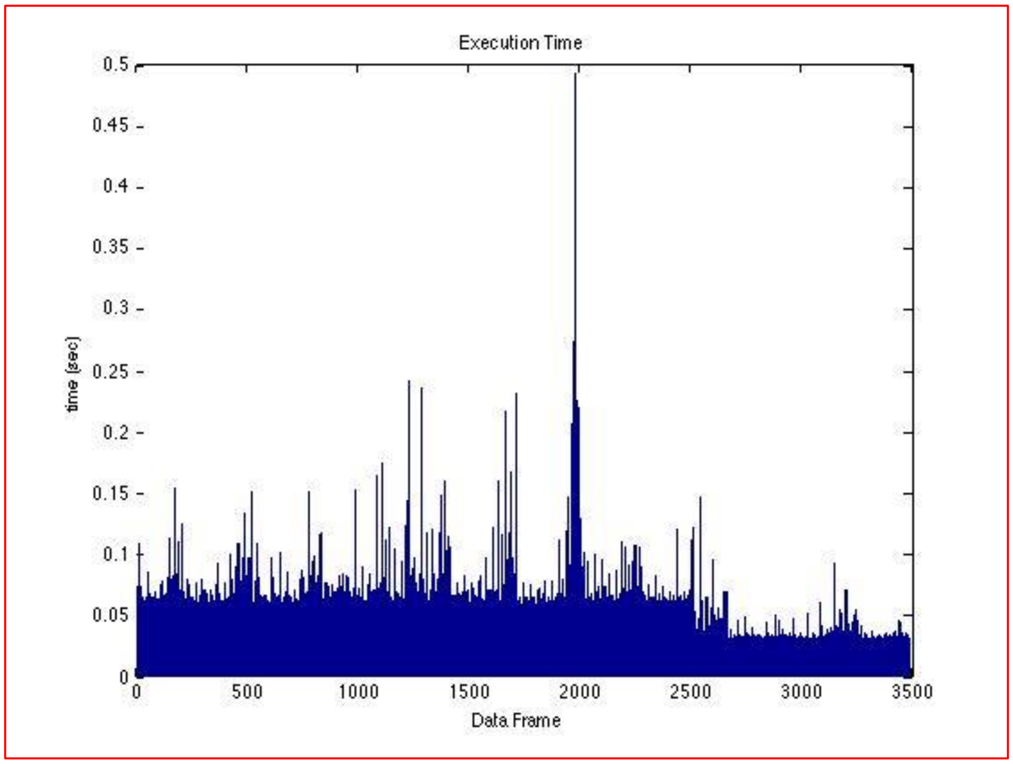

Figure V.X: GUI Execution Time

Chapter VI. Conclusions

This project proposed a real-time indoor navigation system using visual and inertial odometry. Many of the design requirements were met; however the real-time aspect of the design was compromised due to the integration challenges posed by the hardware chosen for the implementation. A summary of the project goals, their current status, and their implementation is given by Table VI.I.

Table VI.I: Design Goals and implementation status

Project Goal	Implementation	Status
Visual Odometry		3/4
• **Capture images and stream them in real-time**	Capella Stereovision Camera used to capture image pairs. GStreamer framework used to stream image frames over an Ethernet connection.	Met
• **Feature Detection and Matching**	Blob and Sobel filters were used to find image features, and feature descriptors, respectively. Circular Matching was used to locate similar features between pairs.	Met
• **Motion Reconstruction**	RANSAC used to reconstruct camera motion from successful feature matches.	Met
• **Successful ARM Port**	X86 version of C++ code cross-compiled for ARM. Intrinsic functions manually altered to closest corresponding ARM counterpart. Compiler floating point errors not resolved.	Not Met
Inertial Odometry		3/4
• **Obtain Acceleration and Rotation Data.**	ADIS16375 IMU used to obtain data. Level shifter designed to resolve high-bit voltage differences.	Met
• **Integrate Data to find position**	Kalman Filter performs a summation of motion data for each time step in order to estimate position	Met
• **Successful incorporation with ARM processor**	The IMU data is sent to an Arduino Uno via a SPI interface. The Arduino parses the data to the ARM processor through a vitual COM port.	Met
• **Bias Removal**	Static bias was removed, as well as drift caused by temperature changes. Bias caused by unpredictable acceleration changes is still persistent.	Not Met
Sensor Fusion		3/4
• **Design of EKF**	Extended Kalman filter designed on Matlab.	Met
• **C++ port of EKF**	Matlab version of EKF manually converted to C++ to increase code execution efficacy.	Met
• **ARM port of C++EKF**	C++ code was cross compiled for ARM platform. Floating point errors from compiler not resolved.	Not Met
Cost-Effective	Total price of system was under $3500, due to relatively inexpensive parts chosen.	Met

Real-Time		2/3
• Visual Odometry	Software executes with each new image input from Capella camera, at ~3 FPS. Software not working as intended on mobile platform due to compiler floating point errors.	Not Met
• Inertial Odometry	Raw acceleration and rotation data was extracted, transformed and sent to the processor at each time step.	Met
• Data Transmission	Extracted coordinates from each time step transmitted wirelessly through radio transceiver, and mapped at base station.	Met
Indoor Navigation by motion reconstruction	Motion reconstruction obtained in visual odometry by RANSAC. This data when fused with rotational data from inertial odometry successfully reconstructed system movement in building.	Met

The initial results of the visual and inertial localizations were promising. The feature detection and matching algorithm was able to successfully localize a moving camera system within Atwater Kent. Similar results were obtained from inertial data. Significant strides were made in developing a fully functional, integrated design. A successful ARM port of the (x86) Feature matching and detection algorithms was created. Likewise, the Capella Camera, and the ADIS16375 IMU were both able to communicate with the chosen processor. An ARM C++ Kalman filter was also designed. Unfortunately, the processor chosen by the group, while very powerful, was also fairly new in the market, and lacked much of the documentation necessary for an ideal implementation. With that being said, the implementation itself met the low-cost criteria, costing less than half of some other inertial odometry designs. Indoor navigation was achieved, albeit only through post-processing of the data.

VI.I Challenges

The proposed design was not without its share of challenges to be overcome. The principle challenges mainly arose from the integration of the different components; however some implementation difficulties inherent to the components used were also prevalent.

VI.I.I ARM Architecture Port of Feature Matching and Detection Code

In preliminary testing, the Libviso2 library was found to be very effective when run on an x86 platform, such as a typical desktop computer. The team planned to implement the system on an ARM processor, so the library had to be ported between platforms. This was expected to be a straightforward process, as the library was primarily a series of math functions with few IO operations or other functions that were hardware dependent. Further investigation, however, revealed that in order to increase the efficiency of the filters and parts of the feature matcher, several parts of the code made use of x86 SIMD intrinsics [10]. SIMD, or Single Instruction Multiple Data, is a method of performing vector processing where a single instruction operates on several pieces of data that are stored in a vector format. The x86 SIMD engine can handle 64- and 128-bit variables that consist of several smaller variables arrayed inside. For example, a 128-bit SSE variable could consist of two 64-bit IEEE 754 doubles, or eight 16-bit integers. Operations can then be performed on all of the elements in the variable at once, such as adding them to the corresponding elements in another SSE variable or summing the entire array. For functions that require repeated operations, such as convolving a filter kernel with an image, the use of these functions can speed up the function several times.

The implementation of this functionality is very closely related to the precise vector processing unit used. On x86 platforms, this unit is called SSE. The authors of *Libviso2* used SSE intrinsic functions, or functions that translate directly into predefined assembly instructions. The intrinsics for SSE functions are compiled directly into x86 assembly, and as a result code containing these intrinsics is not portable to other processor architectures.

To port the library to run on the OMAP, all of the SSE intrinsics needed to be changed to the ARM SIMD instruction set, called NEON. Although both of these are SIMD instruction sets, they are implemented differently. For many of the SSE operations used there was no direct NEON equivalent. A simple example of this was a short function that took two 128-bit variables containing eight 16-bit integers and combined, or packed, them into a single 128-bit variable containing sixteen 8-bit integers. In cases where an element was larger than 8 bits, it was saturated, or set to the highest value. Using SSE instructions, this could be accomplished using a single instruction, as shown below.

```
void pack_16bit_to_8bit_saturate( const __m128i a0, const __m128i a1, __m128i& b )
{
  b = _mm_packus_epi16( a0, a1 );
}
```

However no corresponding instruction existed for NEON. Instead, a workaround had to be found. Two intermediate values are calculated; each of the 16x8 integers is first converted to an eight element 8-bit vector and is saturated in the process. These two 64-bit values are then combined into a single 128-bit value. The final function using NEON intrinsics is shown below.

```
    void pack_16bit_to_8bit_saturate( const int16x8_t a0, const int16x8_t a1,
uint8x16_t& b ) {
       b = vcombine_u8 (vqmovun_s16(a0), vqmovun_s16(a1));
    }
```

Although it is still only one line, this function now includes three function calls to interdependent data which would be difficult to pipeline, resulting in significantly reduced performance.

Each time a SSE intrinsic function was used, it had to be changed by hand to NEON instructions. Despite this, all of the SSE intrinsics were successfully converted to direct NEON equivalents or to equivalent sections of NEON intrinsics. Testing revealed that all of the changed sections of code produced exactly the same result on the two different platforms.

A more serious problem that was encountered was a difficulty compiling floating point function calls for the ARM platform. When ARM compilers were originally written, most ARM processors did not have a built in floating point unit, and as a result floating point was emulated in software. When hardware floating point units were added, the calling convention for floating point functions changed. These two formats of floating point conventions are not compatible. Due to the requirement for NEON instructions, the project required function calls to be made using the soft floating point convention, however, the group believes that the C++ Math library on the ARM platform expected floating point function calls to be made using the hardware floating point convention. As a result, calls to important cmath functions such as trigonometric functions and simple rounding functions such as ceil and float returned incorrect values, leading to failure in the visual odometry library. Unfortunately, there was not enough time to fully diagnose this problem or to determine a method to repair it. This problem was not discovered until much later in the debugging process as the large majority of the math done in the visual odometry library is integer math, which was not affected by this problem. Floating point math is done primarily in the motion reconstruction portion of the code, and as a result the problem was initially masked by the other difficulties that were encountered while porting the code to ARM, primarily the SIMD instruction problem discussed above. The team reached out to TI technical support to attempt to find a solution, however they were unable to assist with the problem.

As a result the visual odometry library was not successfully implemented on the ARM platform.

VI.I.II Lack of Serial Drivers on OMAP5432 EVM

The primary method used to connect several parts of the system, including the wireless transceiver, the IMU and the control interface for the Capella Camera was FTDI USB virtual serial ports. This consists of a driver on the USB host and a USB connected integrated circuit made by Future Technology Devices International. When the FTDI IC is connected to the USB host, it appears as a hardware serial port, similar to a RS-232 serial port that can be found on older computers. These devices are commonly used as a simple solution for connecting custom USB devices to a computer, and were used in the original Arduinos. Due to their common use, the drivers for these devices are typically built into Ubuntu, and the team planned on easy integration with the Ubuntu OS on the OMAP platform.

The build of Ubuntu provided by TI, however, did not include these drivers, most likely to save space. As a result, when the FTDI devices were connected to the OMAP they were enumerated as generic USB devices and did not work.

In order to fix this, the Linux kernel had to be rebuilt, including the FTDI drivers. The build of the kernel is controlled by a file, called a config file, which contains a list of which features from the source code to include in the kernel build. This config file also controls which devices the kernel will work on. The team had some difficulty finding the location of the config file that had been specifically written to work with the OMAP platform. Once the config file was located, it was modified to include the necessary driver, and used to rebuild the kernel, which was copied over the old kernel on the bootable SD card. The process used to achieve this is described in detail in Appendix A.

VI.I.III Streaming between Capella Camera and OMAP5432 EVM

The only video output capability provided by the Capella Stereovision Camera was an HDMI out port. Unfortunately, the OMAP5432 EVM did not have HDMI input capabilities. As such, an alternative way to stream the video to the processor had to be devised. It was quickly decided that the unused Ethernet ports on the camera and processor could be repurposed for video transmission. Originally, a simple test was performed to check whether video could be transmitted in real time over Ethernet through a local SSH network between the Capella and the OMAP5432. However, the Capella Camera operating system would refuse the set public and private keys in order to connect with OMAP. Other transmission protocols, such as UDP and TCP could neither understand nor handle the raw video obtained from the camera drivers. It was then realized that a more intricate approach would be required in order to transmit the video streams.

After more research, it was found that the GStreamer Multimedia framework allowed for the functionality described above. However the GStreamer framework had to be first cross-compiled for an ARM7 architecture (the architecture of the Capella processor) and installed unto the Capella camera. This proved to be a non-trivial task, as no members of the group had any prior experience with cross-compilation. Different methods to do this were performed; however they were met with only minimal success. Eventually, a successful compilation of GStreamer for the Capella camera was achieved by using the *Scratchbox2* cross-compiler (and even then it was after much trial and error). Once the base GStreamer functionality was ready, the GStreamer plugins were all cross-compiled and installed in a similar functionality. The installation to the Capella Camera was achieved by copying the relevant files to the necessary filesystem directory on the Camera through a pre-established FTP network. Some GStreamer plugins were incompatible with the Capella Camera, so they could not be used, but the functionality intended for this design could still be achieved. Unfortunately, there were still more issues that had to be resolved before video streaming to the processor could be achieved.

Lack of Digital Signal Processing on Capella Camera

Most of the relevant GStreamer pipelines that allowed for video streaming made use of video encoding plugins for more efficient streaming and pay loading of raw video. However, the video encoding plugins required DSP capability from the Capella Camera. Despite the camera processor being designed for DSP applications, and the Capella being advertised with DSP capabilities, the actual DSP drivers were missing on the camera. This group did not have the intimate knowledge, or time required, to implement the DSP drivers ourselves. Thus we communicated with the Capella manufacturers with the intent of obtaining the drivers. This method became unfeasible due to the company requiring considerable monetary compensation for their services. Thus we were left with having to find a workaround for the DSP issue. Ultimately, a pipeline was created that could stream the video without encoding it first (thus removing the DSP requirement). Nevertheless, this method proved to be far less efficient, and the pipeline could only maintain long-term stability at less than 10 FPS streaming. Likewise, the pipeline allocated about 97% of the Capella CPU while it was running.

Non-calibrated Image Frames from GStreamer Pipeline.

One of the main attractions of the Capella Camera was that it came pre-calibrated. However, unbeknownst to the group, the "calibration" only applied to the demo applications on the camera OS that were provided by the company. This was contrary to the groups' interpretation that the calibration was done on the camera drivers themselves. The GStreamer pipeline previously discussed extracted the video directly from the camera drivers, completely avoiding any pre-calibration performed by the Capella manufacturers. As such, the images sent to the OMAP5 processor showed signs of misalignment and the "fish-eye" effect. Unfortunately, it was too late to fix this issue by the time that it was discovered.

VI.I.IV IMU Bias

The Gyroscope has a constant static bias that was successfully removed by averaging the gyroscope output at zero angular velocity when gyroscope is sitting still on a table and subtracting the average from subsequent measurements. However, gyroscope also has a bias component that varies with time (also called drift) due to effects of linear motion. In the local frame the drift accumulates non-linearly to large values over time. But after converting from local frame to global frame, the drift may increase or decrease depending on whether the turns were in one direction (either clockwise or anti clockwise) or were a combination of clockwise and anti-clockwise turns which cancel out each other. Given the unpredictable nature of the gyroscope drift, it is difficult to filter the drift in gyroscope data.

VI.II Future Work

The primary work to be done in the future would be to resolve the remaining integration issues. Beyond that, there is much room for improvement on the design and implementation described above. Provided the time and resources, the ideal system would consist of custom made components, rather than off-the-shelf designs. Likewise, the feature detection and matching algorithms can still be optimized for ARM processors and attain a higher frame rate (alternatively, an x86 processor may be used instead, which mitigates arm compatibility issues). The Arduino parser may be replaced in future designs when the drivers for the SPI interface on the OMAP5432 are provided. The evaluation model for the processor, while ideal for rapid prototyping, is not ideal for an efficient design. As such, a future model would implement a custom PCB for the OMAP5432 processor (or any other processor that may be decided on). By changing to custom made components, much of the size of the system can also be reduced. Ideally this indoor navigation system should have a weight and size comparable to a modern cellphone or tablet, such that is does not hinder the first responder or mobile robot.

Works Cited

[1] O. Woodman, An Introduction to Inertial Navigation, Cambridge, MA: University of Cambriddge, 2005.

[2] G. Galben, ""New Three-Dimensional Velocity Motion Model and Composite Odometry–Inertial Motion Model for Local Autonomous Navigation"," *IEEE Transactions on Vehicular Technology,* vol. 60, no. 3, pp. 771-781, March 2011.

[3] D. Scaramuzza, F. Fraundorfer and R. Siegwart, "Real-Time Monocular Visual Odometry for On-Road Vehicles with 1-Point RANSAC," in *IEEE International Conference on Robotics and Automation*, Kobe, Japan, 2009.

[4] J. Campbell, R. Sukthankar, I. Nourbakhsh and A. Pahwa, "A Robust Visual Odometry and Precipice Detection," in *IEEE International Conference on Robotics and Automation*, Barcelona, Spain, 2005.

[5] A. Kitanov, S. Bisevac and I. Petrovic, "Mobile robot self-localization in complex indoor environments using monocular vision and 3D model," *IEEE Xplore,* 2007.

[6] Y.-C. Chou and B.-S. Huang, "Mono Vision Particle Filter based Object Tracking with a Mobile Robot," *IEEE Xplore,* pp. 87-92, 2012.

[7] T. Oskiper, Z. Zhu, S. samarsekera and R. Kumar, "Visual odometry system using multile stereo cameras and inertial measurement unit," *IEEE Conference on CVPR,* 2007.

[8] N. Sunderhauf, K. Konolige, S. Lacroix and P. Protzel, "Visual Odometry Using Sparse Bundle Adjustment on an Autonomous Outdoor Vehicle," Tagungsband Autonome Mobile Systeme, 2005.

[9] Y. Cheng, M. Maimone and L. Matthies, "Visual Odometry on the Mars Exploration Rovers," Jet Propulsion Laboratory, Pasadena, CA, 2005.

[10] A. Geiger, J. Ziegler and C. Stiller, "StereoScan: Dense 3d Reconstruction in Real-time," *Intelligent Vehicles Symposium (IV),* 2011.

[11] N. Snavely, "CS4670/5670: Intro to Computer Vision," Ithaca, 2012.

[12] R. Szeliski, Computer Vision: Algorithms and Applications, London: Springer, 2011.

[13] "MathWorks," [Online]. Available: http://www.mathworks.com/help/vision/index.html. [Accessed 1 10 2013].

[14] D. G. Lowe, "Distinctive Image Features from Scale-Invariant Keypoints," International Journal of Computer Vision, Vancouver, 2004.

[15] A. E. T. T. L. V. G. Herbert Bay, "Speeded-Up Robust Features (SURF)," ETH Zurich BIWI, Zurich, 2006.

[16] S. Liu, "Localization Using Feature Matching In Near-Random Textures," Princeton University, 2013.

[17] S. Mattoccia, "Stereo Vision: Algorithms and Applications," University of Bologna, Bologna.

[18] "Tutorial: Kalman Filter with MATLAB example," Mathworks, [Online]. Available: www.mathworks.com. [Accessed 10 2013].

[19] D. Simon, "Kalman Filtering," in *Embedded Systems Programing*, 2001, pp. 72-79.

[20] M. I. Riberio, Kalman and Extended Kalman Filters:Concept.Derivation and Properties, Institute for Systems and Robotics, 2004.

[21] "MultiSense-SL," [Online]. Available: www.theroboticschallenge.com. [Accessed October 2013].

[22] J. J. LaViola Jr., "A Comparison of Unscented and Extended Kalman Filtering for Estimationg Quaternion Motion," [Online]. Available: http://www.eecs.ucf.edu/isuelab/publications/pubs/laviola_acc2003.pdf. [Accessed October 2013].

[23] H. William, ""RANSAC".EENG 512,Electrical Engineering and Computer Vision,Colorado School of Mines, Engineering Division.," [Online]. Available: http://inside.mines.edu/~whoff/courses/EENG512/index.htm. [Accessed October 2013].

[24] T. Oskiper, Z. Zhu, S. Samarasekera and R. Kumar, "Visual Odometry System Using Multiple Stereo Cameras and Inertial Measurement Unit," *IEEE Xplore,* 2007.

[25] J. Zhou and Y. Miao, Efficient Extended Kalman Filtering for altitude estimation based on gyro and vector observations, Aerospace Conference, 2010 IEEE, vol., no., pp.1,7, 6-13, 2010.

[26] T. Robertazzi and S. Schwartz, On applying th extended Kalman filter to non linear regression models, Aerospace and Electronic Systems, IEEE Transactions on, vol.25, no.3, pp.433,438, 1989.

[27] R. Faragher, Understanding the Basis of the Kalman Filter Via a Simple and Intuitive Derivation [Lecture Notes], Signal Processing Magazine, IEEE, vol.29, no.5, pp.128,132, 2012.

[28] R. Baheti, Efficient Approximation of Kalman Filter for Target Tracking, Aerospace and Electronic Systems, IEEE Transactions on, vol.AES-22, no.1, pp.8, 1986.

[29] G. A. Terejanu, "Unscented Kalman Filter Tutorial," [Online]. Available: http://users.ices.utexas.edu/~terejanu/files/tutorialUKF.pdf.

[30] E. A. v. d. M. R. Wan, "The Unscented Kalman Filter for Nonlinear Estimation," [Online]. Available: http://www.seas.harvard.edu/courses/cs281/papers/unscented.pdf. [Accessed October 2013].

[31] J. Shen, D. Tick and N. Gans, "Localization through fusion and discrete and continous epopolar geometry with wheel and IMU odmetry," *Proc.American Control Conference,* 2011.

[32] H. Hirschmuiller and D. Scharsteing, "Evaluation of Cost Functions for Stereo Matching," *IEEE Computer Society Conference on Computer Vision and Pattern Recognition,* 2007.

[33] US Department of the Interior, "The History of GPS," [Online]. Available: http://www.nps.gov/gis/gps/history.html. [Accessed 19 January 2014].

Appendices

A.I. List of Abbreviations

ARM: Acorn RISC Machine

BMP: Bitmap

DARPA: Defense Advanced Research Projects Agency

EKF: Extended Kalman Filter

FAST: Features from Accelerated Test

FPGA: Field Programmable Gate Array

FTDI: Future Technology Devices International

FTP: File Transfer Protocol

GRV: Gaussian Random Variable

GPS: Global Positioning System

GUI: Graphical User Interface

HDMI: High-Definition Multimedia Interface

IMU: Inertial Measurement Unit

JPEG: Joint Photographic Experts Group

MEMS: Micro-Electrical-Mechanical-System

OS: Operating System

PNG: Portable Network Graphics

RANSAC: Random Sample Consensus

RSS: Residual Sum of Squares

RTP: Real-time Transport Protocol

SAW: Surface Acoustic Wave

SIFT: Scale-Invariant Feature Transform

SIMD: Single Instruction Multiple Data

SLAM: Simultaneous Localization and Mapping

SoC: System on Chip

SSD: Summed up squared differences (SSD)

SURF: Speeded-Up Robust Features

TI: Texas Instruments

UDP: User Datagram Protocol

UKF: Unscented Kalman Filter

VCP: Virtual Com Port

A.II. Glossary

A

Accelerometer: Electromechanical device that is used to measure acceleration forces

ARM: An architecture of efficient low power processors frequently used in mobile devices and embedded systems.

C

Canny Method: Edge Detection Algorithm finds edges in an image by looking for local maxima in the Gaussian filter derivative of the image.

Corner Detection: Feature Detection process used to find local corners in an image by taking advantage of minimum and maximum *eigenvalues* from a matrix approximation of a SSD error.

D

Discrete Derivative: Derivative of a function with a discrete domain

Discrete Domain: A domain with a well-defined finite set of possible values

Disparity Map: The apparent pixel difference or motion between a pair of stereo images

E

Edge: A place of rapid change in the intensity function of an image.

Edge Detection: Feature detection process used to find edges in an image or set of images.

Eigenvalue: The multiplier yielded by an *eigenvector*

Eigenvector: a non-zero vector that, when multiplied by a specific matrix, yields a constant multiple the vector.

Extended Kalman Filter: Kalman filter which uses a first-order linear approximation of a nonlinear system

F

Feature Detection: Process involving the detection and extraction of unique features between two or more distinct features.

Feature Matching: Process involving the matching localization of equivalent unique features between two or more distinct features.

Focal Length: The measure of how strongly an optical system converges or diverges light

G

Gaussian Filter: A filter whose impulse response is a Gaussian Function.

Gaussian Function: A function having the form of a characteristic symmetric “bell curve” that quickly degrades to zero.

Gradient: A change in the magnitude of a property observed in passing from one point to another.

GStreamer: A pipelined based multimedia framework used for constructing graphs of media-handling components.

Gyroscope: Device used for measuring and maintaining orientation by way of the principles of angular momentum.

H

Haar Wavelet: A sequence of rescaled "square-shaped" functions which form a *wavelet* family when combined

Hessian Matrix: A square matrix of second-order partial derivatives of a function.

I

Inertial Odometry: Odometry through measurement of the angular rotation and forces in three-dimensional axes.

Intensity Function: Measurement of the radiant power per unit solid angle. In the case of image processing, this can be seen as the discrete change of pixel brightness along one pixel vector.

Isotopic: Having a physical property that has the same value when measured in different locations

K

Kalman Filter: Algorithm that produces estimation of unknown variable that describe a systems current set from noisy data and a dynamic model

L

Laplace Operator (Laplacian): A differential operator calculated by the divergence of the gradient of the function.

Laplacian of Gaussians Method: Edge Detection Algorithm that finds edges in an image by filtering the image with a Laplacian of Gaussian filter.

Laplacian of Gaussian Filter: A two-dimensional *isotropic* measure of the second *spatial derivative* of an image. The filter highlights regions of rapid intensity change.

Linear Regression Kalman Filter: Kalman filter that uses a statistical linearization technique to approximate a nonlinear system

Localization: Technique for determining one's position and heading within a given environment

M

Mechanical Accelerometer: Accelerometer consisting of a mass suspended by springs. The displacement of the mass is measured giving a signal proportional to the force acting on the mass in the input direction.

Mechanical Gyroscope: Gyroscope that consists of a spinning wheel mouthed upon two gimbals that wallow the wheel to rotate in three axes.

MEMS Accelerometer: Accelerometer implemented on a silicon chip, providing smaller size and less power consumption by sacrificing accuracy.

MEMS Gyroscope: Gyroscope implemented on a silicon chip, providing smaller size and less power consumption by sacrificing accuracy.

Mono-Camera System: Visual odometry system which makes use of only one image sensor (camera)

N

Nonlinear System: A system wherein the output is not directly proportional to the input.

O

Odometry: Estimation of the change in location over time through the utilization of electromechanical sensors

Optical Gyroscope: Gyroscope consisting of a large coil of optical fiber that uses light to measure angular velocity.

P

Payload: The "cargo" or body of a data transmission. Generally the fundamental data with the exclusion of the overhead data.

Pipeline: a set of data processing elements connected in series, where the output of one element is the input of the subsequent element

Pixel: The smallest controllable element or sample of an image.

Prewitt Operator: Edge Detection Algorithm that finds edges in an image by using Prewitt derivatives (operators)

Prewitt Operator: Derivative that calculates the difference of pixel intensities in an edge region. The coefficients of the derivative mask are fixed, and work so as to increase the edge intensity, while decreasing non-edge intensity in comparison to the original image.

R

Random Sample Consensus (RANSAC): An iterative method that estimates parameters of a mathematical model from a set of observed data which contains outliers.

Roberts Method: Edge Detection Algorithm that finds edges in an image by using Roberts derivatives (operators)

Roberts Operator: Convolution derivative that finds the gradient edges of an image at -45° and 45°. The edges are then produced by taking the RSS of the two convolutions.

S

Scale-Invariant Feature Transform (SIFT): Method for extracting distinctive invariant features from images.

Sigma Points: A minimal set of sample points picked up by an Unscented Kalman Filter

Sobel Method: Edge Detection Algorithm that finds edges in an image by using Sobel approximation derivatives (operators)

Sobel Operator: Derivative that calculates the difference of pixel intensities in an edge region. The coefficients of the derivative mask are variable, and work so as to increase the edge intensity, while decreasing non-edge intensity in comparison to the original image.

Sagnac effect: The shift in interference fringes from two coherent light beams travelling in opposite directions around a ring as the ring is rotated about a perpendicular axis.

SIMD: a form of parallel processing, utilizing instructions that perform the same operation on several pieces of data simultaneously.

Solid-State Accelerometer: Accelerometer that consists of a cantilever beam with a mass attached to the end of the beam

Spatial Derivative: Derivative that measures the change of a quantity in a given space.

Speeded-Up Robust Features: Novel scale and rotation invariant feature detector and descriptor claiming to be the fastest of similarly proposed schemes.

Stable Platform IMU: Inertial measurement unit that has the inertial system mount on a platform which is isolated from external rotational motion

Stereo-Camera System: Visual Odometry system which makes use of two or more image sensors (cameras)

Stereoscopic: Having the impression of depth and solidity. In relation to images, it refers to a pair of images taken at different angles, such that when the images are viewed together a depth dimension can be inferred.

Strap-down IMU: Inertial measurement unit that is mounting directly onto the device, therefore measuring output quantities in the body frame rather than the global frame

T

Taylor Series Expansion: A representation of a function as an infinite sum of terms that are calculated from the function derivatives at a single point.

Triangulation: Process of determining the location of a point by measuring angles to it from known points from the ends of a fixed baseline.

U

Unscented Kalman Filter: Kalman filter that provides a linear approximation of a nonlinear system without the use of derivatives

V

Visual Odometry: Odometry system that relies on change in location of a platform with respect to static objects in the surrounding environment

W

Wavelet: Wave-like oscillations with a positive amplitude that initiates and ends at zero

X

x86: The most common computer architecture, used in almost all PCs.

Z

Zero-Cross method: Edge Detection Algorithm that finds edges by looking for locations in the image where the value of the Laplacian changes sign.

A.III. Capella Camera Setup Guide

The Capella is an embedded pixel synchronous Stereo Vision Camera reference design for the TI OMAP35x series processors. This guide will provide a walkthrough to set up the Capella Camera for stereo vision applications. The guide assumes that the reader is using a Linux Operating system on their work computer.

A.III.I Getting Started

Connect an Ethernet cable between the Capella Camera and your work computer. Then insert a USB mini plug on the side port of the Camera. Connect the other end to a USB port on your work computer. This connection will serve as a serial port for communication between the camera and the work computer. At this point you may optionally connect an HDMI cable between the camera and a compatible monitor. You may also optionally connect a mouse and keyboard with the top USB mini port for direct communication with the Capella Camera. After the aforementioned connections have been set, connect the power supply to the DC power jack.

On the work computer, find the COM port corresponding to the Camera serial port. Open this serial port with your choice of serial terminal (e.g. minicom, terraterm, PuTTY). After the initialization sequence, the camera will ask for a password to login as root. The password is *root*. After login, type *ls* into the terminal to see a list of top level files and applications that are already on the camera. The camera comes with 2 demo applications from the manufacturing company. The functionality of these applications can be found in the Camera product brief. The V4l folder contains an application that allows for camera streaming and snapshots. The OpenCV folder contains a simple circle detector application that finds circular objects in the camera stream and outputs their position. The camera home folder will also have several bash files (files with the .sh extension) that have been created by this group to automate certain functionalities.

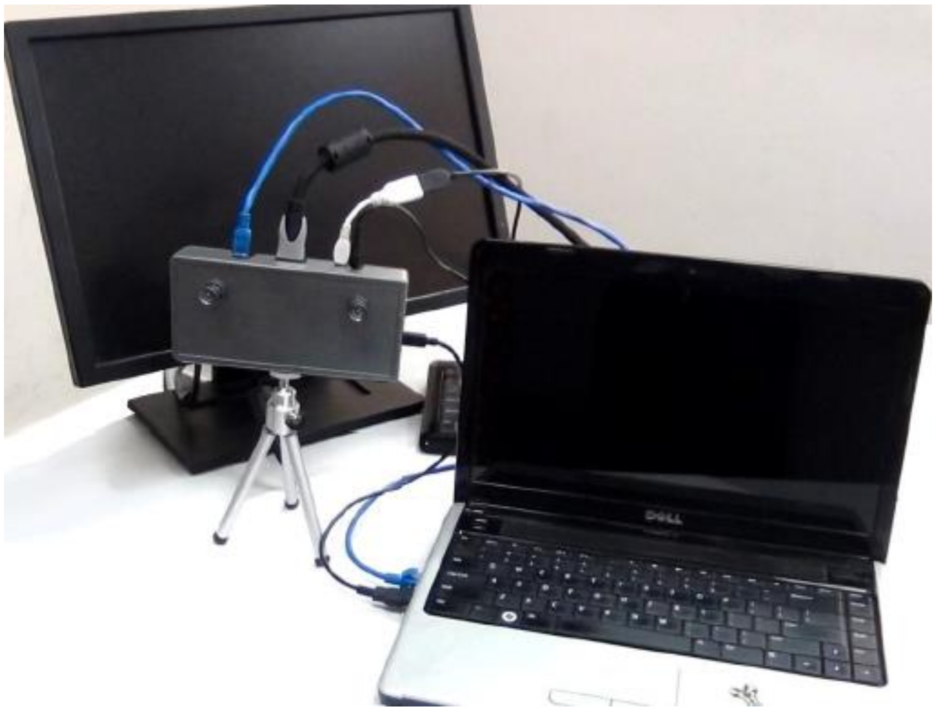

Figure A.I: Capella Camera Full Setup

A.III.II Configuring FTP Network

There is no direct access to the camera file system (without manually taking the camera apart). Thus, to add files and applications to the camera, the user must use a File Transfer Protocol network between the camera and the work computer. The Capella camera comes with a pre-installed FTP server, however before the server can be used, the camera IP address and netmask needs to be initialized. The IP address will serve as a local network for the camera Ethernet connection. To set the IP run the following command on the serial port terminal: *ifconfig eth6 192.168.1.10 netmask 255.255.255.0*. This will configure the Ethernet IP to the address 192.168.1.10 (this command will need to be run every time the camera boots up), this address can be configured to anything you wish so long as it is in the correct format (e.g. X.X.X.X). To run the FTP server, execute the following command in the terminal: *pure-ftpd &*.

On the work computer, the FTP network can be accessed through any open source FTP client, such as *Filezilla*. Upon opening the client of your choice, provide the previously configured IP address to the client, and type *root* for the password. You should now have be able to access any directory and file on the camera OS from within the FTP client. The group has created the *FTP_Config.sh* bash file which automates the FTP server process on the camera. To run the bash file, simply type *sh FTP_Config.sh* in the serial port terminal. The FTP network will prove instrumental in implementing additional functionality for the Capella Camera.

A.III.III Building GStreamer

The Capella Camera does not come with any means to transmit the video stream to the work computer (unless the computer has an HDMI-in port). As such, additional functionality for the camera is needed so as to achieve video streaming to another computer. *GStreamer* is an application that allows for the real-time video and audio streaming over Ethernet. The steps to build GStreamer for the Capella Camera are given below.

Scratchbox2 Cross-compiler

GStreamer will need to be cross-compiled for the Armv7 architecture in order to successfully be implemented on the camera. Scratchbox2 is a simple and effective cross-compiler for this purpose. The following is a summary of steps to install Scratchbox2 on your work computer.[1]

1. Install *QEMU* on the work computer by running the following commands from the terminal (some commands may need root access, to provide this, prefix the command with *sudo*):

```
git clone git://git.savannah.nongnu.org/qemu.git
cd qemu
git checkout -b stable v0.10.5
./configure --prefix=/$qemu_install_directory --target-list=arm-linux-user
make install
```

2. Once QEMU is installed, compile and install scratchbox2 with the following commands:

```
git clone git://anongit.freedesktop.org/git/sbox2
cd sbox2
./configure --prefix=/$SB2_install_directory
make install
```

3. After scratchbox2 is installed, add its location to the target path of the terminal.

[1] For further detail see: http://felipec.wordpress.com/2009/06/07/installing-scratchbox-1-and-2-for-arm-cross-compilation/

export PATH=/$SB2_install_directory /bin:$PATH

4. An ARM toolchain will be needed to configure the scratchbox2 target. A free version of the *CodeSourcery* toolchain can be used for this purpose.[2] Download and install the toolchain. The version used by this group was *arm-2009q3*. From here on *$CS* will be used to refer to the toolchain install directory.
5. The following commands will configure a target, which will represent your target filesystem:
   cd $CS/arm-none-linux-gnueabi/libc/sb2-init –c $qemu_install_directory/bin/arm-none-linux-gnueabi-gcc
   sb2-init -c $qemu_install_directory/bin/qemu-arm armv7 $CS/bin/arm-none-linux-gnueabi-gcc
6. Now cross-compilation for ARM7 architecture can be done by prefixing a command with *sb2*, for example: *sb2 ./configure --prefix=/TARGET_DIR*

Cross-Compiling the Glib Libraries

The GStreamer plugins require the GLib library in order to compile, as such the GLib library needs to first be cross-compiled. The following is a summary of steps to successfully cross-compile Glib for ARM7 architecture.[3] The variable *$TARGET/gst* will be used to represent the GStreamer target directory

1. Make sure that the ~/bin directory is in your path by executing the following command: *export PATH="$HOME/bin:$PATH"*
2. Before we can compile GLib, we must first compile and install the ZLib library, which GLib depends on. Cross-compile ZLib with the following commands:

```
wget -c http://zlib.net/zlib-1.2.5.tar.gz
tar -xf zlib-1.2.5.tar.gz
cd zlib-1.2.5
sb2 ./configure --prefix=$TARGET /gst
sb2 make install
```

3. Some versions of the GLib library contain bugs that fails to detect the ZLib library. To get arounf the bugs the C_INCLUDE_PATH and LDFLAGS globals have to manually be set by the following command: *export C_INCLUDE_PATH='$TARGET/gst/include' LDFLAGS='-L/$TARGET/gst/lib'*. If all else fails, try different versions of the GLib library until one is found that does not contain the bug.
4. Run the following commands to cross-compile the GLib library for ARM7:

```
git clone git://git.gnome.org/glib
cd glib
git checkout -b stable 2.24.1
./autogen.sh --noconfigure
sb2 ./configure --prefix=$TARGET/gst --disable-static --with-html-dir=/tmp/dump
sb2 make install
```

Cross-Compiling the GStreamer Plugins

At this point, the GStreamer core, base and extension plugins can finally be cross compiled. GStreamer has three major plugin packages: the *Good* (contains the most stable and

[2] CodeSourcery tool chain may be downloaded from: http://www.mentor.com/embedded-software/sourcery-tools/sourcery-codebench/editions/lite-edition/
[3] For further detail see: http://felipec.wordpress.com/2010/10/08/my-arm-development-notes/

tested plugins), the *Bad* (plugins that are not as extensively tested), and the *Ugly* (least tested and stable plugins). The following is a summary of steps to successfully cross-compile GStreamer for ARM7 architecture. As before, the variable *$TARGET/gst* will be used to represent the GStreamer target directory.

1. The first step is to download and install the core GStreamer framework. This is done with the following commands:
   ```
   git clone git://anongit.freedesktop.org/gstreamer/gstreamer
   cd gstreamer
   git checkout -b stable RELEASE-0.10.29
   ./autogen.sh --noconfigure
   sb2 ./configure --prefix=$TARGET/gst --disable-nls --disable-static --disable-loadsave --with-html-dir=/tmp/dump
   sb2 make install
   ```
2. Many GStreamer components require the *Liboil* library. The following commands cross-compile Liboil for our target:
   ```
   git clone git://anongit.freedesktop.org/liboil
   cd liboil
   git checkout -b stable liboil-0.3.17
   ./autogen.sh --noconfigure
   sb2 ./configure --prefix=$TARGET/gst --disable-static --with-html-dir=/tmp/dump
   sb2 make install
   ```
3. Now the GStreamer base plugins will be installed. These plugins provide the fundamental functionality of GStreamer. The following commands will cross-compile the base plugin package for our target:
   ```
   git clone git://anongit.freedesktop.org/gstreamer/gst-plugins-base
   cd gst-plugins-base
   git checkout -b stable RELEASE-0.10.29
   ./autogen.sh --noconfigure
   sb2 ./configure --prefix=$TARGET/gst --disable-nls --disable-static --with-html-dir=/tmp/dump
   sb2 make install
   ```
4. The *Good* plugins package can be installed with the following commands:
   ```
   git clone git://anongit.freedesktop.org/gstreamer/gst-plugins-good
   cd gst-plugins-good
   git checkout -b stable RELEASE-0.10.23
   ./autogen.sh --noconfigure
   sb2 ./configure --prefix=$TARGET/gst --disable-nls --disable-static --with-html-dir=/tmp/dump
   sb2 make install
   ```
5. The *Bad* and the *Ugly* plugin packages can be installed similarly to steps 3 and 4.
6. Every time you open a new terminal is opened, and you wish to cross-compile, you must first manually export the package configuration paths with the following command: *export PKG_CONFIG_PATH=$TARGET/gst/lib/pkgconfig*

Transferring GStreamer onto the Capella Camera

Now that GStreamer has been built for an ARM7 architecture, it must be transferred over to the Capella Camera Operating System. This is where the previously configured FTP network comes in. Using the FTP client, copy the contents of the $TARGET directory to the */opt* folder in the Camera file system (you will have to back out of the home folder in the camera, where upon you will see all of the system folders, including the */opt* folder). After the contents have been copied, make sure they are given full user permissions (if using the Filezilla client, you can right click on the copied folder in the Capella file system, select "change permissions" and then type 777 to give full read/write/execute permissions to the user. After this is complete, GStreamer should be fully operational on the Capella Camera.

A.III.IV Transmitting and Receiving the Camera Video Stream

After GStreamer is installed on the camera, a GStreamer pipeline can be created to transmit the camera video feed over Ethernet to a receiving computer. The receiving computer must also have GStreamer installed. If the receiving computer is a standard PC or laptop running Linux, the installation process is as simple downloading the GStreamer application and running the installer If the receiver is another ARM machine, then GStreamer will have to be installed in a process similar to the Capella Camera (alternatively if the receiver is also ARM7 the user can simply copy the cross-compiled GStreamer folder in the target directory, over to the receiver file system).

Transmitting the Video Stream

Every time the Capella Camera boots up, the user must export the GStreamer library locations. This can be done by executing the following commands through the serial port terminal:

export PATH=/opt/arm/gst/bin:/user/:$PATH
export GST_PLUGIN_PATH=/opt/arm/gst/lib/gstreamer-0.10:/usr/share/gstreamer-0.10
export LD_LIBRARY_PATH=/opt/arm/gst/lib:/usr/lib

Now the GStreamer pipeline of your choice can successfully be executed. Unfortunately, GStreamer is not designed to stream stereoscopic feeds, and does not recognize the Capella Camera /dev/video4 device, which contains both the left and right streams combined together. The following pipeline can be used to transmit the left and right camera video feeds to different ports within the same pipeline.

```
gst-launch-0.10 -v v4l2src device=/dev/video0 always-copy=false ! 'video/x-raw-
gray,format=(fourcc)UYVY,width=640,height=480,framerate=5/1' ! ffmpegcolorspace
! rtpvrawpay ! multiudpsink clients=\"192.168.1.1:4000\" v4l2src
device=/dev/video3 always-copy=false ! 'video/x-raw-
gray,format=(fourcc)UYVY,width=640,height=480,framerate=5/1' ! ffmpegcolorspace
! rtpvrawpay ! multiudpsink clients=\"192.168.1.1:5000\"
```

While the Overo WaterSTORM COM processor used by the Capella Camera has DSP capabilities, the DSP drivers were not included with the Capella Reference design. As such, some of the more sophisticated GStreamer pipelines, such as video encoding, cannot be done on the Capella. Likewise, because the Capella effectively has no DSP, the GStreamer pipeline takes up considerable CPU usage (about %97). It is thus recommended that no other processes be run on the camera while the GStreamer pipeline is active. The *Initialization.sh* bash script created by this group automates the GStreamer transmission pipeline for the Capella Camera

Receiving the Video Stream

A GStreamer pipeline will need to be initiated on the receiving end in order to obtain the video stream. This pipeline will be fundamentally similar to the pipeline of the transmitter. The following is the respective receiving pipeline for the transmission pipeline shown above:

```
      gst-launch-0.10 udpsrc port=4000 caps = 'application/x-rtp,
media=(string)video, clock-rate=(int)90000, encoding-name=(string)RAW,
sampling=(string)YCbCr-4:2:0, depth=(string)8, width=(string)640,
height=(string)480, colorimetry=(string)SMPTE240M, payload=(int)96,
ssrc=(uint)3586515688, clock-base=(uint)2274023560, seqnum-base=(uint)17136' !
rtpvrawdepay ! ffmpegcolorspace !  jpegenc quality=100 ! multifilesink
location=$HOME/IMAGES/imgL%d.jpg  udpsrc port=5000 caps = 'application/x-rtp,
media=(string)video, clock-rate=(int)90000, encoding-name=(string)RAW,
sampling=(string)YCbCr-4:2:0, depth=(string)8, width=(string)640,
height=(string)480, colorimetry=(string)SMPTE240M, payload=(int)96,
ssrc=(uint)3586515688, clock-base=(uint)2274023560, seqnum-base=(uint)17136' !
rtpvrawdepay ! ffmpegcolorspace ! jpegenc quality=100 ! multifilesink
location=$HOME/IMAGES/imgR%d.jpg
```

As can be seen, this pipeline is accessing the ports (4000 and 5000) created by the transmission pipeline. The highlighted *caps* value comes directly from the transmission pipeline. Upon running the transmission pipeline, the serial monitor will print out several values and pseudo pipelines. Among these values are the *caps* declarations. Simply copy the caps value from the serial port, and set it on the receiving pipeline. The pipeline above is saving the video stream in a folder, as a series of JPEG images. The video can also be made to play live by removing the *jpegenc* and *multifilesink* plugins, and instead replacing them with the *autovideosink* plugin.

A.IV. OMAP5432 EVM Setup Guide

The purpose of this section is to document the setup of the Ubuntu Linux OS on the TI OMAP5432 EVM, including the changes made to the OS and the additional programs installed in order to achieve the required functionality. These range from rebuilding the Linux kernel with additional functionality to simple package installations. Additionally, this section will review the scripts and programs used to configure the EVM for collecting and processing data and for obtaining updates from the internet. A basic understanding of Unix-like systems is assumed. In this section the term "EVM" will be used to refer to the Texas Instruments OMAP5432 Evaluation Module as both a hardware and software device. When discussing operating systems, "the OS" or "Linux" will refer to the Ubuntu 12.04 LTS distro of Linux that was installed on the EVM and on the host machine unless otherwise specified.

Many of the changes made to the OS were not implemented in the order described here, but instead as the problem they corrected was discovered. For the sake of simplicity, however, they are documented in an order that builds to a final system in a cleaner manor. Finally, remaining issues with the OS and platform will be discussed. These relate primarily to ease of use issues that do not affect the actual functionality of the system.

A.IV.I. Host System

TI supplies a set of software tools that allow users to easily build and install Ubuntu 12.04 for the EVM, called the TI GLSDK. These tools require a Linux host with Ubuntu 12.04 installed. Instead of acquiring a dedicated machine, our team used a virtual machine.

A.IV.II. Installing the TI GLSDK

Refer to the documentation for installing the GLSDK provided by TI. Version 6.00.00.07 was used as it was the last version to support Ubuntu as the target OS. As in the TI documentation, $GLSDK will be used when referring to the directory the SDK is installed in. On our host, the GLSDK was installed in /opt.

A.IV.III. Rebuilding and Installing the Linux Kernel

The EVM boots off a bootable micro SD card that contains the operating system it will be using. This section will describe the process of building a suitable Linux kernel, and then placing it on the micro SD card along with the file system and bootloader. Although the GLSDK come with a prebuilt Linux kernel, this kernel does not include drivers for FTDI USB to serial devices. This driver is part of the Linux kernel, and is included in the Ubuntu distribution by default, however the configuration file used to make the provided kernel does not include this feature. Configuration files are files that describe the features to be included in a build by the make utility. Although they are text files, they should only be modified with special tools. To enable FTDI drivers in the configuration file, execute the following commands on the host computer. Modifying the configuration file and building the kernel are relatively straightforward operations; however it will take a good deal of time, possibly an hour or more on a typical PC, for the kernel to be built.

The first step is to back up the makefile, and copy it to the Linux directory so that it can be modified. On our host machine, our user did not own the development folder so we had to use sudo for much of the process. To avoid this hassle, a root user session is started before running through these commands.

```
> sudo -s

> cd $GLSDK/board-support/Linux_3.8.4
> cp ./arch/arm/configs/omap2plus_defconfig
./arch/arm/configs/omap2plus_defconfig_backup
```

```
> cp ./arch/arm/configs/omap2plus_defconfig ./.config
```

Next menuconfig is used to modify the config file. Menuconfig is a program that provides a graphical interface for modifying config files. It is important to specify which architecture the configuration file is to be used for, as otherwise menuconfig will assume it is for a 386 machine.

```
> export ARCH="arm"
```

```
> make menuconfig
```

A GUI will appear on the screen. Using the arrow keys, navigate to *Device Drivers* > *USB Support* > *USB Serial Converters*. Press 'Y' while *USB Serial Converters* is selected to include it in the build. Next enter into *USB Serial Converters*, select *USB FTDI Single Port Serial Driver* and press 'Y'.

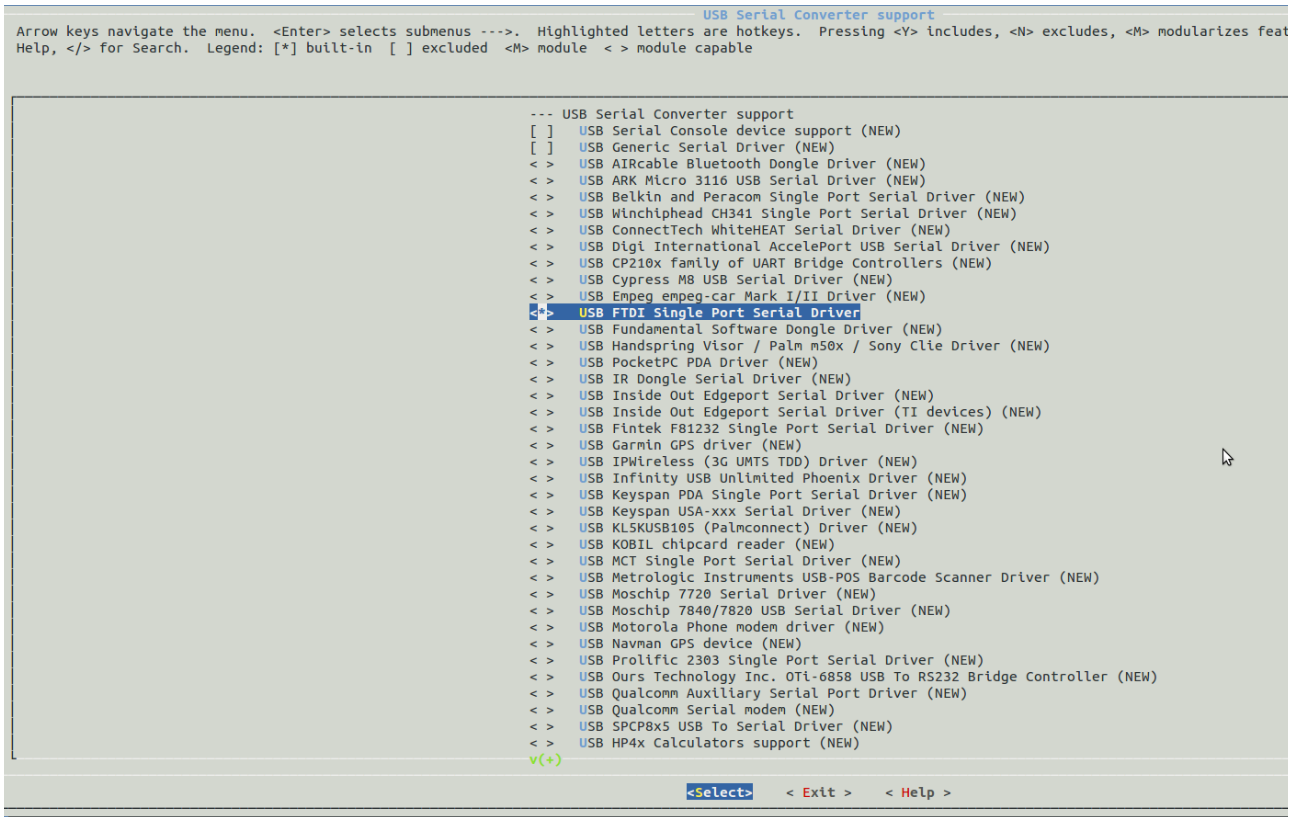

```
                                    USB Serial Converter support
 Arrow keys navigate the menu.  <Enter> selects submenus --->.  Highlighted letters are hotkeys.  Pressing <Y> includes, <N> excludes, <M> modularizes feat
 Help, </> for Search.  Legend: [*] built-in  [ ] excluded  <M> module  < > module capable

                                --- USB Serial Converter support
                                [ ]   USB Serial Console device support (NEW)
                                [ ]   USB Generic Serial Driver (NEW)
                                < >   USB AIRcable Bluetooth Dongle Driver (NEW)
                                < >   USB ARK Micro 3116 USB Serial Driver (NEW)
                                < >   USB Belkin and Peracom Single Port Serial Driver (NEW)
                                < >   USB Winchiphead CH341 Single Port Serial Driver (NEW)
                                < >   USB ConnectTech WhiteHEAT Serial Driver (NEW)
                                < >   USB Digi International AccelePort USB Serial Driver (NEW)
                                < >   USB CP210x family of UART Bridge Controllers (NEW)
                                < >   USB Cypress M8 USB Serial Driver (NEW)
                                < >   USB Empeg empeg-car Mark I/II Driver (NEW)
                                <*>   USB FTDI Single Port Serial Driver
                                < >   USB Fundamental Software Dongle Driver (NEW)
                                < >   USB Handspring Visor / Palm m50x / Sony Clie Driver (NEW)
                                < >   USB PocketPC PDA Driver (NEW)
                                < >   USB IR Dongle Serial Driver (NEW)
                                < >   USB Inside Out Edgeport Serial Driver (NEW)
                                < >   USB Inside Out Edgeport Serial Driver (TI devices) (NEW)
                                < >   USB Fintek F81232 Single Port Serial Driver (NEW)
                                < >   USB Garmin GPS driver (NEW)
                                < >   USB IPWireless (3G UMTS TDD) Driver (NEW)
                                < >   USB Infinity USB Unlimited Phoenix Driver (NEW)
                                < >   USB Keyspan PDA Single Port Serial Driver (NEW)
                                < >   USB Keyspan USA-xxx Serial Driver (NEW)
                                < >   USB KL5KUSB105 (Palmconnect) Driver (NEW)
                                < >   USB KOBIL chipcard reader (NEW)
                                < >   USB MCT Single Port Serial Driver (NEW)
                                < >   USB Metrologic Instruments USB-POS Barcode Scanner Driver (NEW)
                                < >   USB Moschip 7720 Serial Driver (NEW)
                                < >   USB Moschip 7840/7820 USB Serial Driver (NEW)
                                < >   USB Motorola Phone modem driver (NEW)
                                < >   USB Navman GPS device (NEW)
                                < >   USB Prolific 2303 Single Port Serial Driver (NEW)
                                < >   USB Ours Technology Inc. OTi-6858 USB To RS232 Bridge Controller (NEW)
                                < >   USB Qualcomm Auxiliary Serial Port Driver (NEW)
                                < >   USB Qualcomm Serial modem (NEW)
                                < >   USB SPCP8x5 USB To Serial Driver (NEW)
                                < >   USB HP4x Calculators support (NEW)
                                v(+)

                                          <Select>    < Exit >    < Help >
```

Figure A.II - Using menucofig to include FTDI drivers in kernel build

Use the *Exit* selection at the bottom of the screen to exit out of each level. At the top level, press *Exit* again and chose to save your changes. Copy the configuration file back to the directory where it came from, and use the GLSDK to build the kernel.

```
> cp ./.config ./arch/arm/configs/omap2plus_defconfig
```

```
> cd $GLSDK
```

```
> make linux_clean
```

```
> make linux
> make linux_install
```

The build process for Linux may take an hour or more depending on the machine used to do it. Once it is done, use install to put the kernel files in a place you can find them, as shown above. This will be a location you chose during the installation of the GLSDK for the target file system, with the default value being in your home directory. This file path can be found in $GLSDK/Rules.make at the bottom of the file in the variable EXEC_DIR. Our files were moved to /home/USER/targetfs/home/root/omap5. This directory will be referred to as $EXEC_DIR in the instructions below, however it should be noted that this will need to be replaced with the actual direct path, as the variable is not exported from the script. In this directory the files will be contained in the boot directory, making the complete path /home/USER/targetfs/home/root/omap5/boot.

These final instructions move the newly built kernel to where the SD build script can find it and use the GLSDK to make a bootable micro SD card. Make sure the micro SD card that will be used is connected to the host system and that there is no important data on it, as it will be completely and irreversibly erased. To check which disk in /dev in the micro SD card, use `fdisk -l` and look for the drive that matches the size of your disk.

```
> cp -r ./board-support/prebuilt-images ./board-support/prebuilt-images-backup
```

```
> cp -r $EXEC_DIR/boot/ ./board-support/prebuilt-images/
```

```
> ./bin/mksdboot.sh
```

The script will prompt for which disk to use. Agree to the prompts, and once the script is done the micro SD card should be ready to boot from. At the end, exit from the sudo session.

```
> exit
```

A.IV.IV. Installing Packages and Initial Setup

Supply the board with power and connect the debug port to the host computer using a USB cable. On a host with the GLSDK installed, a minicom session with the board can be started by typing `sudo minicom -w`. Note that the board may take some time to boot. Once the target system has booted, log in as root if a prompt is presented. TI has provided a script that installs and sets up many of the basic packages that are required for using the system. To install these packages the board needs network access. The only building on the WPI campus that our group found to allow the board on the WPI network was the Gordon Library. Once the Ethernet is connected, run the setup script on the target device. This may take some time to complete. After the script completes, it may be helpful to install some additional packages to aid in debugging.

```
> ./first-boot.sh
```

```
> sudo apt-get install net-tools usbutils
```

A.IV.V. Scripts and Rules

Automated setup and execution of different parts of the system was achieved through the use of several different scripts. Each of the required scripts is listed below, with a brief descript of what is does, its file path, and the content of the script.

Rules for udev

To automate the usage of serial ports connected through FTDI devices, the devices need to appear with the same name in /dev each time they turn on. This includes the XBee, the Capella camera serial connection, and the Arduino. By default, devices attached to the next open /dev/ttyUSB*, with no guaranteed order. To fix this, the udev rules were modified to create a more descriptive name for each device.

It should be placed in /etc/udev/rules.d/45-custom-serial-names.rules.

```
# Makes simlinks with more appropriate names for all the FTDI devices

SUBSYSTEMS=="usb", KERNEL=="ttyUSB*", ATTRS{idVendor}=="0403",
ATTRS{idProduct}=="6001", ATTRS{serial}=="AE00EVL7", SYMLINK+="ttyCapella"

SUBSYSTEMS=="usb", KERNEL=="ttyUSB*", ATTRS{idVendor}=="0403",
ATTRS{idProduct}=="6001", ATTRS{serial}=="A702NVF7", SYMLINK+="ttyXBee"
```

Python Script to Start GStreamer on the Capella Camera

This brief script logs into the Capella Camera and runs the script placed in the root user's home directory on the Capella that starts sending image data to the EVM. If the corresponding GStreamer client is not running on the EVM, the data is ignored.

This script should be /root/startGSTServer.py .

```
#!/usr/bin/env python
import serial
ser=serial.Serial("/dev/ttyCapella", 115200, timeout=1)
ser.write("root\n")
ser.write("\n")
ser.write("sh Inititalization.sh\n")
ser.close()
```

GStreamer Client

This bash script first configures the Ethernet interface on the EVM to connect with the Capella. Next, if the USB drive used for image storage is plugged in, it is mounted if it is not already. The folder for the images to be stored in is cleared, and finally the GStreamer client is started.

This script should be placed in /root/rximg-jpeg.sh

```
#!/bin/bash

#Camera stream setup

ifconfig eth0 192.168.1.1 netmask 255.255.255.0

echo "Network configured"
ifconfig | head -n 2
echo "Preparing image folder..."

if [ -e "/dev/sda1" ]; then
  mountpoint -q /u || mount /dev/sda1 /u
  TARGETDIR=/u/IMAGES
else
  echo "Can't find Removable Drive, saving images to HOME directroy"
  TARGETDIR=~/IMAGES
fi

if [ -e "$TARGETDIR" ]; then
  rm -R $TARGETDIR
```

```
fi

mkdir $TARGETDIR
echo "Image directory cleared"
echo "Images will be stored in ${TARGETDIR}"

gst-launch-0.10 udpsrc port=4000 caps = 'application/x-rtp,
media=(string)video, clock-rate=(int)90000, encoding-name=(string)RAW,
sampling=(string)YCbCr-4:2:0, depth=(string)8, width=(string)640,
height=(string)480, colorimetry=(string)SMPTE240M, payload=(int)96,
ssrc=(uint)3586515688, clock-base=(uint)2274023560, seqnum-
base=(uint)17136' ! rtpvrawdepay ! ffmpegcolorspace !  queue ! jpegenc
quality=100 ! multifilesink location=$TARGETDIR/imgL%d.jpg  udpsrc
port=5000 caps = 'application/x-rtp, media=(string)video, clock-
rate=(int)90000, encoding-name=(string)RAW, sampling=(string)YCbCr-4:2:0,
depth=(string)8, width=(string)640, height=(string)480,
colorimetry=(string)SMPTE240M, payload=(int)96, ssrc=(uint)3586515688,
clock-base=(uint)2274023560, seqnum-base=(uint)17136' ! rtpvrawdepay
!ffmpegcolorspace ! queue ! jpegenc quality=100 ! multifilesink
location=$TARGETDIR/imgR%d.jpg

echo "GStreamer client started"
```

A.V. Parsing IMU Data

After a full duplex SPI communication was established between the devices, IMU register values were parsed to obtain angular rates in degrees per second. The gyroscope and accelerometer output data is a 32 bit twos complement format. Each IMU register is 16 bits and hence two IMU register reads are required to get the complete data. Figure 6 shows registers that need to be read to get X-axis gyroscope data and how to convert X_GYRO_OUT register value to angular rate in degrees per second. Using the X_GYRO_OUT register provides sufficient resolution for the project so X_GYRO_LOW register was not read because of the processing delay associated with reading in a register through SPI. Other gyroscope registers were parsed similarly following the data format for each register as described in the datasheet.

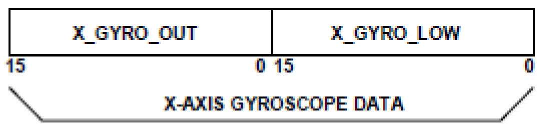

Rotation Rate	Decimal	Hex	Binary
+300°/sec	+22,887	0x5967	0101 1001 0110 0111
+0.026216/sec	+2	0x0002	0000 0000 0000 0010
+0.013108°/sec	+1	0x0001	0000 0000 0000 0001
0°/sec	0	0x0000	0000 0000 0000 0000
−0.013108°/sec	−1	0xFFFF	1111 1111 1111 1111
−0.026216°/sec	−2	0xFFFE	1111 1111 1111 1110
−300°/sec	−22,887	0xA699	1010 0110 1001 1001

Figure A.III: X gyro data format

To read in Arduino data through a serial port, a python script was developed using the pySerial module. pySerial provides backends for Python running on Windows and Linux to provide access to serial port. A script was written using this module so that serial data coming in from Arduino can be read in Linux running on the OMAP EVM. Figure 10 shows the parsed data printed by Arduino to a serial port on the laptop.

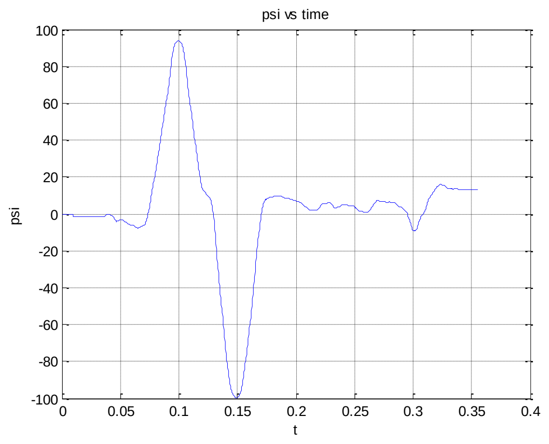

Figure A.IV: Angular rotation Z axis by parsing data in Arduino. Units of Y axis is degrees and units of X axis is seconds.

A.VI. Legacy Designs

The following were previous potential system designs devised before deciding on the final implementation.

A.VI.I. FPGA Design

The FPGA based system shown in Figure A.V was the first proposed design by the group. This system would have taken advantage of the parallelization properties of FPGA systems in order to obtain much faster feature detection and matching solutions. As such, this design would been more ideally suited for a real-time application design. Nevertheless, implementing feature detection and matching algorithms on an FPGA platform proved to be too time consuming to implement within the scope of this project. Additionally, as this system would have been more expensive overall due to requiring both a fairly powerful FPGA and a microprocessor,.

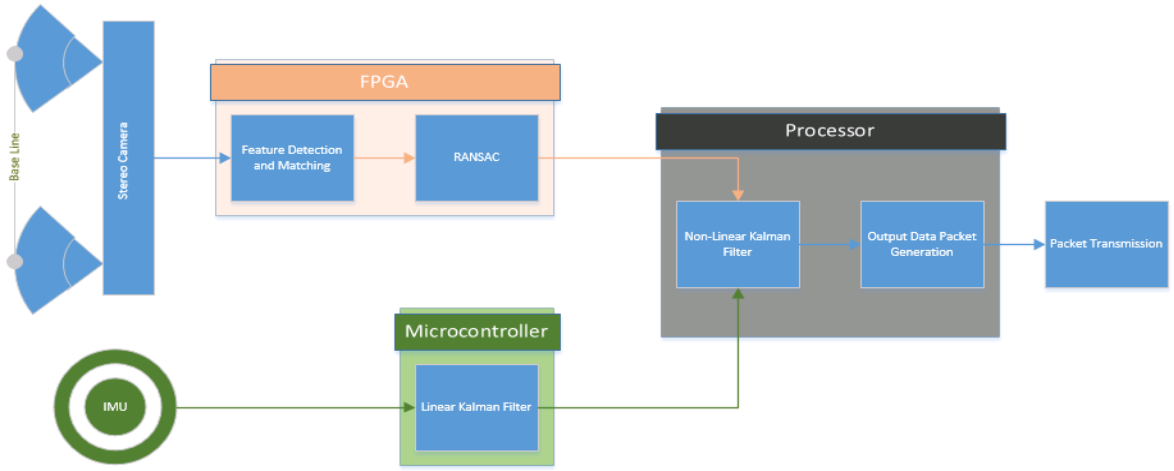

Figure A.V: FPGA based Design

A.VI.II. ZedBoard Based Design

A possible implementation based around the ZedBoard was entertained for a time. The Zedboard is a low cost development board which contains both a programmable logic (PL) section, and a Xilinx Zynq 7000 SoC (System on chip) processor. The Zynq 7000 is a dual core ARM Cortex A9 processor rated at a nominal 800MHz. As the Zedboard allows for development on both programmable logic (FPGA) and software (via ARM processor) environments, it is ideally suited to approximate the practicality of our original system (which contained both environments).

The ZedBoard design was created with the intention that the Arm processor would run an embedded Linux environment which would contain a software implementation of a Sobel filer as well as provide a means of communication between peripherals. Conversely, the programmable logic would be used for hardware acceleration, and also contain a hardware implementation of the Sobel filter. This was done so as to benchmark the relative speeds of the hardware and software implementations. Ultimately it was found that there was a significant communication bottleneck between the hardware and the OS, creating large latency for the hardware implementation of the Sobel filter. Additionally the Zedboard processor was not powerful enough to run the feature detection and matching algorithms at a close to real-time frame rate. Thus, the students opted instead to simply use a powerful embedded processor without programmable logic.

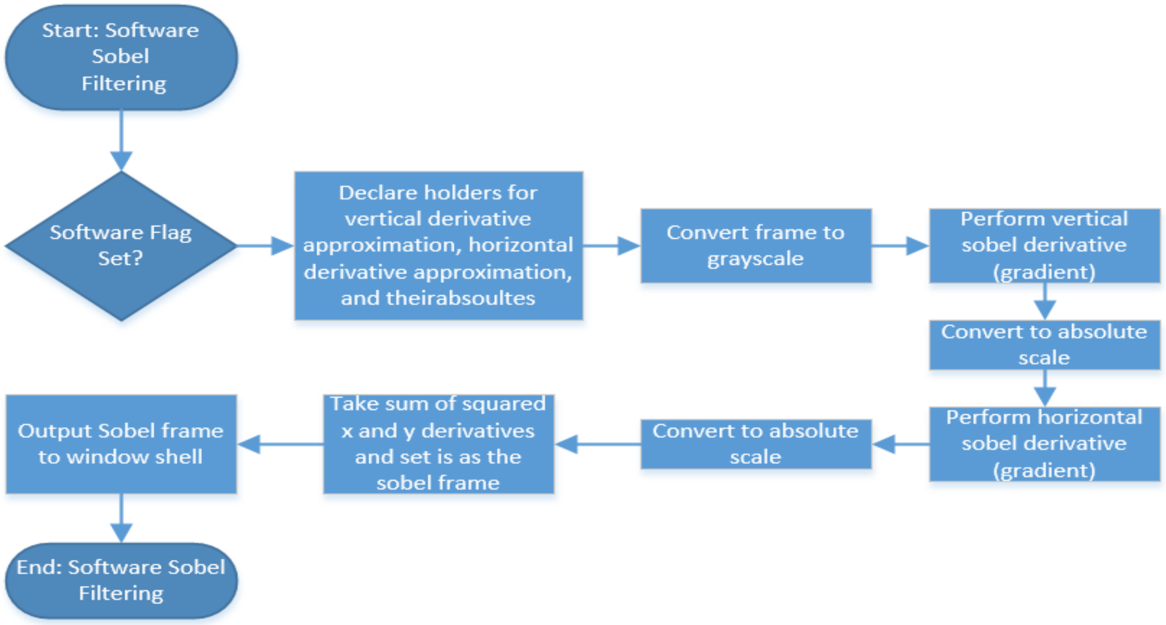
Start: Software Sobel Filtering
Software Flag Set?
Declare holders for vertical derivative approximation, horizontal derivative approximation, and theirabsoultes
Convert frame to grayscale
Perform vertical sobel derivative (gradient)
Convert to absolute scale
Perform horizontal sobel derivative (gradient)
Convert to absolute scale
Take sum of squared x and y derivatives and set is as the sobel frame
Output Sobel frame to window shell
End: Software Sobel Filtering

Figure A.VI: Flowchart of Software filtering on ZedBoard

A.VI.III. Processor Core Based Design

The Processor Core based design is provided by XX. This design is virtually identical to the final realized system with some notable exception. This design has all the functionality within the OMAP5432 processor, with the major algorithms each being given their own cores for processing. Similarly this system also took advantage of the AM M4 cores located on the processor for some of the smaller algorithms. While this system is ideal in theory, the group discovered that we did not have as much free range to customize the processor cores as previously anticipated. Likewise, the LCD screen output on the system was eventually dropped due to timing constraints.

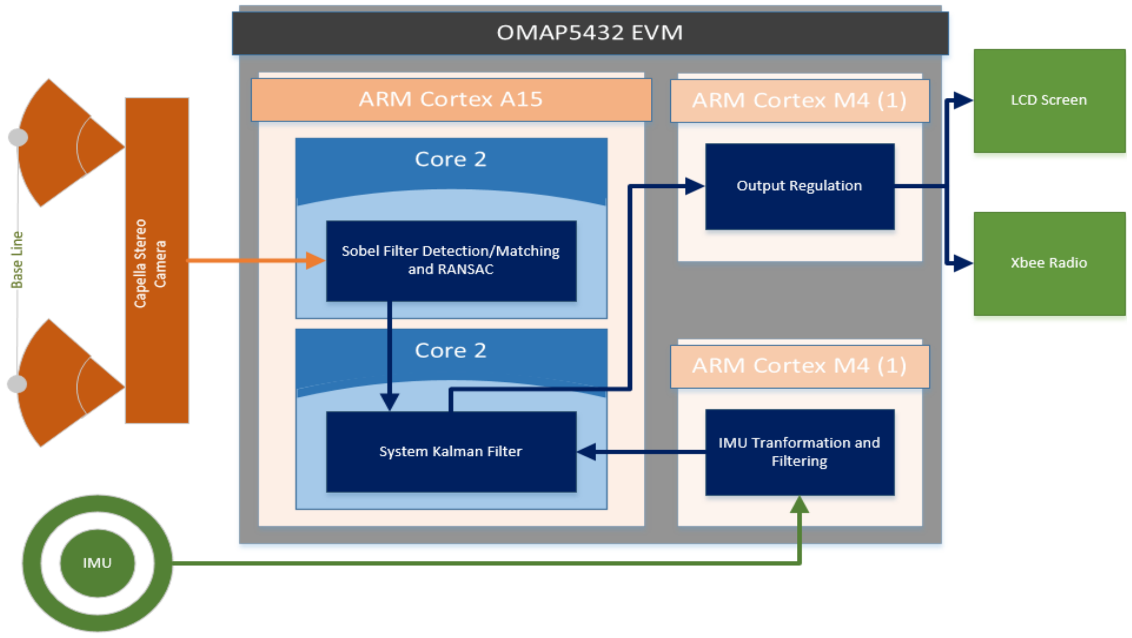

Figure A.VII: Processor Core based Design

A.VII. Other Stereo Vision Camera Systems

This appendix provides an overview for a variety of currently existing stereo vision cameras, and stereo vision camera system packages.

A.VII.I. Surveyor Vision System

Website: http://www.surveyor.com/stereo/

This is an open-source stereo vision system targeted towards research and hobbyist applications.

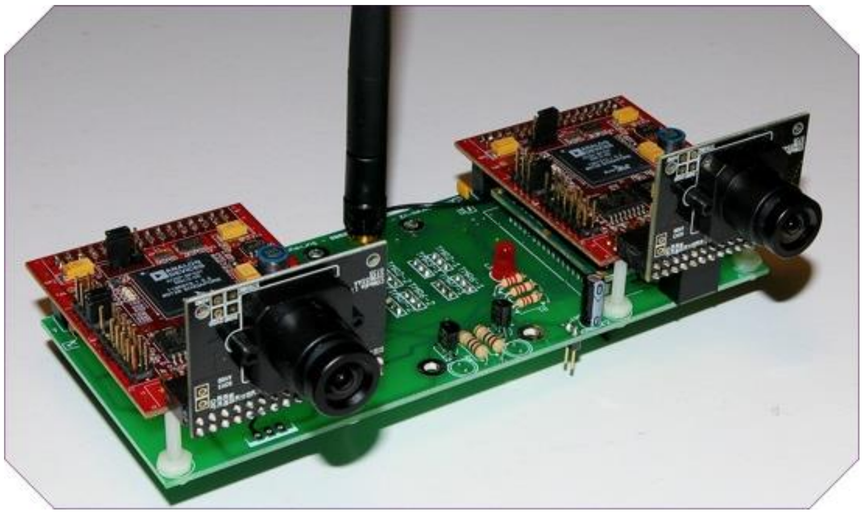

Figure A.VIII: Surveyor Stereo vision system

Table A.I: Specifications and Features for Surveyor Stereo Vision System

SPECIFICATIONS AND FEATURES		QUANTITY ON SYSTEM
PROCESSOR	500 MHz Analog Devices	2 (1 for each camera)
MEMORY	32MB SDRAM, 4MB SPI Flash	2(1 for each camera)
PORTS/BUSES	JTAG, SPI, I2C, 16 GPIO (general purpose input/output), external 32-pin I/O header (with 2 UARTS	2(1 for each camera)
CAMERA	Omnivision OV9655 1.3 megapixel sensor	
COMMUNICATION	Processor-Processor communications via SPI. WLAN 802.11g radio for Wifi	1
POWER	On board 3.3V switching regulator. Dual h-bridge motor driver with 1A drive current per motor. 2 switching transistor driver (100mA drive) Low battery detect circuit Total Power Draw: ~2W (300mA @7.4V)	1
BOARD DIMENSIONS	60mmX150 mm	1
PRICE	~$550.00 (when it was last available	

Schematics and Drawings

Stereo Vision Module - http://www.surveyor.com/blackfin/bfin-stereo-v2.png
Camera Schematic - http://www.surveyor.com/blackfin/SRV1-bfin-schematic.pdf
Camera Module Schematic - http://www.surveyor.com/blackfin/AA9655-schematic.jpg

A.VII.II. MEGA-DCS Megapixel Digital Stereo Head

Website: http://users.rcn.com/mclaughl.dnai/sthmdcs.htm

The MEGA-DCS is an all-digital stereo head for machine vision tasks, emphasizing high performance in a low power, compact package.

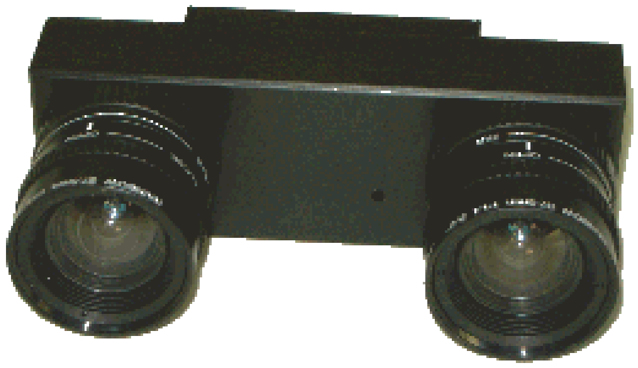

Figure A.IX: MEGA-DCS Megapixel Digital Stereo Head

Table A.II: Specifications and Features for MEGA-DCS Megapixel Digital Stereo Head

SPECIFICATIONS AND FEATURES	
CAMERA RESOLUTION	1280Hx960V pixels
IMAGERS	½" format CMOS, color or monochrome
FORMATS	1280x960 or 640x480, 8-bit monochrome or Bayer color
FRAME RATES	3.75, 7.5, 15, 30 Hz. MAX: 7.5 Hz at 1289x960
GAIN	0-22 dB
SENSITIVITY	2.5 V/lux-sec
S/N	>55 dB
POWER	< 1W
LENS	6.0 mm F 2.4 C mount included 3.5 mm and 12 mm lens optional
SIZE	1.5'' x 5" x 1"
SVS SOFTWARE	Linux kernel 2.4, MSW98SE, ME, 2000, XP
INTERFACE	Single cable for power, data, and control
PRICE	$1,600.00

Manual and References

Manual: http://users.rcn.com/mclaughl.dnai/sthmdcs.pdf
Color/Monochrome Reference: http://users.rcn.com/mclaughl.dnai/sthmdzcs_color.htm
Lens Options: http://users.rcn.com/mclaughl.dnai/sthmdcs_lenses.htm
Pricing Options:
http://users.rcn.com/mclaughl.dnai/Videre%20Design%20Order%20Form%20March%202003.pdf

A.VII.III. PCI nDepth Vision System

Website: http://www.focusrobotics.com/products/systems.html

Vision System targeted towards companies and individuals looking to add real-time depth perception to an existing PC platform.

Figure A.X:nDepth Stereo Vision System

Table A.III: Specifications and Features for nDepth Stereo Vision System

SPECIFICATIONS AND FEATURES	
PROCESSOR SUBSYSTEM	
FRAME RATE	30 fps
RESOLUTION	WVGA (752x480)
CALIBRATION ERROR	.1 pixel RMS error
STEREO ALGORITHM	Sum of Absolute Differences (SAD) with 9x9 block matching
HOST INTERFACE	Standard PCI 33, direct DMA access
STEREO VISION CAMERA	
RESOLUTION	Two 752x480, 1/3 inch VGA CMOS digital image sensors
FRAME RATE	Up to 60 fps
BASELINE	6cm
IMAGE FORMATS	Monochrome
DYNAMIC RANGE	>60dB
A-D CONVERSION	10 bit
SHUTTER TYPE	Global shutter photodiode pixels. Simultaneous integration and readout
CONTROLS	Automatic and manual synchronized exposure + gain control
INTERFACE	LVDS on CAT6 cable
POWER CONSUMPTION	< 1W at maximum data rate
HOST SOFTWARE SUBSYSTEM	
DRIVERS	Linux and Windows (for access to depth image, undistorted, and calibrated images
CONTROL API	Includes programming interfaces for control and infield processor upgrades.
PRICE	N/A

Manual and References

Datasheet: http://www.focusrobotics.com/docs/focus_ndepth_pci_brief.pdf

A.VII.IV. Bumblebee 2 and Bumblebee XB3

Website: http://www.ptgrey.com/products/stereo.asp

The bumblebee 2 and Bumblebee XB3 are high end stereo vision cameras obtainable with complete hardware and software packages.

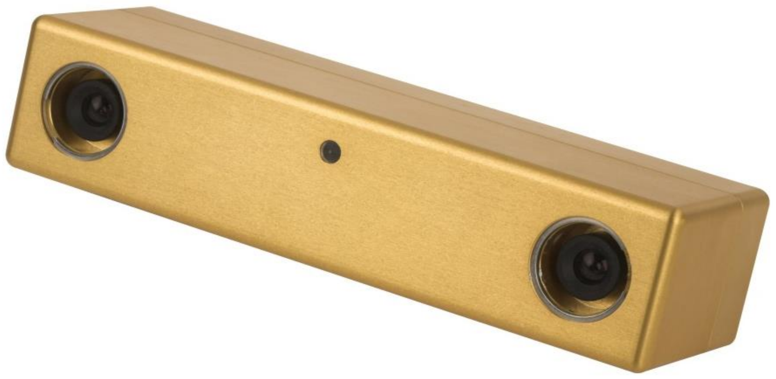

Figure A.XI: Bumblebee 2 Stereo Vision Camera

Table A.IV: Specifications and Features for Bumblebee 2 and Bumblebee XB3

SPECIFICATIONS AND FEATURES

	Bumblebee 2	Bumblebee XB3
FRAME RATE	48 fps , 20 fps	15 fps
RESOLUTION	640x480, 1024x786	1280x960
IMAGE FORMATS	Monochrome and color	Monochrome and color
CALIBRATION	Pre-calibrated to within .1 pixel RMS error	Pre-calibrated to within .1 pixel RMS error
A/D CONVERTER	12-bit ADC	12-bit ADC
CAMERA	Sony® 1/3" progressive scan CCD	Three Sony ICX445 1/3" progressive scan CCD's
BASELINE	12cm or 24 cm	12cm or 24 cm
INTERFACE	6-pin IEEE-1394a	2x9 IEEE-I394 interface and for GPIO pins
DRIVERS	C/C++ API and device drivers.	C/C++ API and device drivers.
SOFTWARE	FlyCapture SDK and Triclops SDK	FlyCapture SDK and Triclops SDK
POWER CONSUMPTION	2.5W at 12V	4 W at 12 V
PRICE	$1,895.00 (640x480), $2,395(1024x786)	N/A

Manual and References

Getting Started Manual for Bumblebee 2:
http://www.ptgrey.com/support/downloads/documents/Bumblebee2%20Getting%20Started%20Manual.pdf
Getting Started Manual for Bumblebee XB3:
http://www.ptgrey.com/support/downloads/documents/Bumblebee%20XB3%20Getting%20Started%20Manual.pdf
Bumblebee 2 Datasheet:
http://www.ptgrey.com/products/bbxb3/bumblebee2_xb3_datasheet.pdf
Triclops SDK Datasheet: http://www.ptgrey.com/products/triclopsSDK/triclops.pdf

A.VII.V. Scorpion 3D Stinger

Website: http://scorpion3dstinger.com/

The Scorpion 3D Stinger is a Vision system designed for industrial robotics applications.

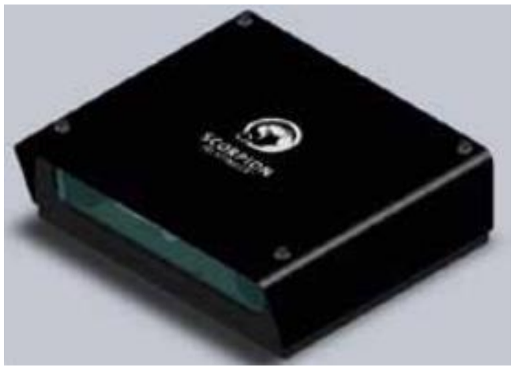
Figure A.XII: Scorpion 3D Stinger Camera

Table A.V: Specifications and Features of Scorpion 3D Stinger Camera

SPECIFICATIONS AND FEATURES	
FRAME RATE	90 fps
RESOLUTION	640x480 (VGA)
IMAGE FORMATS	Monochrome
CAMERA	2 Sony XCG-V6oE cameras
BASELINE	
INTERFACE	1000BASE-T (GigE Vision Compatible), rs-232, or tcp/ip for communication with robots
DRIVERS	N/A (handled through Scorpion Software
SOFTWARE	Scorpion Vision Software
POWER SUPPLY	24V input, 5 and 12V output
PRICE	N/A

Manual and References

Scorpion Stinger Camera Datasheet: http://www.tordivel.no/scorpion/pdf/scorpion%208/PD-2011-0002%20Scorpion%203D%20Stinger%20Camera.pdf

Scorpion Stinger for Robot Vision: http://www.tordivel.no/scorpion/pdf/scorpion%209/PD-2011-0015%20Scorpion%203D%20Stinger%20for%20Robot%20Vision.pdf

A.VII.VI. Enseno N10

The Enseno N10 is a compact Stereo camera with USB interface and a 3D image sensor.

Figure A.XIII: Enseno N10 Stereo Camera

Table A.VI: Specification and Features for Enseno N10 Stereo camera

SPECIFICATIONS AND FEATURES	
FRAME RATE	30 fps
RESOLUTION	752x480 (WVGA)
IMAGE FORMAT	N/A
WORKING RANGE	280-1400 mm
INTERFACE	USB 2.0, M8 GPIO connector
SOFTWARE	Enseno Software API (C++ based)
POWER CONSUMPTION	2.5 W (5V, 500mA)
PRICE	Price on Request

A.VIII. Other IMU Options

This appendix provides an overview for a variety of currently existing Inertial Measurement Units.

A.VIII.I. FreeIMU

FreeIMU is an open source IMU that is primarily intended for the hobbyist market, and is made to be easily interfaced to a small microcontroller. It has limited onboard processing capabilities. In addition to the gyro and accelerometer, it has a magnetometer and a barometer.

Purchase: http://www.varesano.net/projects/hardware/FreeIMU

Datasheet: http://invensense.com/mems/gyro/documents/PS-MPU-6000A-00v3.4.pdf

Figure A.XIV - FreeIMU PCB

Table A.VII: Specification and Features for FreeIMU

SPECIFICATIONS AND FEATURES	
GYRO TYPE	MEMS
ACCELEROMETER TYPE	MEMS
MAX ANGULAR RATE	2000 deg/s
MAX ACCELERATION	16 g
GYRO DRIFT	Not supplied
ACCELEROMETER NOISE	Not supplied
DATA RATE	1000 Hz
INTERFACE	I2C, SPI
RESOLUTION	12 bits
POWER CONSUMPTION	3.9 mA @ 3.3V
PRICE	~$66

A.VIII.II. x-IMU

The x-IMU has more extensive onboard processing using a dsPIC processor. This allows the unit to communicate and log orientation and estimated position data at rates of up to 512 Hz.

Purchase/info: http://www.x-io.co.uk/products/x-imu/#!prettyPhoto

User Manual: http://www.x-io.co.uk/downloads/x-IMU-User-Manual-v5.1.pdf

Example application: https://www.youtube.com/watch?v=6ijArKE8vKU

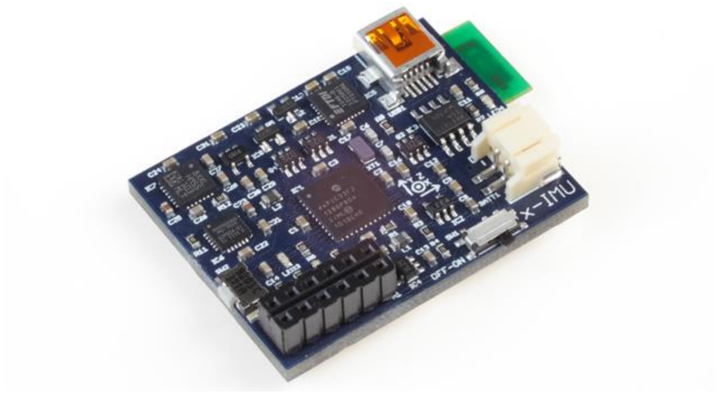

Figure A.XV – x-IMU PCB

Table A.VIII: Specification and Features for x-IMU

SPECIFICATIONS AND FEATURES	
GYRO TYPE	MEMS
ACCELEROMETER TYPE	MEMS
MAX ANGULAR RATE	2000 deg/s
MAX ACCELERATION	8 g
GYRO NOISE	0.01 dps/√Hz
ACCELEROMETER NOISE	Not supplied
DATA RATE	512 Hz
INTERFACE	I2C, SPI
RESOLUTION	16 bits for gyro, 12 bits for accelerometer
POWER CONSUMPTION	50-150 mA @ 3.6-6.3V, depending on settings
PRICE	~$336

A.VIII.III KVH 1750 IMU

The KVH 1750 IMU is a military grade IMU with a fiber optic gyroscope and a low noise MEMS accelerometer. Although this unit is significantly larger than the other units, it offers significantly higher levels of precision, with an angular drift due to gyro bias of less than 0.05 deg/hr.

Info and Datasheet: http://www.kvh.com/Military-and-Government/Gyros-and-Inertial-Systems-and-Compasses/Gyros-and-IMUs-and-INS/IMUs/1750-IMU.aspx

Figure A.XVI – KVH 1750 IMU

Table A.IX: Specification and Features for KVH 1750 IMU

SPECIFICATIONS AND FEATURES	
GYRO TYPE	Fiber Optic
ACCELEROMETER TYPE	MEMS
MAX ANGULAR RATE	490 deg/s
MAX ACCELERATION	10 g
GYRO DRIFT	0.01 dps/√Hz
ACCELEROMETER NOISE	<0.12 mg/√Hz random walk (0.23 ft/sec /√h)
DATA RATE	1000 Hz
INTERFACE	RS-422
RESOLUTION	16 bits for gyro, 12 bits for accelerometer
POWER CONSUMPTION	5-8W, 9-36 V
PRICE	Not supplied

A.IX. Proposed PCB Design

During the early stages of the project the group planned to put the power management system, the FTDI USB to serial bridge for the XBee wireless transceiver, a graphic liquid crystal display controller and the IMU interface on a custom made printed circuit board. Building a custom board would allow these systems to be designed to our specifications so that they would precisely meet our needs. Additionally, combining most of the smaller systems on a single board would have saved a significant amount of space in the final build up. It would have been more robust, as there would have been less cabling that would have been required to connect these subsystems.

The PCB consisted of three major sections. The first of these was the power supply, which stepped the battery voltage down for both the PCB and other off-board systems. A small 8-bit microcontroller was also placed on the board to provide communications with the IMU, to control a graphic LCD screen and to provide battery measurement capabilities. Finally, a FTDI USB to serial bridge was placed on the board to provide the main OMAP board with a simple method of communicating with the XBee. A system block diagram including the custom PCB is shown below.

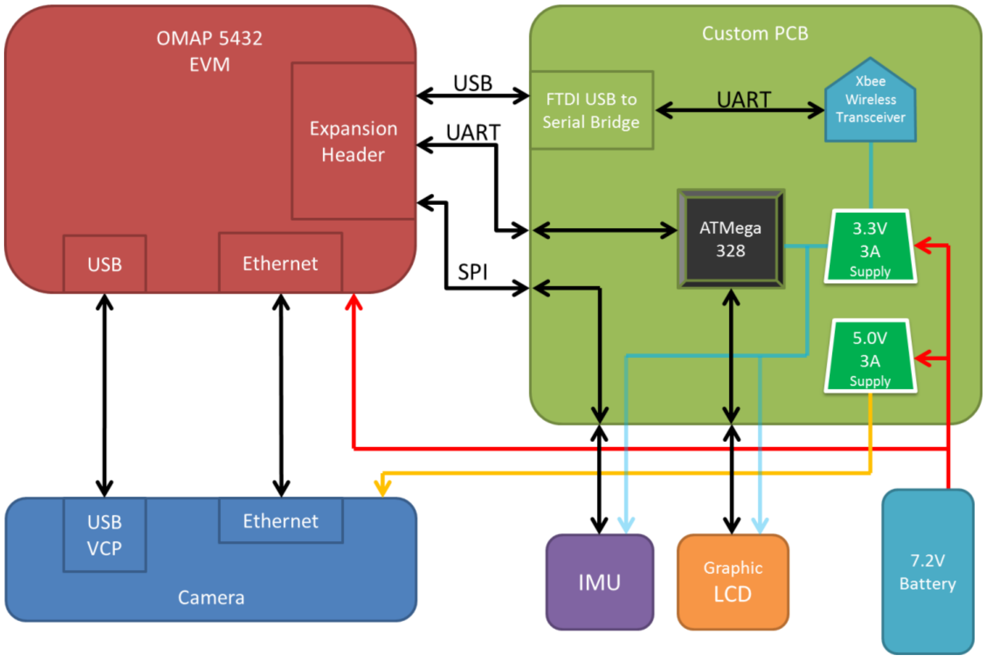

Figure A.XVII - Proposed System Block Diagram Including Custom PCB

A.IX.I. Power Management

Two switching mode power supplies from Alpha Omega Semiconductor are used to provide 5V and 3.3V supplies. The 3.3V supply is used to power the IMU, the ATMega and the graphic LCD. The 5V supply is used to power the Capella Camera. The USB to serial bridge is powered from the USB 5V line. The expected worst case peak power requirements were approximately 1.5 A on the 5V rail and 2 A on the 3.3V rail. To simplify design and layout, the same adjustable switching buck supply was used for both of the supplies. The part, the AOZ1021 from Alpha Omega semiconductors, is capable of sourcing up to 3 A of continuous current, allowing the addition of additional loads of both rails.

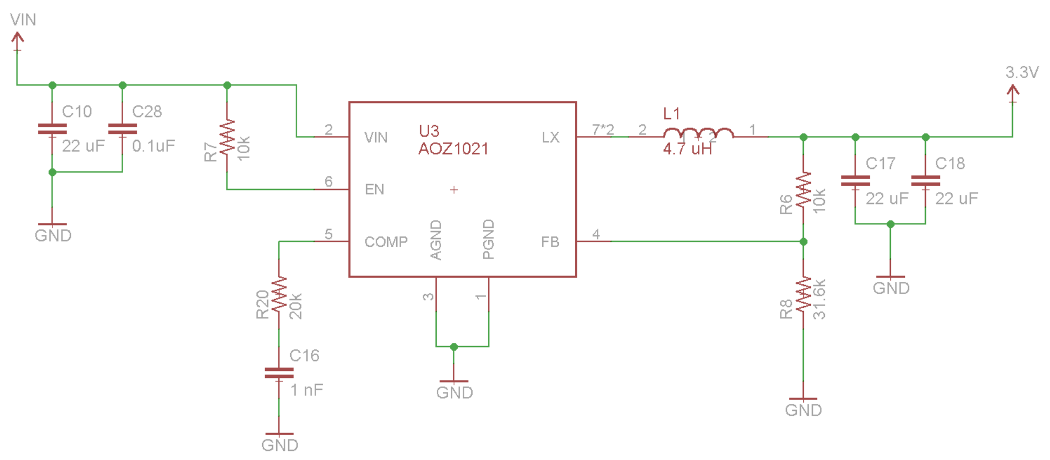

Figure A.XVIII - Schematic for 3.3 V regulator

A.IX.II. Microcontroller

The microcontroller acted as a controller for the graphic LCD, as a battery measurement tool, and as a backup interface for the IMU. The microcontroller chosen was an Atmel ATmega328 clocked at 16 MHz. The ATmega328 is an 8-bit microcontroller with 32 KB of flash memory. This microcontroller was chosen for several reasons. The primary reason was that team members were very familiar with this specific family of microcontrollers, which would speed development. Additionally, it is low-cost, easy to implement, and has several peripherals that applied to this application. The presence of a hardware SPI unit allowed the ATmega to serve as a backup option for connecting the IMU. The UART provided the microcontroller with simple connectivity with the OMAP. Finally, the built in ADC would be used to monitor the battery voltage to prevent over-discharging it.

A.IX.III. XBee Transceiver

The board had a single FTDI USB to serial bridge to connect the XBee transceiver to the OMAP. This device appears as a virtual serial port on the host operating system and presents a 3.3 V serial interface on the other side, compatible with the XBee. In addition to the FTDI receiver, the board had headers so the XBee could be directly connected to the board.

A.IX.IV. Connectivity

The board would be connected to the OMAP via the expansion header on the EVM which has SPI, a USB port, a UART, and I2C which is not used. The available USB port is connected to a USB to serial bridge from FTDI. The serial connection is used to interface with the XBee wireless transceiver, allowing for wireless communications with a base computer.

The UART is connected to the ATMega. The SPI interface is routed through the board and is connected to the IMU. There are jumpers on the board to allow the IMU to be instead connected to the hardware SPI interface on the ATMega if it is later decided to use the ATMega as an interface between the OMAP and the IMU.

A.IX.V. Layout

There were no specific size or shape constraints for the PCB, however to keep fabrication costs to a minimum the board size was minimized. For the same cost reasons, the board was only two layers, which did limit the achievable component density. A first version of the board layout is shown below. The board was 2.25" x 3.0".

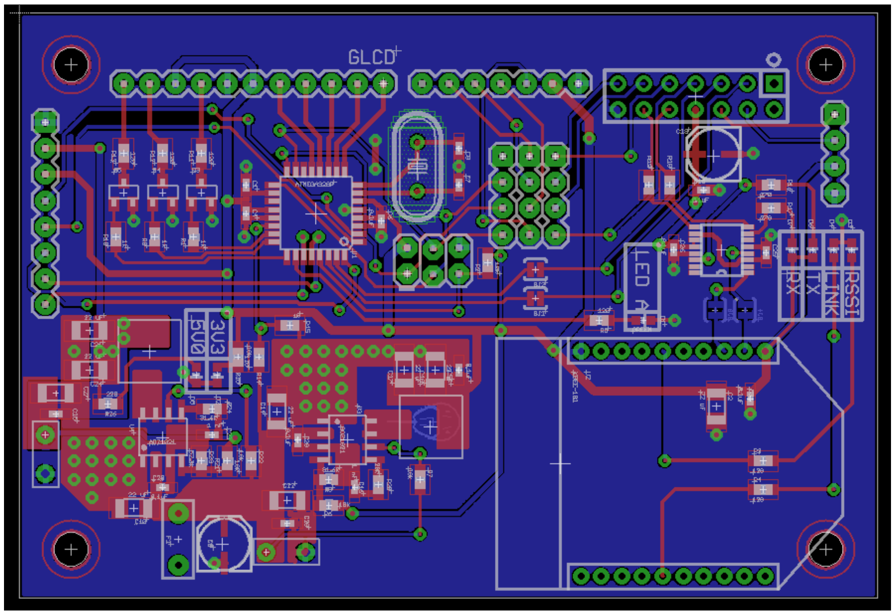

Figure A.XIX - A preliminary layout for the proposed PCB

A.IX.VI. Decision not to use Custom PCB

After serious consideration, the group decided not to continue work on the PCB. It was decided that the same objectives could be achieved through the use of off the shelf components for approximately the same budget and for considerably less effort and in less time. This would come at the cost of working around the restrictions of the off the shelf parts, specifically the Arduino, which proved to have some connectivity problems with the OMAP board. A comparison of the costs for each option is shown below.

Off the Shelf Parts	
Item	**Cost**
Xbee Breakout	$ 24.95
2 x Voltage Regulator	$ 29.90
Total	**$ 84.80**

Custom PCB	
Item	**Cost**
PCB	$ 35.00
Estimated BOM	$ 35.00
Total:	**$ 70.00**

The off the shelf components, their selection, and their implementation are discussed in detail in the System Implementation Section.